Computational Modeling of the Mammalian Cochlea and Cochlea-Inspired Acoustic Devices

by

Aritra Sasmal

A dissertation submitted in partial fulfillment
of the requirements for the degree of
Doctor of Philosophy
(Mechanical Engineering)
in The University of Michigan
2020

Doctoral Committee:

Professor Karl Grosh, Chair
Professor Victoria Booth
Professor Krishna Garikipati
Associate Professor Eric Johnsen
Assistant Professor Bogdan Popa

It's always seemed like a big mystery how nature, seemingly so effortlessly, manages to produce so much that seems to us so complex. Well, I think we found its secret. It's just sampling what's out there in the computational universe.

STEPHEN WOLFRAM

A New Kind of Science

Aritra Sasmal

asasmal@umich.edu

ORCID iD: 0000-0002-5231-2546

ACKNOWLEDGEMENTS

I would like to express my deepest appreciation to Prof. Karl Grosh for his guidance and expertise throughout the process of writing this thesis. This journey would have been considerably more arduous were it not for his constant support and patience. I would also like to thank Prof. Tianying Ren and Prof. Nigel Cooper for providing me with experimental data when I needed it. I would like to acknowledge my committee members, Prof. Victoria Booth, Prof. Krishna Garikipati, Prof. Eric Johnsen, and Prof. Bogdan Popa for providing valuable advice and feedback.

I wish to convey my thanks to all my colleagues and collaborators, especially Alison Hake, Nathan Geib, Dr. Amir Nankali and Dr. Chuming Zhao. Further, I would like to thank Callan Leutkemeyer, Audrey Sedal, Dr. Ashley Bielinski, Dr. James Gorman, Dr. Michael Quann and Dr. Chen Li for their friendship and support.

I would like to extend my sincere thanks to the developers of the various software I have used, and the department's information technology (ME-IT) staff for their support with managing my computing resources over the years.

Finally, I would like to express my sincere gratitude to my fiancée Marie, and my family without whose support none of this would have been possible.

TABLE OF CONTENTS

LIST OF FIGURES

Figure

LIST OF TABLES

Table

LIST OF APPENDICES

Appendix

ABSTRACT

The cochlea is the primary organ in the inner ear associated with hearing, and is responsible for transducing pressure waves in air into neural potentials that can be processed by the central nervous system. The electro-mechanical properties of the cochlea are graded along the cochlear coil to act as a spectrum analyzer with low frequency sounds eliciting a larger vibrational motion at the apex of the coil and higher frequencies at the base. Further, the cochlea is not only a passive sensor, but also amplifies low amplitude sound and compresses high amplitude sound through a non-linear voltage regulated expansion and contraction of the motor protein *prestin* in the lateral membrane of the outer hair cells (OHC). These mechanisms provide mammals with exceptional hearing abilities over a large dynamic range of acoustic intensity. However, this system is often partially or completely damaged, either due to genetic alterations leading to anatomical abnormalities, or due to exposure to acoustic or mechanical trauma. The overarching goal of the first part of this thesis is to develop a detailed fluid-structural-electrical model of the cochlea that describes the *in vivo* response of the cochlea to external stimuli as well as noise present in the system, to understand the mechanism of cochlear transduction and its associated pathologies. This will augment experimental studies by circumventing technological limitations of direct measurement in living cochleae through computer modeling, and assist in formulating new hypotheses that can be tested experimentally. Through our computational framework, we have developed estimates for the system noise incurred during mechanotransduction and show that taller stereocilia are more efficient at detecting vibrations in spite of experiencing more viscous noise. We have shown that

the long-standing challenge of reconciling experimental observations in the base and the apex of the cochlea can be resolved by incorporating the correct cochlear geometry as well as consistently including the effects of the boundary layer in the lymphatic fluids. Further, we have explored the effect of longitudinal spread of current in the lymphatic fluids and analyzed their relevance for the generation and propagation of electrically evoked otoacoustic emissions.

The second part of the thesis develops the theoretical foundations of a new class of non-reciprocal active linear acoustic media that allows vibrations to propagate primarily in one direction. The underlying control architecture is inspired from the phalangeal processes in the inner ear that have been hypothesized to support unidirectional wave propagation from the base to the apex of the cochlear spiral. These acoustic media can have widespread applications in noise and vibration control, as well as signal filtering and duplexing in the communications industry. We show that a cascaded series of non-collocated sensor-actuator pairs can break both spatial and temporal symmetries resulting in a dispersion relation that admits nonreciprocal wave transmission, and develop a generalized theory to derive the system characteristics of this class of active media. Further, we discuss a specific realization of this system using an air-borne acoustic medium and electrodynamic speaker-microphone pairs, and show that it achieves acoustic isolation of over 20 dB across a broad range of frequencies.

CHAPTER I

Introduction

Hearing is one of the fundamental senses through which humans and other animals interact with the physical environment. We rely on sounds for communication, to understand our surroundings, and evade danger. In fact, the acoustic environment is one of the most important evolutionary forces that have shaped the diversity of animals throughout the world [73]. The hearing organ can be found on virtually any part of the body, and the location and anatomical features of the organ reflects the ancestral history of the species [59]. For example, Fig. 1.1 shows the possible locations of the tympanal membrane within the phylogenic group *Insecta*. Within mammals, the hearing organ is localized to the cranium and consists of the outer ear, the middle ear and the inner ear. The cochlea is the anatomical organ in the inner ear that acts as an interface between the physical vibration of the acoustic medium and the psychological perception of sound, by transducing sound into neural signal that the brain can interpret. In this chapter, we will discuss the structural organization of the hearing organ, with a focus on the mammalian cochlea in particular.

1.1 The Mammalian Auditory System

The schematic of the structure of the mammalian auditory system is shown in Fig 1.2(a). Sound enters the outer ear through the external auditory canal and

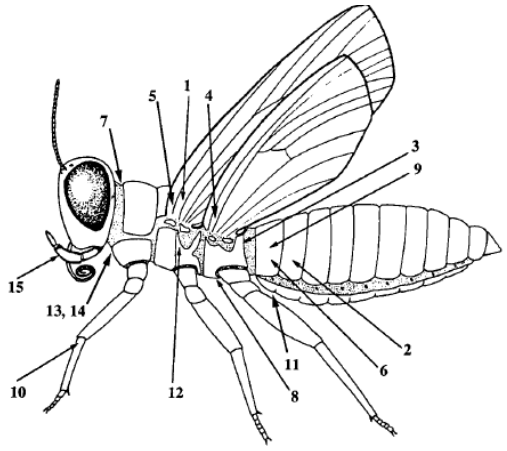

Figure 1.1: The hearing organ in the phylogenic group *Insecta* from [59]. The numbers show the different locations where the tympanum can be found within the group.

vibrates the tympanic membrane. The three bones of the middle ear, the malleus, the incus, and the stapes transfers the vibration from the tympanic membrane to the stapes footplate, and into the cochlea through the oval window. The outer and middle ear serves to reduce the impedence mismatch between the air in the outer ear, and the fluids filled cavity of the cochlea, creating a broad spectral as well as dynamic range over which sound can be effectively transmitted into the cochlea [67]. The inner ear is the hearing and balance center of the peripheral nervous system. It is comprised of the snail shaped hearing organ–the cochlea, as well as the semicircular canals and the otoliths which form the vesticular organ. The inner ear is innervated by the vestibulo-cochlear nerve (cranial nerve VIII) which sends the afferent information from the cochlear and the vestibular organs to their corresponding nuclei in the auditory mid brain, and sends efferent information from the midbrain back to the cochlea . The cochlea is coiled around its central axis, called the modiolus, with the base of the cochlea attached to the oval window (see Fig. 1.2(b)). The number of turns in the cochlea varies among species and is correlated the frequency range over which the animal can hear [43]. The human cochlea is 35 mm long and coils 2.5 times around the modiolus, whereas the guinea pig cochlea is 18.5 mm long and coils four times around the modiolus. The coiling of the cochlea imparts it with a compact geometry to fit

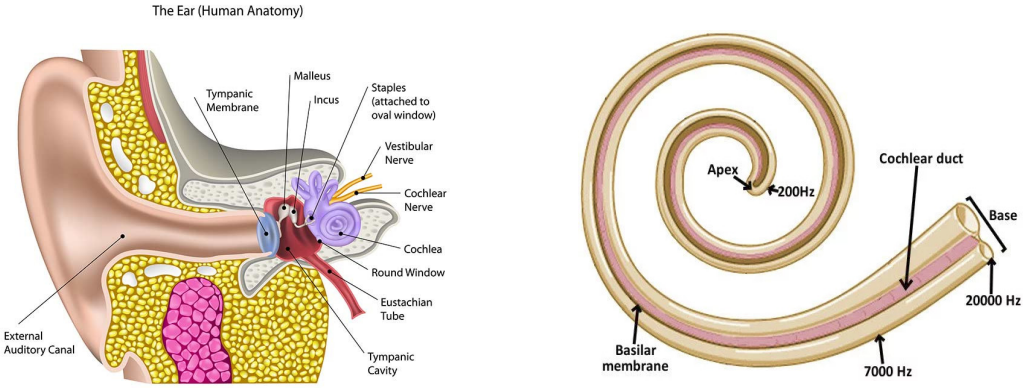

a b

Figure 1.2: The Anatomy of the ear. (a) The organization of the external, middle and inner ear in human, adapted from www.hopkinsmedicine.org. (b) The cochlear spiral showing the cochlear ducts and the tonotopic organization in the human cochlea, adapted from www.scienceabc.com.

into the cranium, but this arrangement has also been postulated to have implications for low frequency hearing [86]. The oval window is connected to the stapes foot plate, which in turn is connected to the middle ear ossicles. The cochlea is tonotopically graded, such that high frequency sounds elicit larger vibration of its structures at the base of the cochlea, and low frequency sounds elicit larger vibrations at the apex, as shown in Fig. 1.2(b). This tonotopic organization in the cochlea is preserved in the auditory nerves, the auditory midbrain and all the way up to the auditory cortex in the brain [153]. This allows the auditory system to spectrally decompose the sound, and then re-construct the auditory scene by extracting only the pertinent information and rejecting the noise.

The mammalian cochlea is transversely divided into three fluid ducts– the scala vestibuli (SV), scala tympani (ST), and the scala media (SM), as shown in Fig. 1.3. The SV and the ST are connected to each other at the apex through a junction known as the helicotrema and contain perilymph. The SV is physically isolated from the SM by a thin membrane known as the Reissner's membrane (RM), and the ST is isolated from the SM by the tight junctions at the apical surface of the inner hair cells

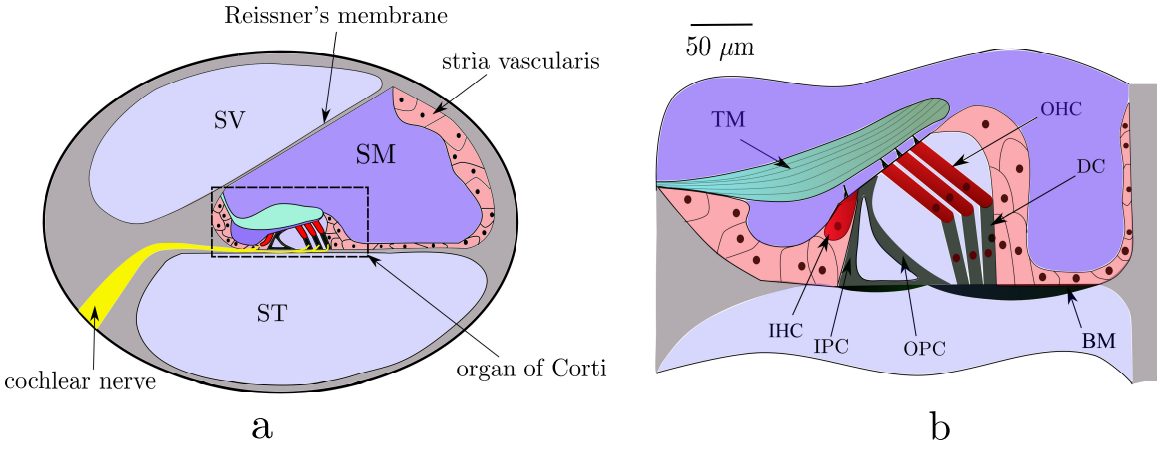

Figure 1.3: Schematic of the cross-section of the mammalian cochlea. (a) The organization of the scalae is shown. The SV and the ST contain perilymph, while the SM contains endolymph. The cochlear nerve innervates the hair cells, with afferent nerves primaruily innervating IHCs and efferent nerves prmiamrily innervating OHCs. The stria vascularis which lines the walls of the SM maintains the potential diffrence between the endolymph and the perilymph, acting as the battery of the cochlea. The OoC sits on the BM. (b) A amgnified view of the OoC showing the IHC, OHCs, TM, IPC, OPC, BM, and DC.

(IHC) and the outer hair cells (OHC). Although both endolymph and perilymph have the same density as water, the ionic concentrations of potassium, sodium, chlorine and calcium in the two fluids are different. The endolymph is at a higher electrical potential (80-90 mV with respect to the perilymph) owing to the higher concentration of potassium in endolymph. This potassium concentration of the endolymph is maintained by cells in the lateral wall of the SM called stria vascularis through a collection of active ion pumps [43]. The hair cells, along with other suporting cells and a gelatinous structure, known as the tectorial membrane (TM), form the organ of Corti (OoC). A magnified view of the OoC is shown in Fig. 1.3(b). The OoC sits on the basilar membrane (BM), which is an orthotropic membrane that is stiffer in the radial direction than the longitudinal direction. The width of the BM increases from base to apex, and the stiffness of the BM decreases from base to apex. This leads to a decrease in the local resonant frequency of the BM, also known as the characteristic frequency (CF), along the spiral axis of the cochlea. The tonotopic

organization of the cochlea is dictated to a great extent by the stiffness gradient of the BM. Indeed, seminal work by Von Békésy on the anatomy and mechanics of the cochlea in human cadavers had attributed the tonotopicity to the gradient in the CF of the BM [154]. However, this is only partially true for a healthy cochlea *in vivo*, and the true tonotopic map depends on other active mechanisms in the cochlea.

The hair cells in the cochlea are classified into two types-the OHCs and the IHCs. The OHCs form two lines along the lateral edge of the OoC, while the IHCs form a single line along the medial edge of the OoC. The OHCs are thought to be primarily responsible for amplifiers in the cochlea, whereas the IHCs are primarily acoustic sensors. In healthy human cochleae, there are around 12000 OHCs and 3500 IHCs. Hair cells have specialized cilia on their apical surface, called sterocilia, that are bathed in endolymph between the TM and the RL, known as the sub-tectorial space (STS). The sterocilia of the IHCs are freely floating whereas the tallest sterocilia of the OHCs are embedded in the lower surface of the TM. The inner and outer hair cells maintain an intracellular electric potential of -50 mV, creating a potential difference of approximately 150 mV across the apical surface of the hair cell [43]. The transverse motion of the cochlear partition leads to the radial shear of the TM. The sterocilia of the OHC are directly coupled to the TM as shown in Fig. 1.4(a), whereas the stereocilia of the IHC are freely floating and are coupled to the radial shear of the TM through the fluid coupling. The cilia are interconnected through tip links, which contain mechanotransduction (MET) channels at the location of its insertion into the top of the stereocilia as shown by dashed circles in Fig. 1.4(a). The deflection of the stereocilia in the excitatory direction leads to the opening of these MET channels an influx of potassium and calcium into the hair cell, depolarizing the hair cell. The depolarization of the hair cell subsequently leads to vescicular release at the synapse triggering an action potential at the afferent nerve. These action potentials subsequently propagate along the auditory neurons to the auditory mid-

brain and finally to the brain for further processing. In this thesis, we are primarily interested in the transduction of sound from physical vibration into neural signals, and will hence restrict ourselves to the cascade of information up till the excitation of the hair cells in the cochlea.

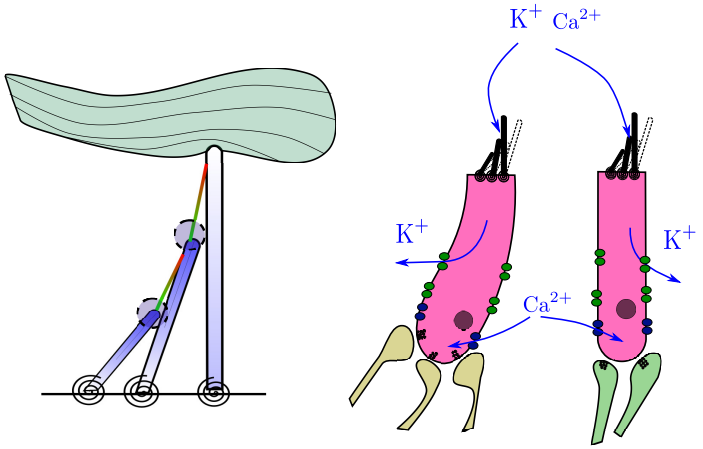

Figure 1.4: The mechanism for the excitation of the hair cells. (a) shows the TM with the stereocilia of an outer hair cell embedded in it. When the TM moves in the excitatory direction, the tension in the tip links increase, leading to ions flowing into the hair cells through the MET channels. The stereocilia of the inner hair cells are not embedded in the TM and are excited primarily by the endolymphatic flow in the space between the TM and the RL. (b) shows the flow of potassium and calcium ions into the hair cells and their consequent exocytosis during depolarization. The influx of calcium leads to release of neurotransmitter at the ribbon synapse.

1.2 Motivation and Objectives

1.2.1 Computational Modeling of the Mammalian Cochlea

Over the last century, research into the peripheral and central auditory system has uncovered the details of several of the processes underlying hearing in mammals and other organisms. These discoveries were usually preceded by the invention of new experimental techniques. For example, the development of the patch clamp technique by Neher and Sakmann provided researchers with the tools to probe the electrical response of the hair cells and the mechanotransduction channels in the stereocilia. Simi-

larly, the development of tools for genetic manipulation led to the discovery of *prestin*, a molecule that is believed to the motor protein in the cochlear outer hair cells and is postulated to play a major role in amplification of sound within the cochlea [162]. These experiments have provided excellent insight into how the different properties of the cochlea operate. However, the transduction of sound is not merely based on the working of the individual components of the cochlea, but a concerted system–level response of all the components within the organ. For example, otoacoustic emissions, sounds generated by the cochlea, arise within the cochlea and depend on the collective response of thousands of hair cells and other structures within the cochlea. Consequently, the study and understanding of the system–level response of the cochlea is of paramount interest to developing a theory of the operation of the cochlea operates. This will aid in the development of cochlear prosthesis as well as non–invasive diagnostic protocols for detection of cochlear pathologies. To this end, mathematical models of the cochlea have proven to be an indispensible tool for probing the system-response to stimuli. The first mathematical framework for understanding the cochlea, developed by Helmholtz [54], assumed the cochlea to be composed of individual Helmholtz resonators tuned to different frequencies that were tonotopically arranged along the cochlear spiral. With the discovery of the traveling wave on the cochlear partition, this model was refined by Von Békésy and others [154, 3, 143] to include the hydrodynamic interactions between the cochlear fluids and the cochlear partition. Later, experimental observations indicated that the cochlear response is strongly nonlinear and the cochlear tuning is sharper that can be explained using linear models alone [119, 131, 103]. Further, the discovery of otoacoustic emission by Kemp [66] and its correlation with cochlear health [125] opened up new avenues of research into the connection between cochlear nonlinearity and cochlear function. One dimensional transmission line models that included nonlinearity and cochlear activity [100, 134] have been very successful in explaining the cochlear tuning as well as otoa-

coustic emissions. However, these models perform poorly close to the 'peak' region of the traveling wave and are phenomenological in nature. Although techniques such as the WKB mthod can be leveraged to resolve the response of the cochlear partition close to the peak, the lack of correlation of the model parameters with anatomical features within the cochlea severely restricts the interpretation of the model results in terms of the *in vivo* respnse of the cochlea. This has necessitated the development of detailed cochlear models that include the cochlear anatomy as well as more detailed modeling of the electrochemical processes and the structural mechanics within the cochlea [97, 114, 130]. Although these models are computationally more expensive than the one dimensional models, the correlation between the cochlear physiology and model parameters provide more accuracy as well as the ability to perform virtual experiments to test hypotheses *in silico*. The overarching goal of this thesis is to develop a detailed computational model of the mammalian cochlea that can reproduce the *in vivo* experimental response of the cochlea and provide tools for the system level response of the peripheral auditory system to guide and motivate future discoveries. In particular, we seek to answer the following questions in this thesis

- The stereocilia in the mammalian cochlea are embedded in an extremely narrow fluid–filled space between the tectorial membrane and reticular lamina. Due to the spatial scales, the fluid flow in this space is primarily viscous, and introduces thermal noise in the mechano–transduction cascade. Further, the gating channels in the stereocilia are stochastic in nature, and generates noise in the system. What is the intrinsic viscous and gating noise present in the mechanotransduction process and how can we quantify their relative contributions *in vivo*?

- It has been long known that the basal end of the cochlea behaves differently from the apical end of the cochlea [136]. For example, the basal tuning curves obtained from the neurons exhibit sharp tuning and a 'tip-tail' transition whereas

the apical tuning curves are more 'V' shaped [31]. Further, experiments using optical coherence tomography has shown that the different parts of the organ of Corti vibrate differently in response of stimulation [115]. Earlier models have been unable to reproduce these results. What are the necessary physics that cochlear models require to reconcile their predictions with experimental observations?

- Electrically evoked otoacoustic emissions (EEOAE) have been used for some time to detect and probe the mechano-electrical activity of the cochlea [104]. More specifically, intracochlear electrical stimulations are predicted to produce otoacoustic emissions that have twice the delay as the forward delay during acoustic stimulation. However, experimental intracochlear and EEOAE measurements in the mouse [118] have shown that the electrical delay is closer to the forward acoustic delay, contradicting the theoretical predictions. Is it possible to explain the discrepancy between the experimental predictions from [118] with theoretical models?

1.2.2 Design of Cochlea–inspired Nonreciprocal Metamaterial

The ability to design systems that manifest unidirectional wave propagation could provide for exquisite control over acoustic signals, and would have enormous implications for noise control and filter design. For example, the ability to control the direction of acoustic signal propagation would allow the design of full-duplex communication systems by coupling RF signals with acoustic waves on a MEMS device. Similarly, coupling of unidirectional wave physics to surface acoustic waves or bulk acoustic waves can be used to create novel filters for use in consumer electronic components or biomedical devices. Although acoustic devices that achieve nonreciprocity through modulation of the background medium or through the generation of nonlinearity has been proposed and demonstrated in the literature, these devices are either

bigger than the acoustic wavelength, making it unsuitable for integration on a chip, or generate nonlinearities that create harmonics that corrupt the signal.

In this thesis, we circumvent both of these issues by designing an active nonreciprocal system that is linear, broadband and sub–wavelength. This design is inspired from the cochlear cyto–architecture in mammals, where the canting of the hair cells and the phalangeal processes create a push–pull mechanism that has been hypothesized to play a role in the cochlear amplification process [44, 158]. The objective of the second part of this thesis is to explore the wave dispersion induced by this system and to develop a generalized theory for the stability of this class of active nonreciprocal systems.

1.3 Organization of the Thesis

This thesis has been divided into six chapters. The second chapter introduces the 3D finite element methodology used throughout this thesis, as well as the Matlab–based finite element framework created for the numerical computations. In chapter III, estimates for the inherent noise in the mechanotransduction process are derived. Chapter IV develops an unified model for the mammalian cochlea. Chapter V expands upon the current model to explain some of the observations from EEOAEs. Finally, chapter VI discusses the cochlea–inspired nonreciprocal device. The thesis concludes with a summary of the results and suggestions for future work that can build upon this study.

CHAPTER II

Computational Model of the Cochlea

In this chapter, we will introduce the differential (strong) formulation of the equations used to model the solid-fluid-electrical interactions in the guinea pig cochlea, followed by the weak formulation of the problem for implementation in the finite element framework. Finally, we will discuss the computational code that has been developed for efficiently solving and visualizing the calculations.

To study the multi-scale dynamics of the cochlea, we have modeled the cochlea through a combination of analytical and numerical methods. The cochlea has been modeled as a prismatic box with two fluid filled ducts, connected at the apex, as shown in Fig. 2.1. The x, y, and z coordinates are along the longitudinal, radial and transverse directions respectively, and this convention has been used throughout this chapter. The stapes and the round window membranes are assumed to be coupled to the fluid in the scala vestibuli (SV) and the scala tympani (ST). The basilar membrane (BM) is assumed to centered along the radial direction throughout the cochlea. The organ of Corti is modeled as a composite structure consisting of the hair cells, the pillar cells, hair bundles and the tectorial membrane, as shown in Fig. 2.1(b) and discussed in [114].The fluid in both scalae is assumed to be coupled with the BM and the organ of Corti is assumed to be acoustically transparent. In the next section, we will discuss the equations describing the individual components in more detail.

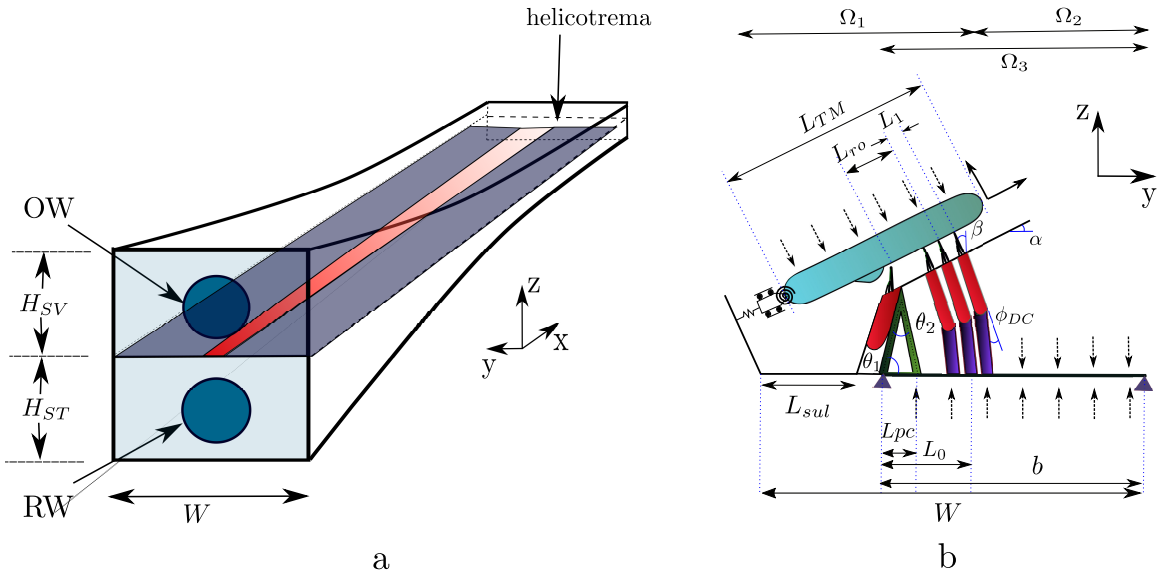

Figure 2.1: Model of the mammalian cochlea. (a) The global model of the cochlea. The cochlea is assumed to have a constant width (W) from base to apex. The height of the scala vestibuli (H_{SV}) and the scala tympani (H_{ST}) decreases from base to apex, and the height profile is specific to each animal. The oval window (OW) and the round window (RW) are coupled to the scala fluid. (b) The schematic of the kinematic description of the organ of Corti. The width of the BM (b) increases tonotopically from base to apex. The length of the TM (L_{TM}), distance between the hair bundles (L_1), distance between the outer and inner pillar cells (L_{pc}), and the angles θ_1, θ_2, ϕ_{DC}, α and β are varied throughout the cochlea according to morphological data from experiments.

2.1 The Differential Formulation

2.1.1 Fluid Domain

The SV and ST are modeled as tapered ducts, separated by the cochlear partition. The RM is assumed to be acoustically transparent, and hence is ignored in the modeling. The fluid in the SV and the ST is modeled by the inviscid compressible Helmholtz equation,

$$\nabla^2 p + \left(\frac{\omega}{c}\right)^2 p = 0 \tag{2.1}$$

where ω is the angular frequency and c is the speed of sound in water. The effect of fluid viscosity is included throguh the modified boundary condition between the fluid

and the structure (BM) is given by [13, 7]

$$-\frac{\partial p}{\partial n} + \frac{1}{\gamma}\nabla_s^2 p = \frac{1}{\alpha}\rho_f \omega^2 u_s, \tag{2.2}$$

where n is the local coordinate normal to the fluid-structure interface, μ is the dynamic viscosity of water, ρ_f is the density of the water, $\gamma^2 = \frac{i\omega\rho_f}{\mu}$, $\alpha = 1 + \frac{i4}{3\rho_f c^2}$. ∇_s^2 is the in-plane 2D Laplacian defined here as $\frac{\partial^2}{\partial x^2} + \frac{\partial^2}{\partial y^2}$. This asymptotic formulation of fluid viscosity leads avoids dense meshing at the fluid-structure interface and shows excellent convergence for low Reynold's number flow (Stokes' flow) [13].

To avoid full 3D computation of the fluid pressure field, we assume a set of orthonormal spatial modes in the y direction that satisfy the radial boundary conditions. The pressure in the ducts is decomposed in the radial (y) direction as

$$p(x, y, z) = \sum_{m}^{M-1} p_m(x, z) \cos\left(\frac{m\pi(y + W/2)}{W}\right), \quad -0.5W \leq y \leq 0.5W \tag{2.3}$$

where W is the width of the duct as shown in Fig. 2.1(a), m is the mode shape number and M is the maximum number of fluid modes. Note that these radial modes satisfy the rigid wall boundary conditions at $y = \pm\frac{W}{2}$. Substituting Eq. 2.3 in Eq. 2.1, and invoking the orthogonality of the fluid modes leads to the reduction of the fluid domain to two dimensions as,

$$\frac{\partial^2 p_m(x, z)}{\partial x^2} + \frac{\partial^2 p_m(x, z)}{\partial z^2} + \left[\left(\frac{\omega}{c}\right)^2 - \left(\frac{m\pi}{W(x)}\right)^2\right] p_m(x, z) = 0, \tag{2.4}$$

where $W(x)$ is the width of the duct at distance x from the stapes.

2.1.2 Structural Domain

The BM is stiffer in the radial (y) direction than in the longitudinal (x) direction, and is hence modeled as an orthotropic plate [87]. The governing equation for the BM motion is

$$\begin{aligned} P_{bm}^{ext}(x,y) =& \frac{2}{b(x)} C_{bm}\dot{u}_{bm}(x,y) + M_{bm}\ddot{u}_{bm}(x,y) - \frac{\partial^2}{\partial x^2}\left(D_{xx}\frac{\partial^2 u_{bm}(x,y)}{\partial x^2} \right. \\ & \left. + D_{xy}\frac{\partial^2 u_{bm}(x,y)}{\partial y^2}\right) - 2\frac{\partial^2}{\partial x \partial y}\left(D_s \frac{\partial^2 u_{bm}(x,y)}{\partial x^{\partial} y}\right) \\ & + \frac{\partial^2}{\partial y^2}\left(D_{yy}\frac{\partial^2 u_{bm}(x,y)}{\partial y^2} - D_{xy}\frac{\partial^2 u_{bm}(x,y)}{\partial x^2}\right), \end{aligned} \tag{2.5}$$

where P_{bm}^{ext} is the net external pressure distribution on the BM from the fluid and the OHCs, and D_{xx},D_{xy},D_s and D_{yy} are orthotropic plate stiffnesses. The BM has been assumed to vibrate with the mode shape corresponding to the first vibrational mode of a plate under pinned-pinned boundary condition in the radial direction given by

$$u_{bm}(x,y) = u_{bm}(x)\sin\left(\frac{\pi(y+0.5b(x))}{b(x)}\right), \quad -0.5b(x) \le y \le 0.5b(x) \tag{2.6}$$

where $b(x)$ is the width of the BM at distance x from the stapes.

The TM is modeled as a longitudinally coupled Euler–Bernoulli beam of cross-sectional area A_{tm}. It has two degree of freedom system with elastic deformations in the radial (y) and transverse direction (z), and is longitudinally coupled through elastic stiffness (G_{xy}) and shear viscosity (η_{xy}). The governing equation of the TM radial motion (u_{tms}) can be written as

$$F_{tm}^{ext} = u_{tms}u_{tms} + C_{tms}\dot{u}_{tms} + M_{tms}\ddot{u}_{tms}\frac{\partial}{\partial x}\left(A_{tm}G_{xy}\frac{\partial u_{tms}}{\partial x} + A_{tm}\eta_{xy}\frac{\partial \dot{u}_{tms}}{\partial x}\right), \tag{2.7}$$

where F_{tm}^{ext} is the total force on the TM in the radial direction by the OHC HBs. The

transverse motion u_{tmb} is assumed to be kinematically constrained with one end attached to the second row of the outer hair cell hair bundle and the other end attached to the osseo-spiral lamina through a torsional spring, as shwon in Fig. 2.1(b). The kinematics and the dynamics of the other cells in the organ of Corti are formulated through a Lagrangian framework, as detailed in [114].

2.1.3 Electrical Domain

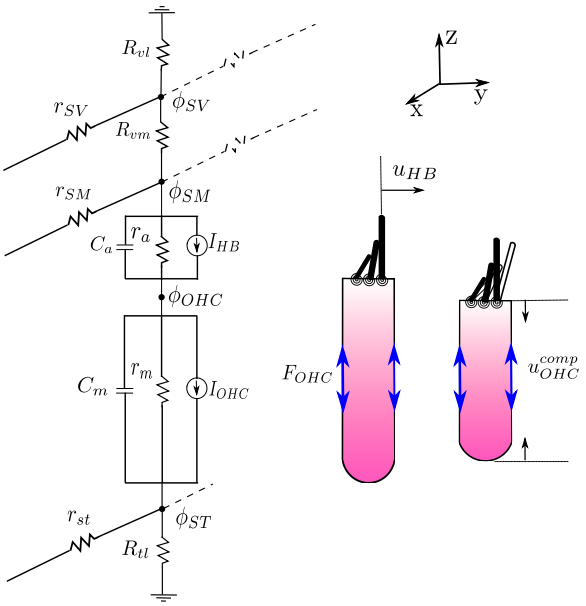

Figure 2.2: Model of the electrical cables and hair cell circuit.

The current flow in the scalae is modeled using one dimensional cable theory [114, 22]. The electrical potentials in the SV, SM, OHC, and ST are given by ϕ_{SV}, ϕ_{SM}, ϕ_{OHC}, and ϕ_{ST} respectively. The schematic of the electrical circuit is shown in

Fig. 2.2. The governing equations are given by

$$\frac{1}{r_{SV}}\frac{\partial^2\phi_{SV}}{\partial x^2} - \left(\frac{1}{R_{vl}} + \frac{1}{R_{vm}}\right)\phi_{SV} + \frac{1}{R_{sm}}\phi_{SM} =, 0 \tag{2.8}$$

$$\frac{1}{R_{sm}}\phi_{SV} + \frac{1}{r_{sm}}\frac{\partial^2\phi_{SM}}{\partial x^2} - \left(\frac{1}{R_{sm}} + 3Y_a\right)\phi_{SM} + 3Y_a\phi_{OHC} - I_{HB} = 0, \tag{2.9}$$

$$3Y_a\phi_{SM} - 3\left(Y_a + Y_m\right)\phi_{OHC} + 3Y_m\phi_{ST} + I_{HB} - I_{OHC} = 0, \tag{2.10}$$

$$3Y_m\phi_{OHC} + \frac{1}{r_{st}}\frac{\partial^2\phi_{ST}}{\partial x^2} - \left(\frac{1}{R_{tl}} + 3Y_m\right)\phi_{ST} + I_{OHC} = 0, \tag{2.11}$$

where Y_a and Y_m are admittances at the apical and basal surface of the OHC, respectively. An extension of the current cable model that includes an extra electrical node in the interstitial space (ISP) close to the base of the OHC will be discussed in Chapter V. This extension leads to better model agreement with experimental results when the cochlea is stimulated using intracochlear electrical stimuli, but has negligible influence on the cochlear response to acoustic stimulation at the stapes. I_{HB} is the current passing through the MET channels in the HBs and is given by

$$I_{HB} = \left(\phi_{SM} - \phi_{OHC}\right)G_{MET}. \tag{2.12}$$

where G_{MET} is the MET conductance and can be written as

$$G_{MET} = \frac{G_0}{1 + e^{-(u_{HB} - u^0_{HB})/\delta_{HB}}}, \tag{2.13}$$

where G_0 is the maximum MET conductance, u_{HB} is the HB deflection, u^0_{HB} is the resting displacement of the HB, and δ_{HB} is the MET channel width. I_{OHC} is the current due to the piezo action of the basolateral membrane of the OHCs, given by

$$I_{OHC} = \sum_{j=1}^{3} \epsilon_3 \dot{u}^{comp}_{OHC,j}, \tag{2.14}$$

where $u_{OHC,j}^{comp}$ is the total inward compression of the j^{th} OHC and Z_m is the basolateral impedence. The force transduced by the j^{th} OHC is given by

$$F_{OHC,j} = K_{OHC} u_{OHC,j}^{comp} + \epsilon\Big(\phi_{OHC} - \phi_{ST}\Big), \tag{2.15}$$

where K_{OHC} is the OHC axial stiffness.

2.2 The Weak Formulation

Eq. 2.1 through Eq. 2.15 can be converted to the weak form [60], and discretized into the finite dimensional weak form. Linear shape functions were used as interpolation functions for second order differential equations (Eqs. 2.1,2.8) and Hermite shape functions were used to interpolate fourth order differential equations (Eq. 2.5). The finite element dynamic stiffness matrix can be written as

$$\begin{bmatrix} K_f & Q_{fs} & 0 \\ Q_{sf} & K_s & Q_{se} \\ 0 & Q_{es} & K_e \end{bmatrix} \begin{pmatrix} p \\ u \\ \phi \end{pmatrix} + \begin{pmatrix} 0 \\ 0 \\ \Omega_{NL} \end{pmatrix} = \begin{pmatrix} f_p \\ f_u \\ f_e \end{pmatrix}, \tag{2.16}$$

where p, u and ϕ correspond to the fluid, structural and electrical degrees of freedom, respectively. K_f, K_s, and K_e are the dynamic stiffness matrices associated with the fluid, structural and electrical domains. Q_{fs} and Q_{sf} are the coupling matrices for the fluid-structure interactions. Q_{se} and Q_{es} are the coupling matrices for the electrical-structure interactions. The f_p, f_s, and f_e represent the forcing due to the natural boundary conditions on the fluid, structural, and electrical nodes, respectively. Ω_{NL} contains the nonlinear forcing associated with the MET current in Eq. 2.8. The coupled set of equations are solved using the numerical suite as described in the next section.

2.3 The Numerical Framework

2.3.1 The Structure of CSound

To solve the coupled set of equations, a finite element solver has been developed in MATLAB (The Mathworks, Natick, MA). The structure of the FEA suite is shown in Fig. 2.3. The entire suite has been organized into four directories– Exe, Elibrary, Parameters, and Main Files. The Exe directory contains the executable 'Csound.m' that contains the FEA assembler and solver, as well as the data input files (inside the subdirectory C_data_files) that prescribe the physics, global properties, connectivity etc. The Elibrary directory contains the files necessary for implementation of different physics associated with the problem. These files are divided into two groups, based on whether they are implemented in the frequnecy domain or the time domain. The files containing frequency domain physics are named as ElemFD****.m, where * is a number from 1 through 0, and the files containing time domain physics are named as ElemTD***.m. During computation of the response of the cochlea to stimuli in the frequency domain, the files containing the frequency domain physics are evaluated at every frequency step, whereas the files containing the time domain physics are evaluated only once to yield the corresponding mass, stiffness and damping matrices saving computation time. Note that the frequency domain elements are only used when the physics cannot be written in terms of the mass, stiffness and damping matrices and includes physics that contain non-integer powers of frequency. The Parameters directory contains the functions that yield the local parameters of different parts of the cochlea and are obtained from experiments. Finally, the Main Files directory contains codes that are used during numerical computations and are not specific to the physics of the problem, for example, Gauss quadrature and interpolation functions.

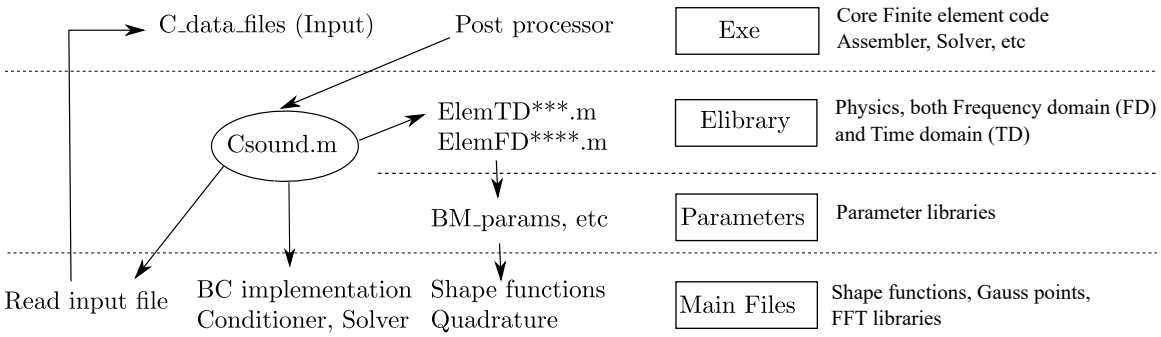

Figure 2.3: Structure of the Csound suite. The four directories– Exe, ELibrary, Parameters, and Main Files are used to organize the files in the suite. The arrows show dependency between the files, such that A→B implies that the A depends on B. The dotted lines have been used to demarcate the locations of the files in the directories. The data input file is included in the C_data_files and specifies the problem description. The primary executable file CSound.m reads the data from the input file and and computes the nodal values using the physics (Elem***TD.m and Elem****FD.m) and associated finite element files. The output is read by the post processor and visualized using the visualization tools

2.3.2 The Different Solvers in CSound

Fig. 2.4 shows the primary structure of the Csound.m file. Upon execution, it links the associated libraries, reads the input data files and outputs useful information for the post processor. There are three types of solvers built into Csound. The frequency domain (FD) solver is used for solving the linearized version of Eq. 2.16, which can be written as

$$\begin{bmatrix} K_f(\omega) & Q_{fs}(\omega) & 0 \\ Q_{sf}(\omega) & K_s(\omega) & Q_{se}(\omega) \\ 0 & \tilde{Q_{es}}(\omega) & \tilde{K_e}(\omega) \end{bmatrix} \begin{pmatrix} p(\omega) \\ u(\omega) \\ \phi(\omega) \end{pmatrix} = \begin{pmatrix} f_p(\omega) \\ f_u(\omega) \\ f_e(\omega) \end{pmatrix}, \tag{2.17}$$

where the tilde matrices are modified versions of Eq. 2.16 to accommodate the linearization of Ω_{NL}. The time domain response to an arbitrary stimulus can be constructed by taking the inverse Fourier transform of the solution of Eq. 2.17. The time

domain (TD) calculations are computed by rewriting Eq. 2.16 as

$$M_{sys}\ddot{Y} + C_{sys}\ddot{Y} + K_{sys}\ddot{Y} = F_{sys}, \tag{2.18}$$

where $Y = [p, u, \phi]^T$, and M_{sys}, C_{sys} and K_{sys} are the corresponding mass, damping and stiffness matrices. This system can be solved used ODE23s in Matlab. However, note that non-integer frequency dependence cannot be included in this formalism because that would require the inclusion of fractional derivatives. Secondly, the problem is stiff and the mass matrix M is singular, which results in expensive computations [91, 69]. To reduce the computational overhead, the fluid nodes are removed using modal reduction, and the longitudinal cables in the scalae are eliminated, similar to the procedure outlined in [91]. Although this leads to fast computations in the time domain, the approximations introduced by this method change the dynamics of the cochlear response to external stimuli (as discussed in Chapter V) which could lead to wrong model predictions.

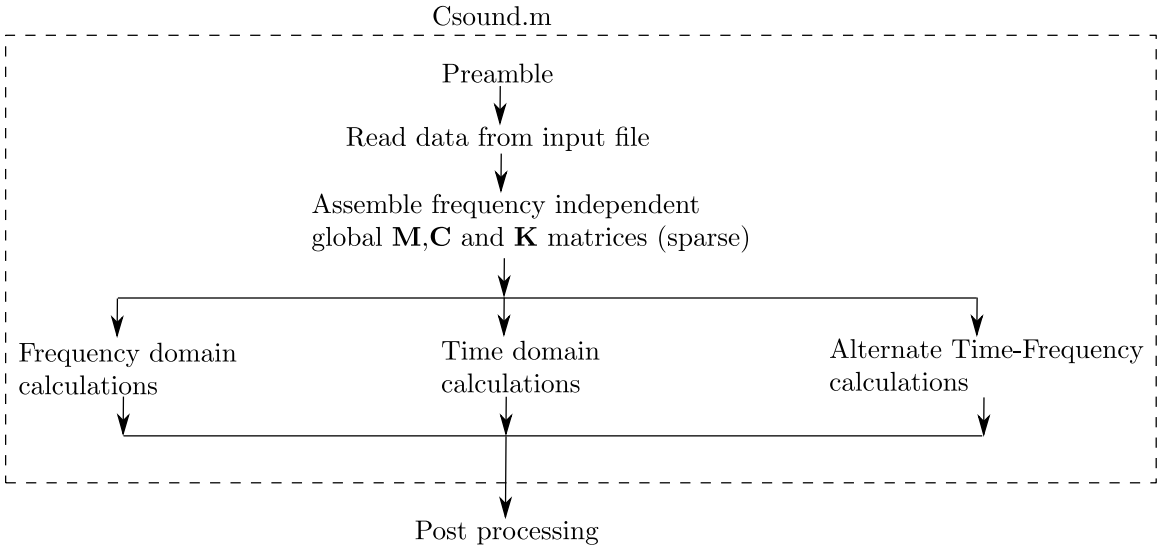

Figure 2.4: Schematic of the workflow in the CSound executable.

To circumvent the problems associated with the TD solver, and to include fractional frequency-dependent physics, the alternate time-frequency (ATF) method is

preferred [89]. This method requires a pre-determined set of harmonics (ω_i) that the solver considers while solving the coupled set of nonlinear equations. In Csound, this is automatically generated by picking the highest N_{harm} harmonics in the Fourier spectrum when the nonlinear term Ω_{NL} is excited using the stimulus. There are further provisions to dynamically update the list of harmonics if other dominant frequencies emerge during iteration. The ATF algorithm is summarized in the following steps.

(i). Solve Eq. 2.16 without Ω_{NL} in the frequnecy domain for frequencies ω_i and calculate the solutions $Y(\omega_i)$.

(ii). Calculate $Y(t) = \sum_{\omega \in \omega_i} Y(\omega) e^{-i\omega t}$.

(iii). Calculate $\Omega_{NL}(t)$ from $Y(t)$.

(iv). Calculate $\Omega_{NL}(\omega_i)$ from $\Omega_{NL}(t)$ through the Fourier transform.

(v). Add the spectral components of $\Omega_{NL}(\omega_i)$ to the corresponding components of $f_e(\omega_i)$. Go to step (i) or stop if the relative error is less than the tolerance.

Note that although the ATF method is fast, convergence is not always guaranteed. Further, it is not possible to calculate the transient response of the cochlea using this method.

CHAPTER III

Signal and Noise in the Inner Hair Cell Stereocilia

3.1 Introduction

The inner hair cells (IHCs) of the mammalian cochlea are responsible for transducing the nanometer-scale motion of IHC stereocilia into afferent neural impulses. Consequently, the mechanical response of the stereocilia to noise forces, either due to viscosity or channel stochasticity, sets the mechanical noise floor of the sensor. The IHC stereociliary hair bundles (HBs) are immersed in an endolymphatic fluid contained in a gap between the reticular lamina (RL) and the basal surface of the tectorial membrane (TM) called the subtectorial space (STS). The thickness of the STS gap ranges from from around 2 µm at the base of the cochlea to 5 µm at the apex while the gaps between free-standing tips of the IHC stereocilia and the TM are much smaller, approximately 5% of those values (see Fig. 3.1). The viscosity of the STS fluid induces thermal noise forces onto the IHC HB as quantified by the fluctuation dissipation theorem [58]. From a noise perspective, positioning the HB in such a narrow gap seems like a poor arrangement because the viscous boundary layer fills the entire channel at acoustic frequencies. However, the viscous STS fluid that induces noise on the HB is also responsible for imparting high sensitivity to the HBs by coupling them to the shear motion of the TM. Superimposed upon the viscous noise is the stochastic noise of the mechanically gated ion channels [95, 9]. In this

paper, we study the competition between both these noise sources and the stimulus forces by developing a mathematical model of fluid-structure interaction and channel gating in the organ of Corti (OoC) of the cochlea.

The importance of modeling cochlear micro-mechanics for determining the sensitivity of the organ to sound stimulation was realized early on by Allen [3] and others. For instance, Mammano and Nobili [85] analyzed the dynamics in a more geometrically accurate representation of the fluid using a integral equation approach. In addition, they used a micromechanical model including a partial model of the electromechanics of the interaction of outer hair cell HB motion to somatic motility, an approach that was extended to include a complete model in Ramamoorthy, et al.[114]. The importance of the including the effects of longitudinal viscoelastic coupling of the TM was highlighted in modeling by Meaud and Grosh [87]. Although these macroscopic cochlear models serve to predict the cochlear responses (e.g., pressure in the cochlear fluid and the displacement of the structures) they do not predict the afferent signal transduction because the excitation of the stereocilia of the IHC is not included. Such predictions require modeling the interaction of the STS fluid, the TM, reticular lamina (RL), the inner sulcus (IS), and the IHC stereocilia. Freeman and Weiss [38] studied the different frequency regimes of excitation of a free standing stereocilia bathed in a viscous fluid, seeking to understand the sensitivity of the HB to the shear motion of a nearby surface. Raftenberg [113] developed an analytic framework for the flow of endolymph in the STS and into the IS, and the different possible modes of excitation of the IHC stereocilia. Steele and Puria [142] developed a composite model of the flow in the STS, IS and over the IHC stereocilia and discussed the importance of such modeling to explain IHC recordings in a mammalian hearing organ. More recently Prodanovic, et al. [111] studied the effect of fluid flow across the HB on viscous dissipation in the OoC using a numerical approach. These studies did not analyze the noise on the HB, rather focusing on the sensitivity to excitation

and losses in the system.

Although the previous cross-sectional models [142, 111] include viscosity but not noise, there is experimental data to bound the level of noise. Denk, et al. [27] measured the motion and estimated the hydrodynamic drag on a hair bundle of a bullfrog sacculus finding the drag coefficient to be of the order of 10^{-7} $\mathrm{N\,m^{-1}\,s}$. A second source of noise arises from the inherent stochasticity of the mechanically gated MET channels attached to the tip links of the HBs. The estimated equivalent drag coefficient from the channel clatter was calculated to be of the order of 10^{-6} $\mathrm{N\,m^{-1}\,s}$ for the bullfrog [95]. Since this is more than the hydrodynamic drag on a free-standing bullfrog HB, the threshold of IHC transduction is thought to be limited by the channel clatter [95, 9]. However, the anatomy of the saccular HC is different (no TM and bundle dimensions) and the MET sensitivity to motion they used is smaller that than currently estimated for mammals. Hence, they likely underestimated the effect of viscouse noise (especially for high frequency hearing). Van Netten, et. al. [152] calculated a lower bound of the channel clatter based on the Cramer-Rao bound and compared their results with experimental estimates from an apical mouse outer hair cell. They did not perform a full coupled analysis of the viscous and channel noise properties on the noise-induced HB motion as we do here.

In the present work, we model the complete STS-IS fluid flow in a gerbil cochlea and derive the sensitivity and noise of the system through analytic techniques. Although channel clatter is the dominant noise for a stereocilia suspended in a larger fluid bath like that in the bullfrog sacculus, the substantially different morphology of the mammalian organ of Corti, where the stereocilia are confined between the RL and the viscoelastic TM, warrants a separate analysis. We compare the contributions of viscous forces and channel clatter to the noise in the HB mechanical displacement and current spectra, and their variation from base to apex. Further, we calculate the TM threshold motion and discuss the tradeoffs between sensitivity and noise with

change in height of the HBs.

3.2 Methods

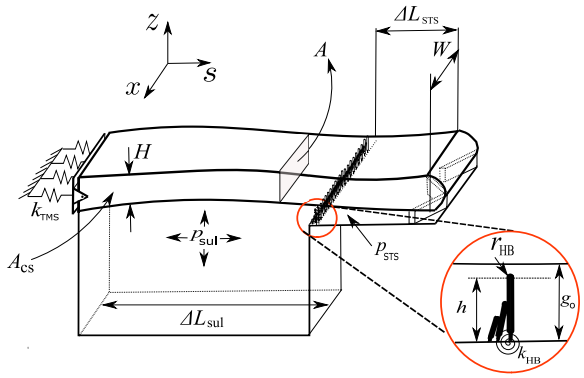

Figure 3.1: A generalized schematic model of the cross-section of the mammalian OoC. The pressure in the STS (p_{STS}) varies in the radial (s) and longitudinal (x) directions while the sulcus pressure (p_{sul}) is assumed to be constant in the cross-section and varies only in the longitudinal (x) direction. The TM is attached to the inner sulcus through an extension spring (k_{TMS}). The IHC HBs (inset) are modeled as stiff rods of height h with a rotational spring, k_{HB}, at the base. The three rows of the OHC HB have been modeled as a single row with net effective impedance of three rows in the model. Geometric quantities are defined in Tab. A.1. This figure is not to scale.

We adopt an approach similar to Steele and Puria [142] and Li [74] to model the subtectorial gap with a shadow coordinate frame attached to the RL to represent the cross-section of the STS, sulcus, and TM as shown in Fig. 3.1. Asymptotic expressions were used for modeling the fluid structure interaction in the STS (Section A in Supporting Material). Thin film lubrication theory was used to calculate the fluid pressure (p_{STS}) and velocity fields in the STS and couple these fields to the structural equations of the TM to yield the overall response of the cross-section. Lubrication theory holds because the combined boundary layers of the RL and TM are thicker than the gap between the TM and the RL in the STS (g_0) at acoustic frequencies [7]. The sulcus is modeled as a constant pressure cavity (p_{sul}), with flow along cochlear spiral (the longitudinal (x) direction) governed by the inviscid Euler equation along

with lossy leakage flow into the STS through the narrow gap between the TM and the IHC HB. The HB is approximated as a rigid rod of height h, pivoting about the cuticular plate resisted by the stiffness associated with the insertion into the plate, the tip link stiffness, and the lateral link stiffness, as shown in the inset in Fig.3.1. The IHC HB rotation results from the fluid pressure and shear forces integrated along the surface of the HB. The three rows of OHC HBs at the SM connection with the STS have been modeled with an effective gap impedance derived by considering the pressure drop due to fluid flow between two OHC ciliary bundles, each 8 µm wide along the x direction, separated by a 2 µm gap (Section A in Supporting Material). The TM is modeled as a viscoelastic beam with thickness H in the cross-section with viscoelastic longitudinal coupling as in [87] and experimentally demonstrated in [45]. We used a constant value for the shear structural damping (loss tangent equal to 0.3) that is the average of the frequency dependent value measured by in mice TM [64]. Variation of the loss tangent did not significantly affect our noise calculations, hence this simplifying assumption does not affect our conclusions.

The in-plane radial motion (s-direction) of the TM is approximated as uniform with a flexible limbal attachment accounting for the deflection. The Hensen stripe introduces additional computational complexities that are not included in the current study.

The fluid-structure interaction in the STS has been reduced to a set of linearized equations in the frequency domain and the resulting coupled equations are solved for the TM displacement, the fluid pressure, and the IHC HB motion, u_{HB}, as described in Section A of the Supporting Material. We focus on two variables, the displacement of the IHC HB (u_{HB}) and the radial motion of the cross section of the TM (u_{TMS}). The IHC HB motion arises from the resultant of all the forces acting on the bundle. The HB dynamics are dominated by the shear force on the apical tip of the HB and the pressure difference between the STS and sulcus fluids. The transfer function

between the net forces applied to the HB (resolved to the tip, f_{tip}) and u_{HB} is given by

$$\chi(\omega) = \frac{u_{HB}}{f_{tip}}, \tag{3.1}$$

where ω is the angular frequency. The dynamic stiffness is found by solving the coupled matrix equations governing the system response (Eq. A.22 in Supporting Material) due to an external load applied to the HB (f_{tip}). From the fluctuation dissipation theorem [58], the spectral density of the noise force on the HB (S_F) is given by

$$S_F(\omega) = 4k_BTR_{tot} \quad , \tag{3.2}$$

where $R_{tot} = \mathrm{Im}((-i\omega\chi)^{-1})$ and k_BT is the Boltzmann constant times the temperature. This force spectrum can be decomposed into contributions due to viscosity ($S_{F_{visc}}$) and channel clatter ($S_{F_{ch}}$) as

$$S_{F_{visc}}(\omega) = 4k_BTR_{visc}, \tag{3.3a}$$

$$S_{F_{ch}}(\omega) = 4k_BT\frac{R^0_{ch}}{(1+\omega^2\tau_c^2)} = 4k_BTR_{ch}, \tag{3.3b}$$

where $R_{tot} = R_{visc} + R_{ch}$, $R^0_{ch} = \frac{\tau_c N k_{gs}^2 d^2 \gamma_{HB}^2 P(1-P)}{k_BT}$ as derived in [95, 9]. Here P is the average open probability of the N transduction channels at rest, $k_{gs}d$ is the single channel gating force, γ_{HB} is the geometric gain, and τ_c is the channel correlation time. We only include channel gating in our model and not the effect of the channel being embedded inside of an elastic membrane [110],[109]. Such an arrangement may also produce additional noise on the channel, increasing the thresholds. The values for the parameters are given in Tab. A.1. The total noise force acting on the HB is a sum of the viscous and channel noise, $S_F = S_{F_{visc}} + S_{F_{ch}}$ as these noise forces are uncorrelated. The power spectral density of the HB response to these forces is given

by [58]

$$S_{u_{HB}^{noise}} = |\chi|^2 (S_{F_{visc}} + S_{F_{ch}}) \tag{3.4}$$

3.3 Results

3.3.1 Noise and sensitivity of nominal HB

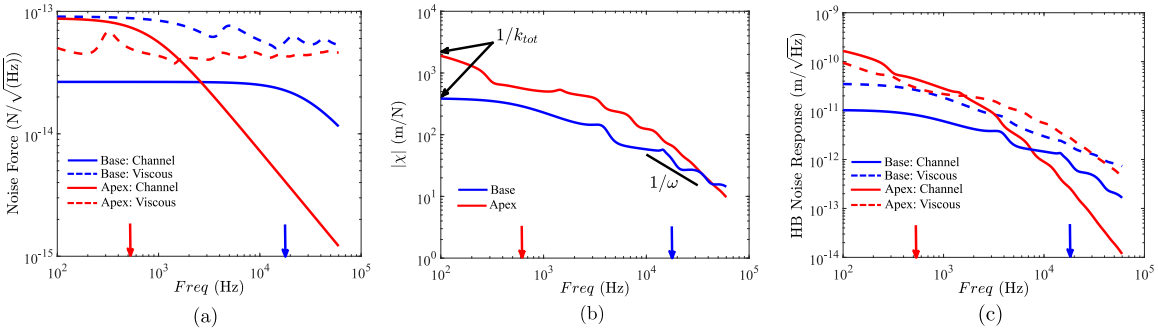

Figure 3.2: The mechanical effects of viscous and channel noise to the HB response at the base and apex of the cochlea. Blue curves refer to the basal locations whereas red curves refer to the apical location. (a) The amplitude spectral density of the noise force due to the viscous noise force (dashed lines $\sqrt{S_{F_{visc}}} = \sqrt{4k_BTR_{visc}}$) and the channel noise force (solid lines $\sqrt{S_{F_{ch}}} = \sqrt{4k_BTR_{ch}}$). (b) The HB sensitivity (χ) at the base and apex. The high frequency slope of χ approaches the slope of the $1/\omega$ curve, shown in solid black line on the same scale. (c) The displacement of the HB due to noise ($\sqrt{S_{u_{HB}^{noise}}}$). The HB displacement due to viscous noise and channel clatter are shown in dashed and solid lines respectively. The total RMS HB displacement is obtained by integrating the entire spectrum and is calculated to be 1.18 nm at the base and 2.72 nm at the apex. The blue and red arrows denote the CF at the base and apex.

The amplitude spectral density of the viscous and channel noise forces acting on the HB at basal (blue lines) and apical (red lines) segments of the gerbil cochlea are shown in Fig. 3.2a. The contributions of the viscous (dashed lines) and channel clatter (solid lines) forces are plotted separately as computed from Eq. 3.3 using the nominal parameters from Tab. A.1. We find that at any location, the viscous force is relatively smooth across frequencies. The local variations in the viscous force spectra are due to damped resonances in the entire STS-sulcus system. The viscous noise is higher for

the basal HBs compared to the apical HBs because the gap between the TM and the HB, assumed to be 5% of the STS height, is smaller at the base (300 nm) than at the apex (900 nm). Unlike the viscous forces which reflect the dynamics of the different elements of the STS, the channel clatter force depends only on the MET channel properties (τ_c in particular) and the geometric factor γ_{HB}. The channel clatter (solid lines) is a low pass filter, limited at high frequencies by the channel correlation time, given by Eq. 3.3b. We have assumed that the channel correlation time is proportional to the characteristic frequency (CF) of the place [121]. Therefore τ_c increases from base to apex (see Tab. A.1). Although γ_{HB} decreases from base to the apex [57], the product $\gamma_{HB}^2\tau_c$ increases from base to apex resulting in an increase in channel noise force at the apex (Eq. 3.3b).

The frequency dependence of the HB sensitivity ($|\chi|$) is shown in Fig. 3.2b. Although the frequency dependence of the sensitivity is complex due to the coupling of the HB with the boundary layer in the STS (Eq. A.21 in Supporting Material), asymptotic limits can be used to simplify the system at low and high frequencies. The low frequency asymptote is controlled by the total stiffness $k_{tot} = k_{HB} + k_G$, a combination of the HB tip stiffness (k_{HB}) and the gating stiffness of the MET channels, $k_G = Nk_{gs}\gamma_{HB}^2\left(1 - \frac{k_{gs}d^2P(1-P)}{k_BT\sqrt{1+\omega^2\tau_c^2}}\right)$. The high frequency asymptote is dictated by the total resistance of the system $R_{tot} = R_{visc} + R_{ch}$ and their frequency dependence can be determined from Fig. 3.2a. The low and high frequency asymptotes of the sensitivity curve are

$$\chi(\omega) \simeq \frac{1}{k_{tot}} \simeq \frac{1}{k_{HB} + k_G}, f \ll f_{cor}; \tag{3.5}$$

$$\simeq \frac{1}{-i\omega R_{tot}}, f \gg f_{cor}, \tag{3.6}$$

where f_{cor}, is the corner frequency at which the two approximations meet given by

$f_{cor} = \frac{1}{2\pi}\frac{k_{HB}+k_G}{R_{tot}}$. The corner frequency is less than <1 kHz at base and <100 Hz at apex, lower than the CF at either location. At high frequencies, R_{visc} dominates R_{tot} and is nearly constant (Fig. 3.2a), and consequently the sensitivity falls at least as fast as $1/\omega$ as shown in Fig. 3.2b.

The displacement of the HB in response to the noise force is given by $u_{HB}^{noise} = (S_{u_{HB}^{noise}})^{1/2} = \sqrt{|\chi|^2 S_F}$. The individual contributions to the displacement of the HB by the viscous and channel clatter forces are plotted separately in Fig. 3.2c using dashed and solid lines respectively with all components displaying a low–pass behavior. The low–pass nature of HB displacement due to channel noise is evident from low–pass nature of the force itself, $S_{F_{ch}}$, in Eq. 3.3b, and that of the HB sensitivity 3.2b. The viscous noise force also gives rise to a low–pass behavior because of the dependence of the sensitivity on ω^{-1} for $f \gg f_{cor}$ at high frequencies, but falls off less rapidly than the channel–noise induced motion because of the near constancy of the viscous noise force (also commented upon by [27]. The asymptotic values of the total HB response to noise (u_{HB}^{noise}) can be calculated from Eq. 3.4, and Eq. 3.5 and 3.6, and are given by $\mathrm{u}_{HB}^{noise} \simeq \sqrt{\frac{4k_BTR_{tot}}{(k_{HB}+k_G)^2}}\mathrm{f} \ll f_{cor}$,
$\sqrt{\frac{4k_BT}{\omega^2 R_{tot}}}\mathrm{f} \gg f_{cor}$. These limiting values give a more succinct view of the complex interaction driving the noise response of the HB. At low frequencies ($f << f_{cor}$), the displacement of the HB due to noise (u_{HB}^{noise}) is proportional to $\sqrt{R_{tot}}$ because the sensitivity of the HB (χ) is stiffness controlled in this limit (Eq. 3.5). At high frequencies ($f \gg f_{cor}$), both the sensitivity of the HBs (χ) (Eq. 3.6) and the noise force (Fig. 3.2a) are resistance controlled and consequently we get the counterintuitive result that u_{HB}^{noise} is inversely proportional to $\sqrt{R_{tot}}$ (Eq. 3.3.1).

The HB displacement spectra due to different noise sources (Fig. 3.2c) has been integrated to yield the RMS hair bundle deflection. The RMS deflection at the base is calculated to be 0.3 nm from the channel clatter and 1.15 nm from viscous drag. At the apex the RMS deflections are considerably higher due to the reduced stiffness of

the HB, amounting to 2.1 nm from the channel clatter and 1.73 nm from viscous drag. Thus the viscous noise is higher than the channel noise at the base and is less than the channel noise at the apex. These results reflect a cross-over from viscous dominated noise at the base to channel clatter dominated noise at the apex. The shape of the spectrum of the HB motion we predict is similar to that measured by [27].[152] find an RMS bundle motion of 2 nm for a undisturbed OHC bundle dissociated from the TM (possibly higher levels might be seen if the bundle is biased closer to its putative operating point).

3.3.2 Threshold TM Radial Motion

The OHC HBs apply radial forces at the outer portion of the TM causing the TM to displace in the radial direction, shearing the STS fluid and displacing the IHC HBs. The transfer function between the shear motion of the TM and the HB displacement is given by $H_{TMS}^{HB} = \frac{u_{HB}}{u_{TMS}}$. The amplitude of H_{TMS}^{HB} at the base and apex are shown in Fig. 3.3 using blue and red lines respectively. At low frequencies (below f_{cor}), the dynamic stiffness of the HB is dominated by $k_{HB} + k_G$ (see Eq. 3.5) and the net force on the HB is proportional to the TM shear velocity. Consequently, the transfer function, H_{TMS}^{HB}, scales linearly with frequency and is in phase with the TM velocity. This can be most clearly seen in the basal HB (blue curve in Fig. 3.3). At higher frequencies, the the impedance is mainly resistive and the velocity dependent and now stronger shear force from the boundary layer "locks" the HB in–phase with the TM. At these frequencies, the HB motion follows the TM displacement with almost the same amplitude and phase. Hence, the HB displacement is in phase with the TM velocity at low frequencies and in phase with the TM displacement at high frequencies [111]. The fluctuations in the sensitivity spectra in Fig. 3.3a are due to damped resonances in the STS system.

The threshold TM radial motion required to stimulate the HB above its noise level

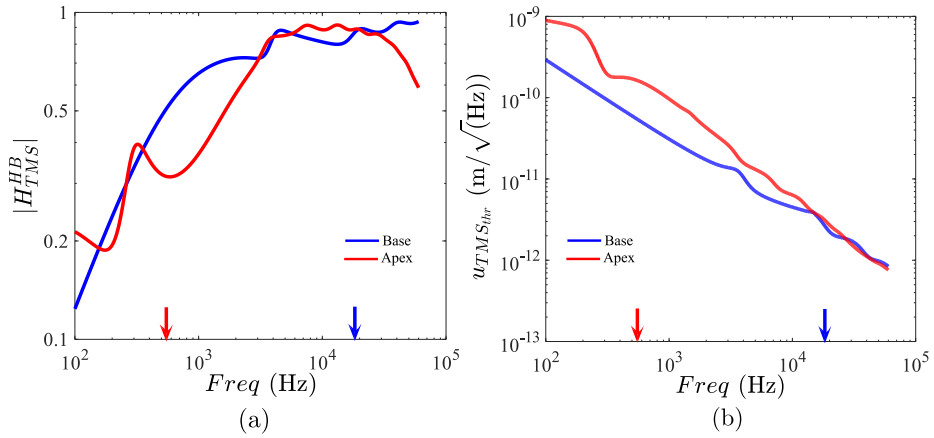

Figure 3.3: The HB sensitivity to TM radial motion and the TM threshold motion. (a) H_{TMS}^{HB} for a basal and an apical HB. The sensitivity for the basal HB is shown in blue whereas that for the apical HB is shown in red. (b) The TM threshold shear displacement required to elicit a HB response above the baseline noise level are shown in blue lines at the base and red lines at the apex. The arrows indicate the CFs at the base and apex.

(Fig. 3.2c) is given by

$$u_{TMS_{thr}} = \frac{|u_{HB}^{noise}|}{|H_{TMS}^{HB}|}, \tag{3.7}$$

and is shown in Fig. 3.3b with a blue line at the base and a red line at the apex. The threshold TM motion in the radial direction is 5 pm at the CF of the base and 0.1 nm at the CF of the apex.

3.3.3 Tall Hair Bundles Have the Lowest Shear Thresholds

Figs. 3.4a and 3.4c show the dependence of total noise force ($\sqrt{S_F}$) on the HB height for a basal and apical HB respectively. We study the effect of HB height on the noise and displacement response by considering HBs of nominal height h (solid lines), $0.75h$ (dash dot lines) and $0.5h$ (dotted lines), while keeping the height of the STS space (g_0) constant (i.e., we are varying the gap between the HB tip and the TM). Other properties which depend on HB height are γ, which goes like $1/h$ because of geometric constraints [57] and k_{HB} which varies like $1/h^2$ because we have assumed

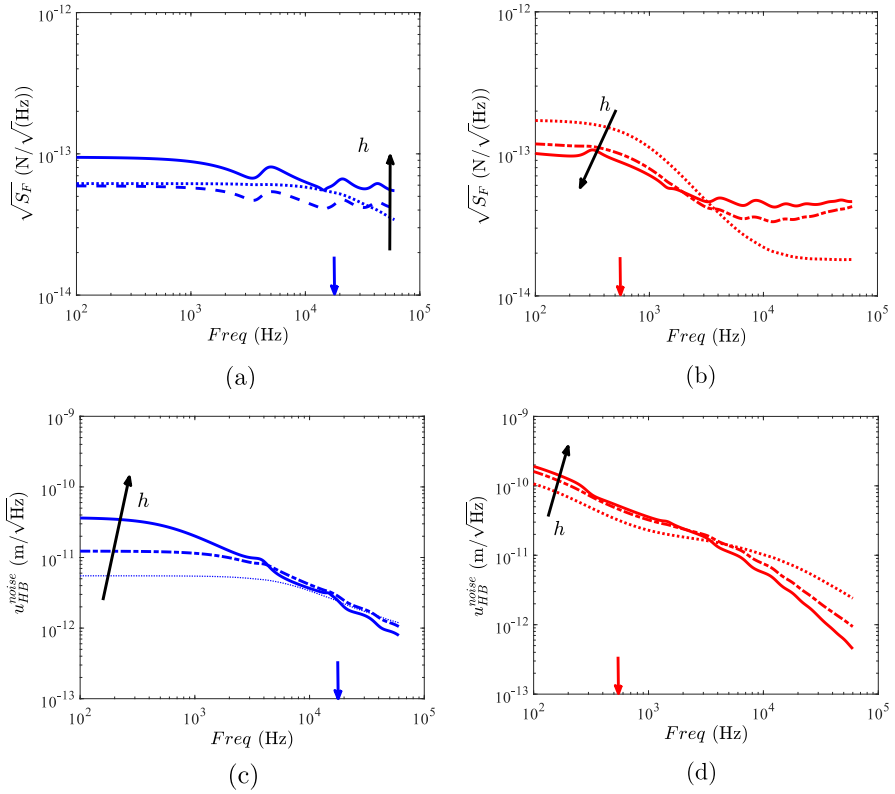

Figure 3.4: The variation of noise force spectrum and the displacement spectrum of the HB due to noise with change in height of the HB. Solid lines denote nominal height h, and dash-dot lines and dotted lines indicate HB of height $0.75h$ and $0.5h$ respectively. (a) At the base, the noise force on the HB of nominal height, h, is primarily viscous. As the bundle height is decreased to $0.75h$ keeping the STS gap constant, the total noise force falls. However, below $0.75h$, the channel clatter becomes dominant and the total noise force increases again as the HB height is lowered to $0.5h$. (b) At the apex, decreasing HB height further increases channel noise force below the cross-over frequency where viscous forces dominate channel clatter and the trend reverses and the taller HBs have greater noise forces. (c,d) The HB displacement spectra at the base and apex depends on the interplay between the noise forces and the tip sensitivity χ. The arrows on the frequency axes denote the CF of the location.

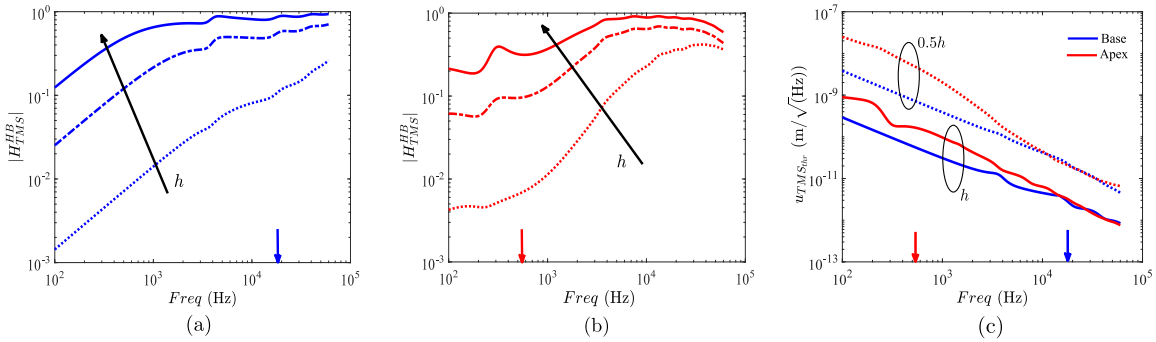

Figure 3.5: The variation of H^{HB}_{TMS} and $u_{TMS_{thr}}$ on height of the HB at the base and apex. The sensitivty for the HB of nominal height, h, is shown with solid lines for the (a) basal and (b) apical locations. The sensitivity for the HBs with height $0.75h$ and $0.5h$ are shown with dash-dot and dotted lines respectively. The dramatic decrease in sensitivity for the shorter HB reflects the loss of coupling between the underside of the TM and the HB as the Stokes shear layer weakens exponentially with distance from the TM. (c) The threshold TM radial motion, $u_{TMS_{thr}}$, for the basal HB is shown in blue whereas that for the apical HB is shown in red. The thresolds for the HB of nominal height, h, is shown with solid lines whereas the thresholds for the HB with height $0.5h$ is shown with dotted lines. Although the shorter HB incur lower viscous noise, the increased threshold displacement is due loss of sensitivity owing to weakened shear coupling between the TM and the HB.

that the moment stiffness at the pivot remains constant as we change the height.

The noise on the nominal basal HB (Fig. 3.4a) is primarily viscous over the entire frequency range (as shown in Fig. 3.2a). Decreasing the HB height to $0.75h$ reduces the viscous drag from the Stokes layer attached to the TM, causing a reduction of the total noise force. Reducing the HB height by 50% or more of the nominal height results in $R_{ch} > R_{visc}$ over the entire frequency range (see dotted lines in Figs. 3.4a). This is because as h decreases the viscous noise force reduces (as the HB moves outside the TM boundary layer) and the channel noise force increases (because $\sqrt{S_{F_{ch}}}$ is proportional to γ_{HB} which is inversely proportional to the HB height). For all apical HB heights (Fig. 3.4c), the noise force is channel dominated below about 3 kHz and depends inversely on HB height. Above this frequency, the viscous force becomes greater than the channel force. In this higher frequency range, the taller HB experiences a greater force because of insertion of the HB tip into the TM boundary

layer; therefore the noise force increases with HB height.

The noise–force induced HB displacement (u_{HB}^{noise}) for a basal HB is shown in Fig. 3.4b and for an apical HB in Fig. 3.4d. The displacement spectrum of the HB is a product of the noise force (Figs. 3.4a,3.4c) and the sensitivity of the HB to these forces (Eqs. 3.5,3.6). For the viscous–force dominated basal HB (Fig. 3.4b) below 1 kHz, where Eq. 3.3.1 holds, a reduction of the HB height accompanies a reduction in u_{HB}^{noise} because the stiffness increases, since $k_{HB} \propto 1/h^2$. For an apical HB, the corner frequency (f_{cor}) is less than 100 Hz and Eq. 3.3.1 holds. Therefore, u_{HB}^{noise} is R_{tot} controlled throughout the spectrum and an increase in resistance reduces the noise response. Since channel resistance (R_{ch}) dominates the low frequency resistance spectrum (Fig. 3.2a), decreasing the HB height increases R_{tot}, decreasing u_{HB}^{noise} at frequencies below 3 kHz. Above 3 kHz, viscous forces surpass channel forces and the trend reverses, with shorter HBs experiencing lower resistance and therefore a higher noise response. Overall, note that at the CF of both basal and apical locations, the u_{HB}^{noise} is relatively insensitive to the ratio of the HB height (h) to the height of the STS gap (g_0).

In contrast with u_{HB}^{noise}, there is a strong dependence of the HB sensitivity to TM radial motion (H_{HB}^{TMS}) on the HB height (h) as shown in Fig. 3.5a and Fig. 3.5b for the basal and apical HBs, respectively. H_{HB}^{TMS} of the shorter bundle is two orders of magnitude smaller than that of the taller bundle. Two factors give rise to this reduction. The first is that the shear coupling decreases exponentially with increasing distance between the TM and the tip of the HB. Second, the pressure differential across the HB falls as the HB height is decreased because the flow resistance in the gap between the TM and the tip of the HB is likewise reduced. The balance between noise and sensitivity with changing HB height can be best understood through the TM threshold motion, $u_{TMS_{thr}}$ (Eq. 3.7). In Fig. 3.5, the TM threshold displacement for the nominal bundles at the base and apex (shown in blue and red solid lines

respectively) are compared with those for the half height bundles (shown in dotted lines). Even though the shorter HB experiences a lower noise force, the dramatic loss in H_{HB}^{TMS} leads to the TM threshold for the shorter bundle being an order of magnitude higher than the taller bundle both at the base and the apex. Hence, for the TM shear stimulus, the threshold is primarily controlled by the shear sensitivity and the taller bundle, in spite of incurring a higher viscous noise force, is preferable from a sensor design point of view.

The effect of factors other than HB height were explored as to their effect on $u_{TMS_{thr}}$. A parametric study was done to investigate the effect of changing TM bending rigidity. In this study, the TM is assumed to be an isotropic solid which is characterized solely by its Young's modulus (E_{TM}). We simulated the noise spectrum (not shown) for a range of E_{TM} and found a weak variation of the HB displacement due to noise with TM stiffness. Also, the rigidity of the TM had little effect on the sensitivity of the HB to TM radial motion (H_{TMS}^{HB}) because the transverse motion of the TM does not play a major role in the generation of shear force by the Stokes boundary layer. We also varied the open probability (P). When P is reduced from 0.4 to 0.1, the TM–shear threshold for the viscous-noise dominated basal HB was not altered. For the channel–noise dominated apical HB, a reduction of the open probability was accompanied by a less than 20% decrease in the threshold only at low frequencies because of the lower channel noise force. Finally, increasing the HB stiffness (k_{HB}) had almost no effect on the threshold for either basal or apical HBs. This because the reduction in sensitivity to TM motion was balanced by a reduction in the response to the noise stimulus.

3.3.4 Effect of HB activity on noise and thresholds

We implemented the active HB model from [150] by linearizing the equations about the operating point of the HB complex corresponding to the resting open

channel probability of $P = 0.4$ (Section B of Supporting Material). For the choice of parameters used, the active bundle generates energy providing negative resistance to the system. This negative resistance reduces the net effective hydrodynamic drag on the hair bundles. The channel noise is not affected by the active process as the inherent stochasticity of the MET channels remain unaffected. The reduction in noise is accompanied by a corresponding reduction in TM threshold motion ($\Delta u_{TMS_{thr}}$). Fig. 3.6 shows the percent decrease in TM threshold $\left(\frac{\Delta u_{TMS_{thr}}}{u^{pas}_{TMS_{thr}}} \times 100\right)$ for the active HB with respect to the passive bundle, at the base and the apex. The low frequency threshold is reduced by 10-25% due to the active process, whereas the high frequency threshold is reduced by less than 5%. The peaks in the threshold predictions are due to a frequency shift in the peak response of the HB to TM radial motion.

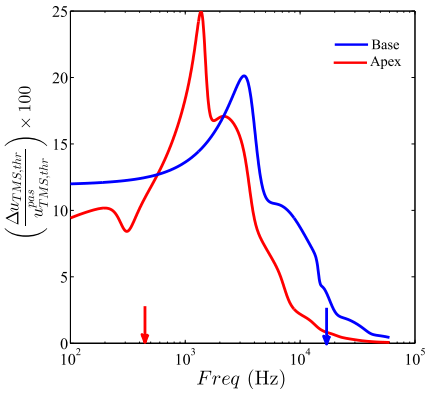

Figure 3.6: The percent reduction in TM radial displacement threshold of the STS model with active HB ($u^{act}_{TMS_{thr}}$) with respect to the STS model with passive HB ($u^{pas}_{TMS_{thr}}$). Addition of hair bundle activity reduces the effective hydrodynamic drag on the hair bundle, decreasing the TM shear displacement threshold by $\Delta u_{TMS_{thr}} = u^{pas}_{TMS_{thr}} - u^{act}_{TMS_{thr}}$.

3.4 Discussion

3.4.1 Comparing model predictions to experiments

Our model makes predictions of the TM shear motion needed to stimulate the IHC HB motion above the levels induced by noise forces alone (Fig. 3.3). To test our

model, we compare these predictions with experimental data of mechanical motion at the base and apex. First we consider the basal, high frequency region (near 18 kHz). There, the threshold TM radial motion predicted from our model is around 5 pm for the CF at the base (Fig. 3.5). Most experiments at the base of the cochlea measure BM transverse motion and not the radial motion of the TM at threshold. To compare the two, we use a kinematic mathematical model [114] to translate the TM shear to an equivalent to the BM transverse motion; the result of this calculation is a factor of two or a threshold BM displacement of 10 pm. Optical coherence tomography (OCT) experiments by Chen et. al. [11] at the base of the guinea pig cochlea (with a CF of 18.8 kHz) have shown that the BM deflection is around 40 pm in response to to 20 dB SPL (the threshold of hearing for the guinea pig at this frequency [53]). Hence, the experimental value is four times greater than the threshold BM displacement prediction of 10 pm from our model. However, our estimate of TM shear thresholds underpredict the actual thresholds since we have not included other sources of noise in our reductionist model. Noise contributions that are present *in vivo*, such as losses in the ear canal, middle ear, outer hair cells and intracochlear signal propagation may reduce the 12 dB difference between the measured and predicted thresholds. Hence, this result does imply that shear sensing is a viable approach to high frequency hearing as hypothesized by most experimentalists and inherent to most models [3], because there is room in the noise budget for sensing at physiological displacement levels.

Fridberger, et al. [39] measured the OHC HB radial (shear) motion at the apex of an *in vitro* preparation. This measurement corresponds to the shear motion of the TM in our model (because we use a shadow coordinate frame attached to the TM). At 200 Hz, the OHC HB radial displacement is around 28 nm in response to 98 dB SPL at the apex of the guinea pig cochlea. To obtain a lower bound on the threshold radial TM motion, we scale the OHC HB radial displacement linearly from 98 dB SPL to 41 dB SPL, the threshold for hearing at 200 Hz in the guinea

pig [53]. This yields an estimate of the threshold OHC HB radial displacement of 0.04 nm uncorrected for cochlear compression. From the measurements at the apical turn of a guinea pig cochlea [115], we might expect a factor of 6 to account for the non-linear compression *in vivo*, increasing the experimental threshold estimate to 0.24 nm, less than the 0.6 nm TM threshold displacement predicted by the apical HB model at 200 Hz (Fig. 3.3). Hence the model threshold prediction exceeds the threshold observed *in vivo*, leaving no additional room in the noise budget. This may indicate the presence of alternate modes of stimulation that function separately or in conjunction with the shear mode. One possible candidate for such low frequency stimulation could be the fluid pressure driven pulsatile flow in the STS gap [102]. Such a stimulation mechanism could impart a high HB sensitivity at lower frequencies resulting in reduced low-frequency acoustic thresholds.

3.4.2 Couette flow underestimates damping

Because of its simplicity compared to the model presented in this paper, the Couette flow assumption is often used in the STS [38, 88] to estimate the effect of fluid viscosity on the motion of the cochlear structures. These models underestimate the damping in the mammalian cochlea because they ignore the coupling of the fluid flow with the IHC and OHC HBs as well as oversimplifying the flow in the STS space between the OHCs and IHCs. For instance, the net damping on the gross motion of the TM due to the shearing of the TM relative to the RL is an important quantity because it is a dominant damping force affecting the OHC HB motion. As such, it is a crucial quantity in macroscopic cochlear models, such as [88]. Computing the frequency independent TM damping coefficients from a Couette flow profile alone (and neglecting the effect of the flow around the IHC and OHC HBs) yields values of 114 $\mathrm{nN\,m^{-1}\,s}$ at the base and 108 $\mathrm{nN\,m^{-1}\,s}$ at the apex. Using the more complete model presented here, the TM damping coefficients for shear motion are found to be

411 nN m^{-1} s at the CF of the basal location and 191 nN m^{-1} s at the CF of the apical location, 3.6 and 1.8 times higher than those obtained from Couette flow estimates. In particular, the damping associated with the flow over the IHC HB significantly influences the macroscopic response of the cochlea.

As in [111] we find that the low frequency damping experienced by a IHC HB is also underestimated by a Couette flow approximation. The HB resistance at 100 Hz obtained from a simple Couette flow assumption over the tips of the HBs at the cochlear base and apex are 28.5 nN m^{-1} s and 11.3 nN m^{-1} s respectively. The resistances at 100 Hz computed using the more complete model with Stokes flow along with channel-related damping ($S_F/(4k_BT)$, Eq. 3.3) are 542 nN m^{-1} s at the base and 600 nN m^{-1} s at the apex respectively, considerably higher than the simple Couette flow predictions mainly due to the added channel damping [9]. This damping underestimate would not only contribute to the overall damping of the system but could also be important when estimating the IHC HB motion induced changes to the polarity of the IHC cell body through changes in the channel conductance and ultimately to the input to the auditory nerve.

Hence we conclude that modeling the STS is necessary to estimate the proper damping in the cochlea. The finite element method can be used to create a detailed model to simulate the complex fluid-structure interactions in the STS as well as the dynamics of the global cochlear system. However, the discretization requirements at the dramatically different length scales in a global model, namely milimeter scale global geometries and the sub-micron scale IHC HB-TM gap would lead to very expensive computations. This would make variation of stimulation parameters necessary for scientific discovery of important mechanisms (e.g., OHC somatic versus HB motility) difficult. Furthermore, resolving these disparate scales in nonlinear simulations (e.g., two-tone interactions) at a variety of frequencies and conditions would likewise be nearly impossible even with large scale computational resources. An alternative

approach is to use a semi-analytic model in the STS like the one suggested in this study and couple it (or appropriate simplifications thereof) to a global finite element model to produce more accurate results without a large increase in the computational cost.

3.4.3 Displacement noise of the IHC HB

The focus of this paper is on the noise–induced mechanical motion of the HB and the associated TM threshold displacement. Although the effect of varying the HB height on the noise and threshold were discussed in detail, similar studies were done by varying the HB stereocilia pivot stiffness and the MET resting probability. We found that increasing the HB stiffness (k_{HB}) reduces the HB displacement due to noise as expected. Decreasing the MET channel resting probability reduces the channel clatter as well as the gating compliance, decreasing the HB displacement fluctuation. However, the threshold TM motion is relatively insensitive to alterations of the HB stiffness (k_{HB}) or the resting open probability (P) because the change in the sensitivity of the HB affects its transduction of the signal as well as the noise. The MET channel correlation time, τ_c, at any location limits the maximum frequency the HBs can accurately transduce and it must be less than the inverse of the maximum frequency it is trying to transduce. Extrapolating from existing data in turtles and rats [120, 121], we also hypothesize that the channel correlation time varies with location (and hence the CF). In the absence of experimental values of the channel correlation time for the gerbil cochlea, we used a conservative estimate of one tenth of the inverse of the CF of the location (see Tab. A.1). This choice safely puts the low–pass filter cutoff for the channel out of band for the CF at the given location. From a noise perspective, increasing the channel correlation time increases the low frequency channel resistance (and noise) but decreases the corner frequency in the channel resistance spectrum (Fig. 3.2b solid lines). Hence there exists a tradeoff; a

shorter correlation time reduces the noise from the channel itself but broadens the transduction filter [121] rendering the HB vulnerable to higher frequency noise. For the nominal parameters chosen in this study (Tab. A.1), the lower τ_c and higher viscous drag at the base compared to the apex results in viscous forces dominating the noise spectrum at the base and channel clatter dominated noise spectrum at the apex.

Although a complete study of the current and the IHC depolarization warrants a more complete study as in Poveda et al, [81], an estimate of the transduced current noise can be calculated by assuming a current sensitivity of 26 $\mathrm{pA\,nm^{-1}}$ at the base and 15 $\mathrm{pA\,nm^{-1}}$ at the apex [62]. This gives a DC current noise of around 0.94 $\mathrm{pA}/\sqrt{\mathrm{Hz}}$ at the base and 2.8 $\mathrm{pA}/\sqrt{\mathrm{Hz}}$ at the apex. Note that the current noise at DC frequency due to basolateral conductance of the OHC is 0.028 $\mathrm{pA}/\sqrt{\mathrm{Hz}}$ (using the conductance of 50 nS measured by Johnson, Marcotti et al [63]), and that due to the MET channels conductance is 0.022 $\mathrm{pA}/\sqrt{\mathrm{Hz}}$ (using a channel conductance of 30.1 nS as measured by Jia, Dallos et al. [62]). Hence the transduced current noise is greater or at least comparable to the thermal noise from the basolateral membrane and the MET conductance.

Further, the hydrodynamic drag of the HB can be reduced by HB activity as discussed in [111]. The phenomenological model used in this study assumes a molecular motor based tip-link tensioning mechanism modulated by the conductance of the MET channels [95]. In the parameter regime used in this study, the HB adaptation coupled with the right timing, adds energy to the HB on a cycle by cycle basis to overcome the damping in the STS. However, this energy addition is limited to low frequencies [147] by the latency of the adaptation motor activation. The effective hydrodynamic drag on the HB is reduced by the HB motility, increasing the sensitivity of the HB (Eqs. 3.5 and 3.6) leading to a reduction in thresholds (Fig. 3.6) at low frequencies for the active HB. Although the active force generation in the mammalian

cochlea is thought to be primarily mediated by the OHC somatic motility and the OHC HB activity, the IHC HBs also exhibit calcium dependent kinetics which could potentially generate active force. We speculate that such an active process in the IHC HBs may play a role in maintaining lower thresholds of hearing, and if compromised, could lead to increased thresholds.

We find that the height of the bundle plays a key role in IHC sensory effectiveness to shear motion. Although the taller HB incurs a higher noise-inducing viscous drag, the stronger coupling to the TM through the Stokes boundary layer increases the HB sensitivity and ensures a low threshold TM displacement. While the shorter bundle experiences a lower viscous drag, the higher channel clatter and low shear sensitivity (H_{HB}^{TMS}) results in the threshold TM displacement being an order of magnitude higher than that of its taller counterpart, as shown in Fig. 3.5. The threshold TM displacement increased roughly 25 times when the hair bundle height was reduced from the nominal height of 95% of STS gap height to 50% the STS gap height. A similar trend was also observed at the apex. We posit that the profound deafness found in the Eps8 mutant mouse with shortened stereocilia [159] comes at least in part from the reduced IHC HB sensitivity shown here.

CHAPTER IV

Unified Cochlear Model of Low- and High Frequency Mammalian Hearing

4.1 Introduction

The mammalian cochlea acts as an acoustic spectral analyzer because the emergent organ-level dynamics arising from the spatial organization of its morphological, mechanical, electro-chemical, and neural characteristics imparts a base-to-apex gradient of frequency selectivity known as the tonotopic map. The tuning of the sound-induced mechanical response of a key structural element of the cochlea, the basilar membrane (BM), has traditionally been used as a proxy for the auditory nerve fiber (ANF) response because of measured similarities between the two quantities [124]. However, the canonical theory is based on experiments confined to the basal end of the cochlea, and more recent apical measurements have challenged this tenet [157, 115]. For instance, experiments in the apical turn of the guinea pig cochlea using optical coherence tomography (OCT) [157] have shown that the BM response is poorly tuned and does not exhibit the high and non-linear gain seen in the basal turn. Vibrations at a point near the reticular lamina (RL) at the apex does exhibit a 20-30 dB non-linear gain shift from low to high SPL [115] but fails to recreate the V shaped tuning associated with the ANF threshold [148, 31, 17, 115]. The differences between the

mechanical tuning at the base and the apex, as well as the divergence of the mechanical and neural tuning at the apex, has given rise to the notion that the underlying micro-mechanics in the basal part of the mammalian cochlea is different from that of the apex, and there exists a transition from the basal to apical mechanics along the cochlear spiral [136].

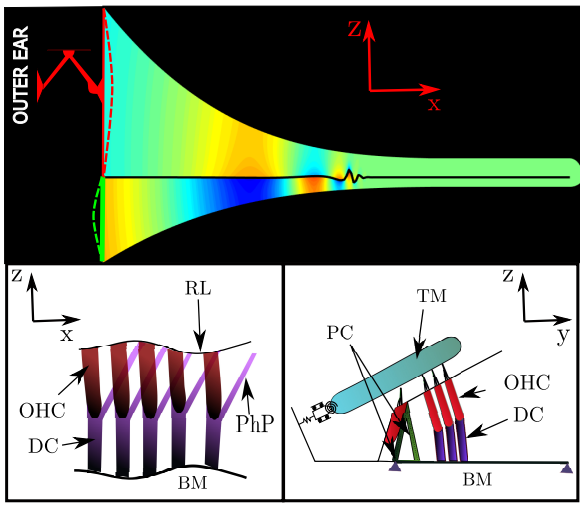

Figure 4.1: Schematic of the model of the guinea pig cochlea. The height of the scala vestibuli and the scala tympani varies from base to apex based on areal measurements of the guinea pig cochlea[33]. The fluid in the scalae has been modeled as compressible and viscous. The stapes and the round window have been modeled as flexible membranes with a single vibrational mode as shown in Fig. 4.1. The OHCs are tilted basally and the PhPs connect the DC body to the apical RL to include the feed-forward effect [158]. The parameters have been tonotopically varied from base to apex based on morphological data, and has been summarized in Appendix B.

Although theoretical and numerical studies have been successful in modeling the basal, high-frequency response of the cochlea [99, 90, 78], few studies have concentrated on modeling the cochlear response at the apex. Recently, a model that includes the feed forward effect from the phalangeal processes has been shown to provide a good fit of the vibration amplitude at the base as well as the apex in the high frequency hearing mouse cochlea [93]. However, the model overestimates the phase accumulation observed *in vivo*, and lacks the mechanics of the TM which has been shown to be an important factor governing the amplification in the cochlea, both

theoretically [87] and experimentally [45, 127]. Other models have shown that the mechanical properties of the BM [35], impedance of the helicotrema [21, 94, 112], and curvature of the cochlea [86] could play a role in low frequency hearing. Reichenbach, et al. [116] proposed a model to account for the loss of BM amplification at the apex by critically tuning the hair bundle and the outer hair cell (OHC) electromotile feedback parameters. However, this model assumes equality of the hair bundle and transverse RL motions, which is inconsistent with experimental data [72] and higher fidelity physiological models [114]. Further, this model assumes that the positive HB deflection leads to the hyperpolarization of the hair cell which is unlikely to be true *in vivo* in the mammalian cochlea. Nevertheless, the model shows a possible mechanism that could decouple the BM from the HB to explain the lack of BM amplification at the apex. Although these previous studies have indicated mechanisms that could be pertinent to low frequency hearing, none has led to the development of a global model of the cochlea that accurately predicts the diversity of gains seen across the entire range of frequencies. In this paper, we develop a physiologically based model that explains the mechanical tuning of the cochlea from base to apex.

4.2 Methods

We have used a 2.5D hybrid-finite element (FE) model of the guinea pig cochlea. Physiological parameters for the guinea pig cochlea have been used wherever possible, and approximations made based on measurements on other animals wherever necessary. The scala vestibuli (SV) and the scala tympani (ST) have been modeled as tapered prismatic ducts, as shown in Fig. 4.1, to accommodate the change in area observed in anatomical measurements of the guinea pig cochlea [33]. The BM has been modeled as an orthotropic plate [79], and the TM has been modeled as a longitudinally coupled viscoelastic beam [87]. The fluid viscosity has been incorporated in the SV and the ST through viscous corrections [13] for efficient computation. A

complete formulation and the list of parameters has been included in the *Appendix*.

4.3 Results

4.3.1 Unified model for the Base and the Apex

We have compared the model predictions of the BM gain and phase spectra with the experimental data obtained at the basal turn of the guinea pig cochlea. Fig. 4.2a and 4.2b show the model predictions of the BM gain and phase with respect to the stapes at 3.9 mm (CF: 16.3 kHz) from the stapes. The solid blue line shows the BM gain for the active model, and the blue dashed lines shows the BM gain for the passive model. The experimental results from [26] have been overlaid for comparison, with blue diamonds showing the BM gain at 20 dB SPL stimulus (equivalent to the active model), and the blue circles correspond to the BM gain at 100 dB SPL in a dead animal (equivalent to the passive model). The solid arrows show the CF of the location and the dashed arrows show the frequency of maximum gain for the passive BM. Both model and experimental gains have been normalized to their corresponding peak passive gains and the correspondence is stiking. The model shows a remarkable match with the experiments, with the active BM response exhibiting a 27-30 dB gain over the passive BM response at CF, and a phase accumulation of approximately 2 cycles in the active case and 1 cycle in the passive case.

Figs. 4.2(c,d) show the model predictions of the BM and RL displacement gain and phase spectra at 3.9 mm from the stapes. The solid blue line shows the BM gain spectrum and the solid red line shows the RL gain spectrum for the active model. The corresponding passive responses are shown with dashed lines. In the passive model, the RL displacement motion is similar to that of the BM, and the RL moves in phase with the BM at all frequencies. In the active model, the RL motion is approximately 13 dB more than that of the BM at 0.3 CF, and is out of phase with the BM motion,

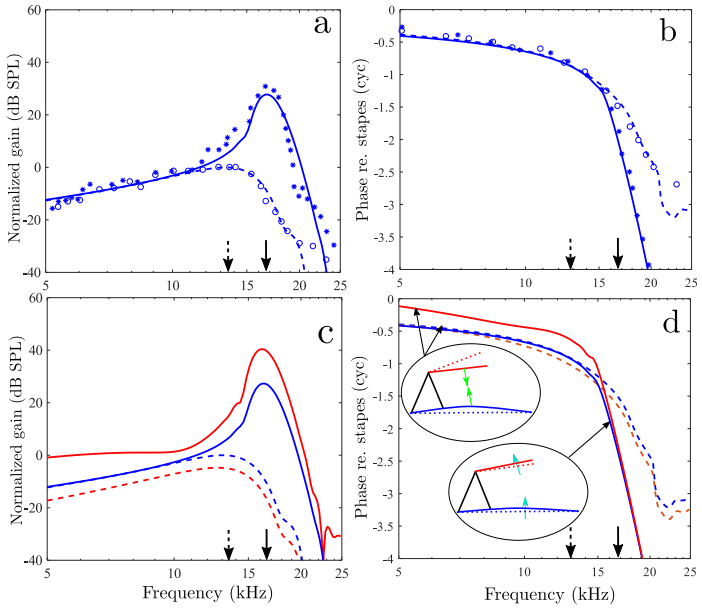

Figure 4.2: Comparison of model predictions with experiments at 3.9 mm from the stapes in the guinea pig cochlea.(a, b) shows the gain and phase of the BM in the active (solid blue line) and passive (dashed blue line) model of the cochlea. The symbols show the response at 20 dB SPL and 100 dB SPL from [26]. (c,d) shows the prediction of the BM and the RL gain and phase for the active (solid lines) and passive (dashed lines) model. The blue and red lines correspond to the BM and RL respectively. In the active model, the RL moves out of phase with the BM at low frequencies and transitions to moving in phase close to the CF, whereas in the passive model it moves in phase with the BM at all frequencies, as shown in the insets. Further, the active model predicts a RL gain that is 11 dB higher than that predicted by the passive model at 0.5 CF, in line with observations from [118]. The model and experimental gains have been normalized to their corresponding peak passive BM gains. The solid arrows show the CF of the location and the dashed arrows show the frequency of maximum gain for the passive BM.

in line with experimental observations in guinea pig [11], gerbil [51], and mouse [118].

We wanted to explore the generality of our model BM response by comparing the model results to the BM response of a different animal from a different research group. Fig. 4.3 shows the comparison of the model results (lines) with the parameters used in the main text (given in Appendix B, Tab. B(1–3)). The experimental data from [18] is shown with symbols. The peak BM gain from the model (blue lines) matched well with the BM gain at 40 dB SPL from the experiment (squares) and was 10 dB lower than the BM gain at 20 dB (circles) observed in the experiment. The lower BM gain from the model is due to the value of the parameters chosen to fit to the experimental data from [26]. The animal used by de Boer and Nuttall may have been less sensitive than that of the Cooper and Rhode preparation. Increasing the electromechanical parameter, ϵ_3, by 7% and 5% respectively (which represents an animal with higher sensitivity in the experimental preparation) resulted in good match with the experimental data at 20 dB and 30 dB SPL stimulation as shown in Fig. 4.3 with the green and red lines. The BM phase from the model is in good agreement with the experimental data at 20-40 dB SPL.

Figs. 4.4 shows the model predictions of the RL displacement at 75%, 80%, 92%, and 95% the length of the cochlear partition from the stapes. The solid red lines show the amplitude of the gain of the RL in the active model of the cochlea and the dashed red lines correspond to the RL gain in the passive model. The responses are normalized to the peak RL gain for the passive model for each case. The has been overlaid for comparison. The symbols show the RL gain spectra at 20 and 76 dB SPL measured using OCT [115] at the apical turn of the guinea pig cochlea. The RL gain spectrum from the model transitions from a band-pass filter at 75% from the stapes to low-pass at 95% from the stapes, reflecting the transition seen in experiments. Further, the peak active RL displacement gain spectrum is approximately 15-20 dB higher than the peak passive response. The phase accumulation from the model is

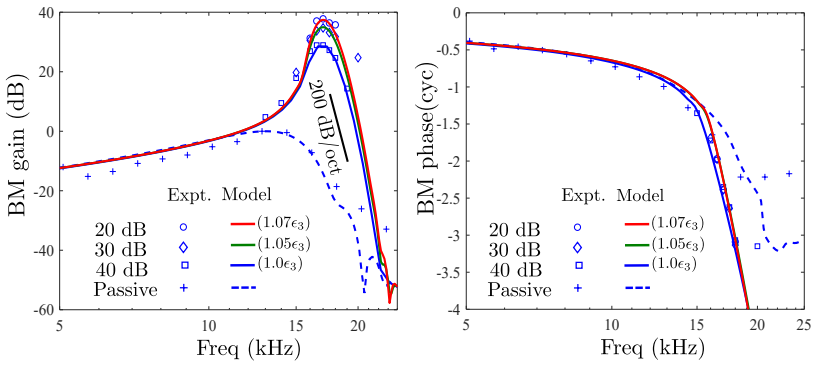

Figure 4.3: Comparison of model results with experimental data from Cooper and Rhode [18]. The solid blue lines shows the results from the model with parameters fitted to [26]. The symbols show the experimental data. The active BM gain obtained from the model matches the BM gain when the cochlea is stimulated with 40 dB SPL. Increasing the electromechanical coupling parameter ϵ_3 by 7% and 5% to reflect a more sensitive preparation (red and green lines) results in a good fit with the experimental data at 20 dB (circles) and 30 dB (diamonds) SPL (Thanks to Nigel Cooper for providing the unpublished phase data from this study). The phase spectra from our model results is in good agreement with both the active and the passive phase from experiments.

around 1 cycle at CF and 3 cycles at the high frequency plateau, similar to that seen in experiments [17, 115].

4.3.2 Response to Electrical Stimulation

To explore the relative motion of the BM and the RL *in vivo* at the apex, we simulated the response of the RL and the BM to electrical stimuli in the active model. Fig.4.5 shows the displacement of the RL and the BM at 11 mm from the stapes window due to an unipolar current sweep from -5 μA to 5 μA in the scala media. The experimental data from Warren et al. [157] has been overlaid for comparison. Both the model and experimental data have been normalized by the corresponding RL displacement at 5 μA. The BM displacement was negligible compared to the RL displacement and was out of phase with the RL displacement, in line with the observations from [157] and [85]. We found that the asymmetry of the RL response to positive and negative current was due to the initial onset of the current stimulus,

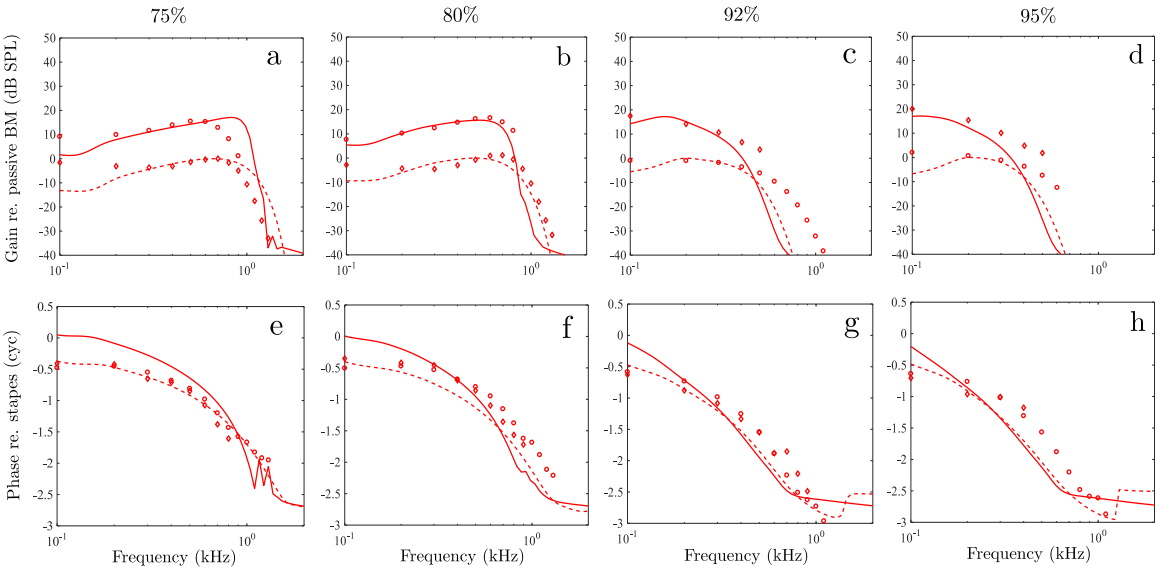

Figure 4.4: Panoramic view of the apical tuning. (a-d) shows the RL gain at 75%, 80%, 92% and 95% of the length of the cochlear partition from the stapes. The solid red lines show the RL gain in the active model whereas the dashed red lines show the RL gain in the passive model. The symbols show the gain seen in experiment by Recio-Spinoso et al. [115] at 20 dB SPL (diamonds) and 76 dB SPL (circles). (e-h) shows the corresponding phase spectrum at different distances from the stapes. We see that the RL gain transitions from band-pass to low-pass at the apex. All gains have been normalized to the passive RL gain. The experimental data show a CF that is not strictly tonotopic as the CF at 75% is less than the CF at 80%. Such trends cannot be recreated by our model where exponential variation of dynamic parameters have been assumed throughout the cochlea.

and can be systematically varied by changing the onset time. Nonlinear effects such as saturation and adaptation during negative current stimulation may also play a role in the experiment, but was not explored in this work.

4.3.3 Base to Apex Transition in Neural Tuning

We have extended the predictions of the mechanical tuning of the model to the tuning of the ANFs by using the model described in Appendix B to formulate the transfer function between the TM radial shear and the stimulation to the ANF. The solid black lines in Fig 4.6(a-c) show the model prediction of the frequency tuning curves (FTCs) of the IHC HB radial tip deflection at the basal (20, 25, and 30% the

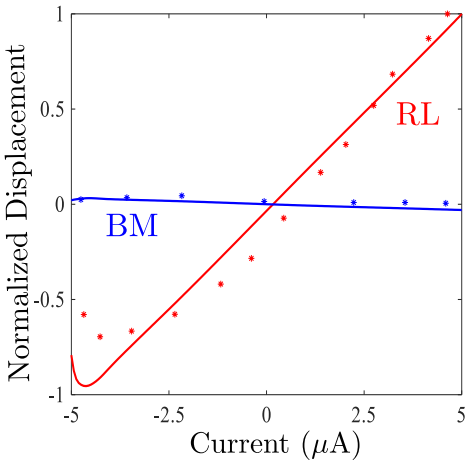

Figure 4.5: Response of the RL and the BM to unipolar electrical stimulation in the scala media. The stimulus was chosen to be a -5 μA to 5 μA current ramp over 50 ms, with onset and offset time of 5 ms. The displacement has been normalized to the peak RL displacement. The current evoked RL motion is much higher than the BM motion due to the lower RL stiffness as well as the OoC geometry favoring RL amplification over BM amplification. The RL and BM displacements sare anti-phasic to each other because the force from the somatic electro-motility acts in opposite directions on the RL and the BM. The asymmetry in the current-displacement curve at negative current stimulation is due to the transients during onset of the stimulation.

length of the cochlea from the stapes), middle (40, 45, and 50%) and the apical (85, 90, and 95%) turn of the guinea pig cochlea. Each FTC has been normalized to its threshold at CF, and the frequency axes have been normalized to the corresponding CF at each location. The blue arrows show the change in the shape of the FTCs in each turn. The red circles are ANF threshold curves from single ANF data obtained in guinea pigs [31]. The model predictions show remarkable agreement with the transition of the shape of the neural tuning curves from base to apex [148] as well as the low and high side slopes at the tip of the FTCs.

4.3.4 Duct taper leads to physiological tuning at apex

To study the effect of duct taper and fluid viscosity on the gain spectrum at the apex, we have simulated the response of the RL at 95% from the stapes in cochleae without taper and/or viscosity. In our simulations without taper, the height of the

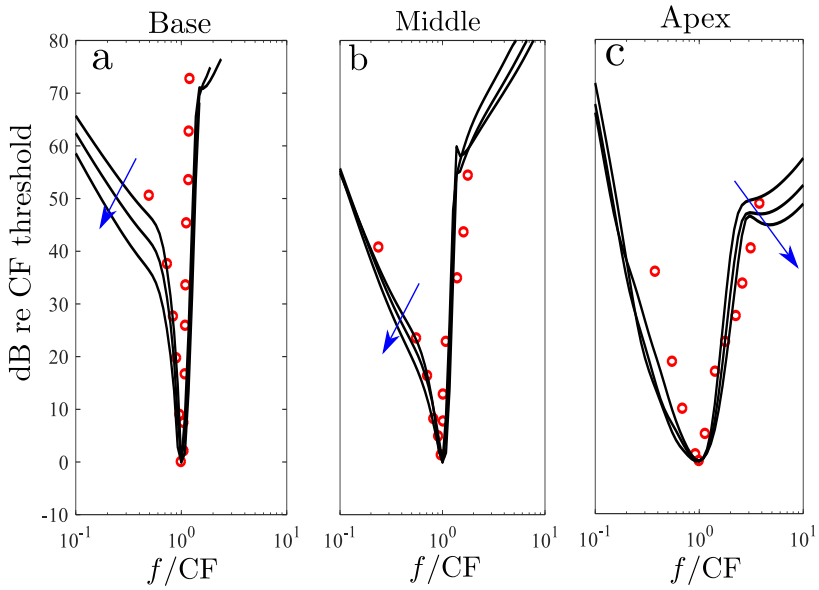

Figure 4.6: Comparison of model prediction of ANF FTC with experiments throughout the cochlea. The ANF FTCs predicted by the model are shown with solid black lines at the (a) basal (20, 25, 30% the length of the cochlea), (b) middle (40, 45, 50% the length of the cochlea), and (c) apical(85, 90, 95% the length of the cochlea) turn of the guinea pig cochlea, normalized to the FTC threshold at the CF. At each turn, the blue arrows show the local base-to-apex transition at each location. All thresholds have been normalized to the threshold at the CF, and the frequency axes has been normalized to the CF at each location. The red circles show measurement of ANF FTCs obtained from measurements in the guinea pig cochlea[31].

straightened cochlea has been selected such that the scalae volume of the straightened cochlea is equal to the scalae volume in the tapered cochlea. The solid line in Fig. 4.7 shows the gain spectra for a tapered cochlea with fluid viscosity (T-V) from Fig 4.4d, but with an extended frequency range going down to 10 Hz. The dashed line shows the gain spectra for a tapered cochlea without fluid viscosity (T-NV), and the dotted line shows the gain spectra for a straight cochlea without fluid viscosity (NT-NV). Both the NT-NV and T-NV models exhibit under-damped system resonances associated with apical reflections and the global motion of the entire organ of Corti [112]. These non-physiological modes of vibration are damped out in the T-V model leading to a displacement spectrum spectrum similar to what is observed in experiments. Further, reduced duct height due to the taper leads to increased fluid mass loading on the

cochlear partition, reducing the CF of the location [143]. Although, both the T-V and the T-NV models predict a downward shift of the CF compared to the NT-NV model due to increased mass loading, only the T-V model displays a reduced CF as well as realistic low frequency tuning.

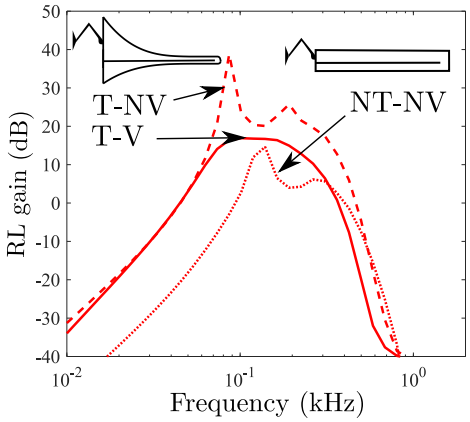

Figure 4.7: The effect of viscosity and fluid mass loading on the RL gain spectrum. The RL gain spectrum at 95% from the stapes with both duct taper and fluid viscosity (T-V, model shown in left inset) is shown with the solid red line. The gain spectrum with duct taper but no fluid viscosity (T-NV) is shown is dashed lines, and the gain spectrum with no duct taper and no fluid viscosity is shown with dotted lines. Both T-NV and NT-NV displays unphysiological peaks due to apical reflections and system resonance. Further, the NT-NV model predicts a higher CF and band-pass characteristic. Only the T-V model correctly predicts the smooth low pass spectrum seen in experiments. All RL gain spectra drop to zero at DC frequency because of the shunting of the fluid pressure across the cochlear partition through the helicotrema.

4.3.5 Variation of macroscopic fluid viscosity and duct height

To study the effect of fluid viscosity throughout the cochlear spiral, we systematically vary the macroscopic fluid viscosity away from the control settings of the model while keeping all other parameters constant to isolate the effect of this parameter on the model response. Fig. 4.8 shows a panoramic view of the BM, RL and threshold ANF response at 20%, 40%, 70% and 95% the length of the cochlea from the stapes as the macroscopic fluid viscosity is varied. The height of the cochlear duct is the same as the control case (see Appendix B for the height profile) for these simulations. At

the base (20%), the effect of macroscopic viscosity on the mechanical tuning is minimal, increasing by 2.5 dB when viscosity is eliminated, and decreasing by 8 dB when viscosity is increased ten fold. The CF is largely unaffected by the change of viscosity (<0.05%). A similar change is observed in the ANF tuning where the threshold is reduced by around 2.5 dB when viscosity is eliminated and is increased by around 8.5 dB when viscosity is increased ten fold. This is expected because the combined boundary layer thickness at CF at this location is around 0.43% of the height of the scala vestibuli, and consequently the macroscopic fluid flow is predominantly inertial.

However the effect of macroscopic viscosity is significant in the middle and the apical turns. At 70% from the stapes, elimination of macroscopic fluid viscosity increases the peak mechanical gain by 4.7 dB and increases the CF by around 8.5%, whereas the increase of macroscopic fluid viscosity decreases the peak mechanical gain by around 12 dB and decreases the CF by 28%. The corresponding changes are also reflected in the ANF tuning curves. The effect of macroscopic fluid viscosity is most pronounced at the apex, where the boundary layer covers 30% of the scala vestibuli. Elimination of macroscopic fluid viscosity led to reflections from the apex as well as increase of mechanical gain by 10 dB and a corresponding increase in CF of around 10%, whereas increasing macroscopic viscosity ten fold led to a significant decrease in mechanical gain by 14.7 dB and a 28% decrease in CF. To summarize, macroscopic fluid viscosity has minimal effect on the mechanical and neural tuning at the base and is not necessary for accurate modeling of cochlear mechanics. However, macroscopic fluid viscosity has a pronounced effect at the apex, and should be included in models of the cochlear apex.

Fig. 4.9 shows the panorama of BM, RL and threshold ANF response at 20%, 40%, 70% and 95% the length of the cochlea from the stapes as the scalae duct height is varied, keeping all other parameters constant. At the base (20%), the effect of varying the height of the scala duct on the mechanical tuning is minimal, increasing by the

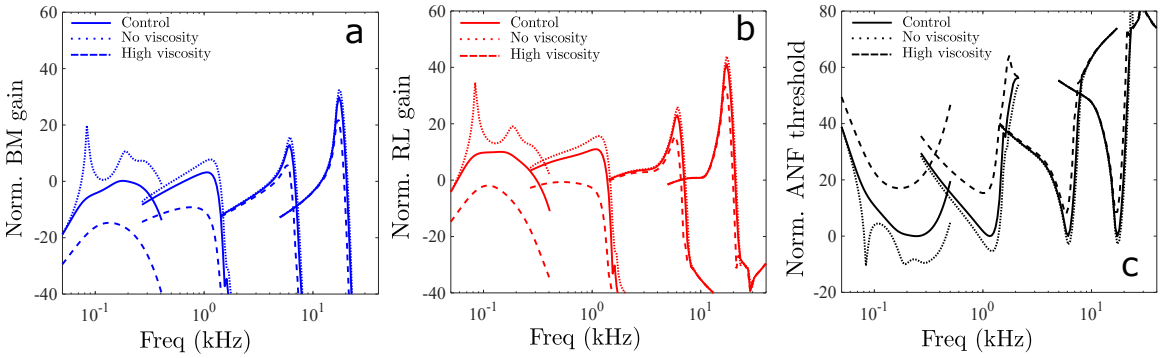

Figure 4.8: The effect of macroscopic fluid viscosity on (a) BM gain, (b) RL gain and (c) threshold ANF tuning at 20%, 40%, 70% and 95% the length of the cochlea from the stapes in the active model. The dynamic viscosity of the macroscopic fluid was varied between 0 cP (No viscosity), 1 cP (Control), and 10 cP (High viscosity). The mechanical responses of the BM and the RL (a,b) have been normalized to the peak passive BM response of the "control" case at each location. The ANF curves (c) have been normalized to the threshold at CF of the "control" case at each location.

peak amplitude by 3 dB when the duct height is doubled, and decreasing it by 4 dB when the duct height is halved, with negligible effect on the CF at the location. A similar change is observed in the ANF tuning where the threshold is reduced by around 3 dB when the duct height is doubled and is increased by around 4 dB when the duct height is halved. Varying duct height in the middle and the apical turns led to significant changes in the mechanical and ANF tuning as well as the CF. At the apex (95%), the BM gain decreased by 17 dB and the CF is reduced by around 40% when duct height is halved. Doubling the duct height increased BM gain by 9 dB and increased the CF by around 34%. From these studies, we can see that the effects of the duct height and viscosity are consistent with theoretical expectations and (more importantly) the correct incorporation of viscosity and duct geometry is critically important for the low frequency, apical region of the cochlea.

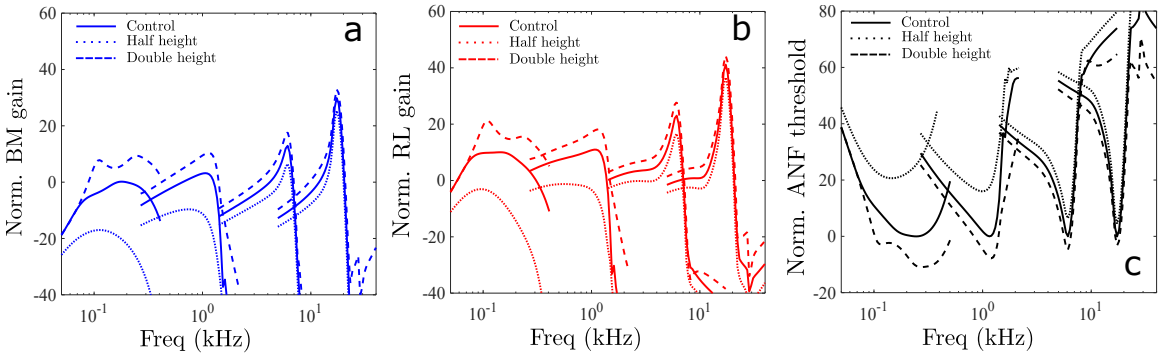

Figure 4.9: The effect of duct height on (a) BM gain, (b) RL gain and (c) threshold ANF tuning at 20%, 40%, 70% and 95% the length of the cochlea from the stapes in the active model. The scalae duct height was varied between the physiological height (H_{SV}, H_{ST}), twice the physiological height, and half the physiological height. The mechanical responses of the BM and the RL (a,b) have been normalized to the peak passive BM response of the "control" case at each location. The ANF curves (c) have been normalized to the threshold at CF of the "control" case at each location.

4.4 Discussion

The effect of macroscopic fluid viscosity on cochlear tuning

Oscillating flow of viscous endolymph and perilymph in the scalae results in the formation of boundary layers (BL) at the walls of the duct as well as in the subtectorial space (STS). Previous studies [111, 38, 129] have analyzed the dissipation due to the BL in the STS, while others [155] have studied the effect of viscosity on the bulk or macroscopic fluid flow in the scalae ducts. In the present study, we concentrated on macroscopic viscous dissipation in the scalae because the accurate modeling of this effect in our model is one of the key factors that led to the transition from basal to apical dynamics (STS damping is used in all simulations). The combined thickness of the BL on the BM and the bony wall is given by $d_{BL} = 2\sqrt{\nu/(\pi f)}$ [71, 112], where ν is the kinematic viscosity of the fluid. In the basal turn of the guinea pig cochlea, d_{BL} is much smaller than the duct height at CF. Consequently, macroscopic fluid viscosity plays a minor role in the mechanical tuning at the base. However, at the apex, the duct height tapers significantly resulting in d_{BL} being comparable to

the duct height for frequencies at and below CF. The increased effect of macroscopic viscosity leads to overdamped motion of the BM and the RL (Fig. 4.7, T-V), resulting in a low quality-factor gain and the reduction of reflections from the apex. Moreover, using the more physiologically realistic duct height in the model induces a greater fluid-loaded mass (as analytically shown in [143]) and lowers the CF compared to a cochlear model with constant cross sectional area, a result we also confirmed using finite element simulations (compare Fig. 4.7, T-NV and NT-NV). The combined effect of macroscopic fluid viscosity and fluid mass loading on the cochlear partition leads to the smooth and broad gain spectrum observed *in vivo* at the apex, and creates a natural transition between the tuning at the basal and the apical turns of the cochlea. While the exact purpose of such a transition in the mammalian cochlea remains unclear, we speculate that the enhanced viscous effects at the apex could have created an evolutionary advantage by supporting higher cochlear gains without compromising stability, resulting in a broader dynamic range of hearing. A systematic study of the effect of macroscopic viscosity and duct height at different locations along the cochlear spiral is included in Appendix B.

The organ of Corti cytoarchitecture significantly impacts the BM gain

In addition to macroscopic fluid viscosity, the cytoarchitecture of the OoC influences the effectiveness of somatic electromechanical forces in modulating the vibrations of the BM and the RL. While orientation of the cytoarchitecture in the longitudinal direction (i.e., base-to-apex direction, see Fig. 4.1) is included in our model and has been studied extensively by others [158], our study primarily focuses on the cellular orientation in the radial plane and its role in cochlear mechanics. In this plane, the RL is pivoted at an angle (denoted as α) with respect to the BM that varies from approximately 5° at the base to 36° at the apex in the guinea pig cochlea. Similarly, the angle between the axes of the OHCs and the DCs (ϕ_{DC} in Fig. 4.1)

varies along the length of the cochlea. The somatic electromechanical force generated by the OHC is transferred to the transverse motion of the BM through the DC, and is proportional to the product of the cosines of the angle between the OHC-DC (ϕ_{DC}) and the DC-BM angle ($\alpha - \phi_{DC}$). Because of this change in orientation, the effective somatic force on the BM decreases by about 20% from base to apex, a factor that can result in a reduction of BM gain up to 20 dB [114]. However, the OHCs are approximately perpendicular to the RL throughout the cochlea, a favorable orientation for actuation via somatic motility. The effect of the modulation of the active process by the geometry can be quantified by the ratio of the maximum gain of the active and the passive model for the RL and the BM, denoted by δ_{RL} and δ_{BM}, respectively. From our model calculations, δ_{RL} varies from 45 dB at the base to 20 dB at the apex (Fig. 4.4), implying high nonlinear gain of the RL throughout the cochlear spiral. Similarly, calculation of δ_{BM} at the base (Fig. 4.2*A*) yields a value of 30 dB, in line with the nonlinear gain seen in experiments at the base of the guinea pig cochlea [26]. However, δ_{BM} was calculated to be around 2 dB at the apex, indicating a near level-independence of the somatic amplification at the apex. This result is consistent with the measured BM gain at the apex which is nearly linear in response to sounds from 40-100 dB SPL [157]. Further, the experimental and theoretical responses to electrical stimulation also demonstrate that somatic motility preferentially moves the RL over the BM at the apex (see Fig. 4.5). Finally, the correlation of nonlinear gain and cochlear geometry is further exemplified by the mouse cochlea where the axes of OHCs are oriented nearly perpendicular to the BM over the entire length of the cochlea [138]. Experimental observations show that, unlike in the guinea pig, the compressive nonlinearity in the BM gain spectrum in the mouse is greater than 20 dB throughout the cochlea [41, 72]. This lends credence to our conclusion that the transition of the geometry of the organ of Corti plays a major role in reducing the effect of nonlinear compression of the BM motion at the apex of the guinea pig

cochlea.

Different factors shape threshold neural response at base and apex

Comparison of Fig. 4.2*A* and Fig. 4.6*A* shows that the shape of the mechanical tuning (roughly the inverse of the gain function at low levels) is similar to that of the threshold neural tuning at the base of the guinea pig cochlea. This is because the high pass filtering associated with the fluid coupling between the radial shear of the TM and the IHC HB [38, 129, 111], as well as the high pass filter associated with the MET channel adaptation [121, 141, 105] have corner frequencies much lower than the CF in the basal turn. Consequently the basal threshold FTCs are primarily shaped by the mechanical dynamics of the organ of Corti [98, 124]. However, in the apical turn, the model predicts that each of the high pass filters associated with the STS fluid-HB coupling and the MET channel adaptation filter contributes a slope of 6 dB per octave for the low frequency limb of the threshold ANF FTC (Fig. 4.6*c*) as discussed in [21, 126]. An additional 6 dB per octave roll-off in the ANF filter is present for frequencies below the cut-in of the high pass filter associated with the shunting of the acoustic pressure at the helicotrema (at around 80 Hz in our model, as seen in Fig. 4.7). The helicotrema cut-in frequency shifts to a higher frequency when the cochlear walls are fenestrated at the apex for for measurement (as in [28, 115]), or in species with larger helicotrema [21].

CHAPTER V

The Effect of Longitudinal Conductance in the Cochlear Scalae

5.1 Introduction

Otoacoustic emissions (OAEs) have been successfully utilized as a non-invasive diagnostic tool for clinical detection of hearing pathologies for over a decade. However, there are still unanswered questions about how these emissions are generated and emitted from the inner ear. It is well accepted that the otoacoustic emissions are generated by active mechanisms in the cochlea, and consequently strongly correlated with the physiological health of the cochlea. Invasive as well as non-invasive experimental studies, backed by theoretical models have successfully explained many of the similarities and differences in the spectral and temporal response to pure tones and tone complexes. The current theoretical understanding of cochlear emission is founded on the classification by Shera and Guinan as summarized in Fig. 5.1. Spontaneous otoacoustic emissions (SOAE) are emissions exhibited by the cochlea without any external stimuli and are postulated to arise due to standing wave dynamics within the cochlea. Stimulation frequency otoacoustic emissions (SFOAE) are emissions that are generated by the cochlea when stimulated by an external stimulus and are at the same frequency as the stimululation tone. On the other hand, distortion product

otoacoustic emissions (DPOAE) are cochlear emissions due to two or more tones (at frequencies $f_1, f_2, \ldots, f_n$, where $f_1 < f_2 < \ldots < f_n$), and are at harmonic combination of the stimulation frequencies. Both SFOAEs and DPOAEs are evoked by external stimuli and are consequently classified as evoked emissions. However, SFOAEs have been hypothesized to primarily arise from cochlear activity coupled with coherent linear reflections from cochlear irregularities, whereas DPOAEs are postulated to arise from nonlinear sources in the cochlea, mostly from the MET channels in the hair bundles and the electromotility of the basolateral membrane of the outer hair cells.

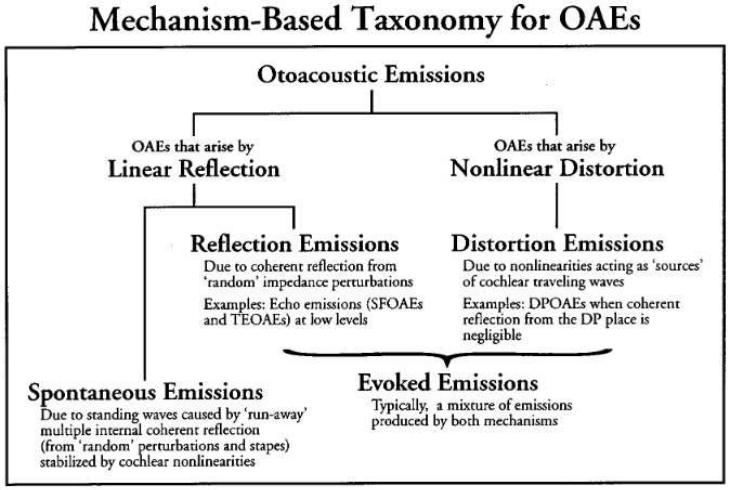

Figure 5.1: Classification of various types of cochlear emissions based on generation and propagation mechanism, from Shera and Guinan [135]

In this taxonomic scheme, the paths of reverse propagation of the SFOAE and the DPOAE are shown in Fig. 5.2. The SFOAE is generated by partial reflection of the traveling from all regions of the BM, but is most prominent close to the peak of the traveling wave. The reflected wave travels back to the stapes as a backward propagating wave and is emitted our through the middle ear. Part of the wave impinging on the stapes footplate is reflected back into the cochlea due to the middle ear impedance mismatch. When a healthy cochlea is stimulated by two tones (at frequencies f_1 and f_2, $f_1 < f_2$), the distortion product (DP) is generated close to the best place of the higher frequency (f_2) tone, and is partially reflected to the

stapes, where part of the wave is transmitted out of the ear as DPOAE, and the rest undergoes reflections and is launched back as a forward propagating wave. A part of the generated DP travels to its own best place along the cochlear spiral and is linearly reflected back to the stapes, similar to the SFOAE. In either case, this model predicts that otoacoustic emissions travel inside the cochlea as a fluid-structure coupled wave on the cochlear partition. This is in agreement with intracochlear pressure measurements [29] that have found that the distortion frequency is localized to the fluid close to the cochlear partition and is rapidly attenuated away from it.

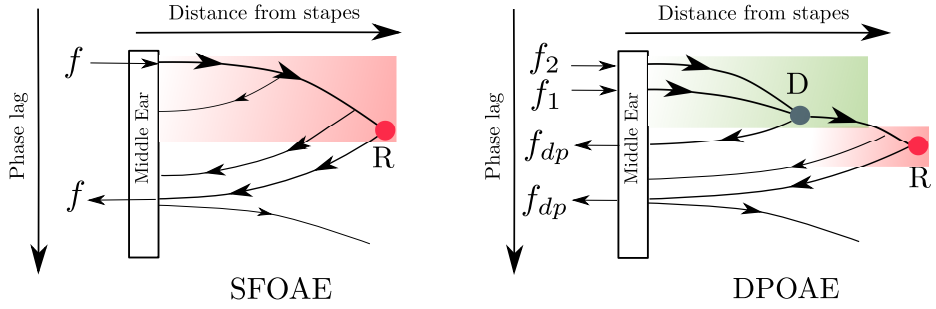

Figure 5.2: The path of the stimulus, reflection and distortion waves inside the cochlea in SFOAEs and DPOAEs, adapted from Shera and Guinan [135]. In SFOAEs, the stimulus tone undergoes reflection from cochlear irregularities throughout the cochlea, but mostly from the peak of the traveling wave (labeled as R and shown with red circle). The amplitude of the traveling wave is shown with red colored gradation. In DPOAEs, the primary tones, f_1 and f_2 generate harmonics close to the f_2 best place (marked with D). The amplitude of the f_1 primary is shown with the green color gradation. Part of the distortion product wave travels back to the stapes, and part of the wave travels to its own best place (corresponding to f_{dp}) where it undergoes coherent reflection and travels back to the stapes. The red color gradation shows the amplitude of the distortion product wave.

However, experiments by He et al. [50] have shown that the BM vibration temporally lags the stapes vibration, implicating that the emissions generated inside the cochlea travel out of the cochlea via fast compressional waves, and part of the wave is reflected back at the stapes. To further control for the uncertainty in the region where the DP is generated Ren et al. [118] have utilized intracochlear electrical stimulations to evoke otoacoustic emissions (EEOAE) within the cochlea and provide a controlled method to excite the cochlear partition and study the propagation of these emissions

out of the cochlea. In their experiment they observed the DP on the cochlear partition at two locations both basal to the stimulation location, corresponding to 12.4 kHz and 15 kHz. Their results showed that the displacement of the cochlear partition at the 15 kHz region led the displacement at the 12.4 kHz region, indicating that the DP travels from the location where it is generated to the stapes and subsequently travels from the base to the apex (as schematically shown in Fig. 5.3). This ambiguity between the delay derived from DPAOE and intracochlear measurements, and those from the EEOAE measurements are confounding and prevents a complete understanding of cochlear nonlinearities required to develop non invasive measures of cochlear health. In this chapter, we have modeled the electrical excitation of the cochlea using varying stimulus protocols and analyzed the effect of the longitudinal spread of electric current in the scalae to better understand the generation and propagation of EEOAEs in the cochlea.

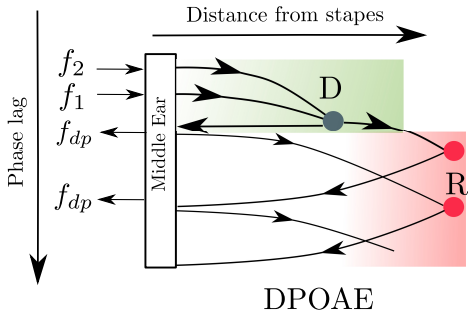

Figure 5.3: The path of the stimulus, reflection and distortion waves inside the cochlea according to the fast reverse wave hypothesis.

5.2 Methods

The cochlea has been modeled as a prismatic box with the cochlear partition separating the scala vestibuli fluid duct from the scala tympani duct, as described in Chapter II. The organ of Corti has been modeled through a Lagrangian framework by including the kinetics and the kinematics of the three rows of outer hair cells (OHCs)

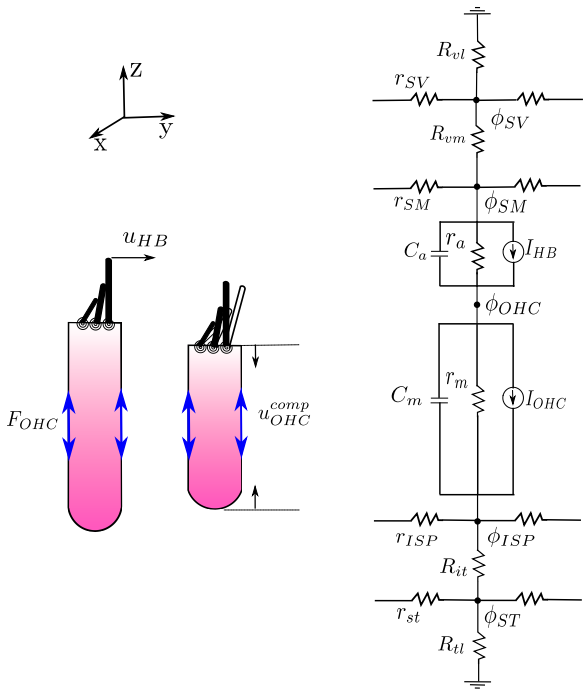

Figure 5.4: The model of the outer hair cell and the electrical circuit. The resistances r_{SV}, r_{SM}, r_{ISP} and r_{ST} correspond to longitudinal coupling in the scalae fluid. The electrical potentials in the scala vestibuli (ϕ_{SV}), scala media (ϕ_{SM}), interstitial space (ϕ_{ISP}) and scala tympani (ϕ_{ST}) at each cross-section are coupled to its neighbors through the longitudinal cables. The apical conductance of the outer hair cell is quantified thorough the resistance r_a and capacitance C_a. The MET channels are modeled as a current source I_{HB} whose strength is modulated by the excitation of the HBs. The basolateral resistance and conductance are given by r_m and C_m respectively, and the piezo action of *prestin* is modeled as a current source in the electrical domain as I_{OHC}.

and the hair bundles (HBs), the reticular lamina (RL), the tectorial membrane (TM) and the pillar cells (PCs) as in [114]. The basilar membrane (BM) has been modeled as a longitudinally coupled orthotropic plate and the TM has been modeled as a longitudinally coupled shear beam, as in [87]. The somatic electro-motile force from each OHC (F_{OHC}) have been modeled through piezoelectric constitutive equations as in Eq. 2.15 and the MET current (I_{HB}) is modeled with the two state Boltzmann distribution as in Eq. 2.13.

Previous modeling studies by Li and Grosh [74, 75] have shown that internal point excitation of the BM in a transversely symmetric cochlea results primarily a

backward propagating wave in the cochlea, and there is minimal contribution from the compression fast wave to the cochlear emission. However, the cochlea is not transversely symmetric and there are significant differences in the scalae volume in the cochlea. Further, the stiffness of the round window is much lower than that of the stapes. This transverse asymmetry in the cochlea can excite a fast wave within the cochlear ducts and couple the cochlear partition with the middle ear, providing a fast acoustic path. However, in this chapter, we are primarily concerned with the effect of the spread of electric current in the scalae. To eliminate the fast waves generated due to the transverse asymmetry of the cochlea, we have artificially imposed an equality of the scalae volumes, and round window and stapes stiffness.

To model the longitudinal spread of current in the scala tympani, we have modified Eq. 2.8 to include the longitudinal cables for the spread of current in the scala tympani. The modified electrical circuit is shown in Fig. 5.4. The longitudinal cables r_{SV}, r_{SM}, r_{ISP} and r_{ST} denoting the cable resistance in the scala vestibuli (SV), scala media (SM), interstitial space (ISP) and scala tympani (ST). Note that the longitudinal conductance in the ISP is much lower than the SV, SM and ST. The modified set of cable equations can be written as

$$
\begin{aligned}
\frac{1}{r_{SV}}\frac{\partial^2\phi_{SV}}{\partial x^2} - \left(\frac{1}{R_{vl}} + \frac{1}{R_{vm}}\right)\phi_{SV} + \frac{1}{R_{sm}}\phi_{SM} =, 0 \\
\frac{1}{r_{sm}}\frac{\partial^2\phi_{SM}}{\partial x^2} + \frac{1}{R_{vm}}\Big(\phi_{SV} - \phi_{SM}\Big) - 3Y_a\Big(\phi_{SM} - \phi_{OHC}\Big) - I_{HB} = 0, \\
3Y_a\Big(\phi_{SM} - \phi_{OHC}\Big) - 3Y_m\Big(\phi_{OHC} - \phi_{ISP}\Big) + I_{HB} - I_{OHC} = 0, \\
\frac{1}{r_{ISP}}\frac{\partial^2\phi_{ISP}}{\partial x^2} + 3Y_m(\phi_{OHC} - \phi_{ISP}) - \frac{1}{R_{it}}\Big(\phi_{ISP} - \phi_{ST}\Big) + I_{OHC} = 0, \\
\frac{1}{r_{ST}}\frac{\partial^2\phi_{ST}}{\partial x^2} + \frac{1}{R_{it}}\Big(\phi_{ISP} - \phi_{ST}\Big) - \frac{1}{R_{tl}}\phi_{ST} = 0
\end{aligned}
\tag{5.1}
$$

5.3 Results

To study the effect of the longitudinal propagation of electrical current in the scalae fluid, we simulated the response of the cochlea under various excitation protocols for three different models. The first model, subsequently referred to as Model 1, ignores all longitudinal cables in the scalae eliminating longitudinal spread of current in the cochlear fluid. The second model, referred to as Model 2, restores the longitudinal electrical cables in the SV, SM and ISP, but not in the ST. Finally Model 3 refers to the model with all longitudinal electrical cables in the scalae.

5.3.1 Acoustic response

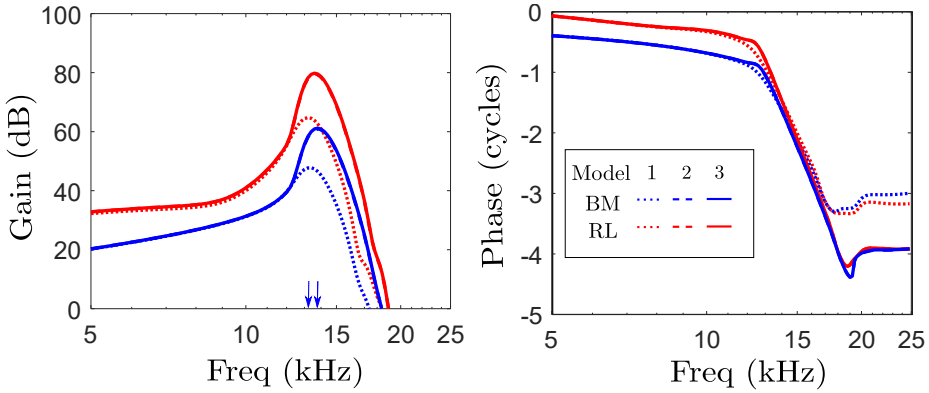

Figure 5.5: The displacement spectra of the BM and the RL in the three models under acoustical excitation at the stapes.

Fig. 5.5 shows the gain and phase of the BM and the RL for the three models when the stapes is excited by a pure tone acoustic stimulus. The dotted lines show the gain and phase spectra for the model with no longitudinal cables (Model 1), the solid lines shows the spectra for the model with the SV, SM and ISP longitudinal cables included (Model 2), and the solid lines show the spectra for the model with all cables included (Model 3). The spectra for the RL displacement is shown with red lines and the spectra for the BM displacement is shown with blue lines. The BM and RL gain spectra are identical for Model 2 and Model 3 showing that the inclusion

of ST longitudinal cables do not affect the mechanical response of the cochlea to acoustic stimuli. However, elimination of the longitudinal cables (Model 1) leads to more than 10 dB decrease in the gain and is in line with what has been reported in the literature [91]. The phase spectra remained largely unchanged in all three cases.

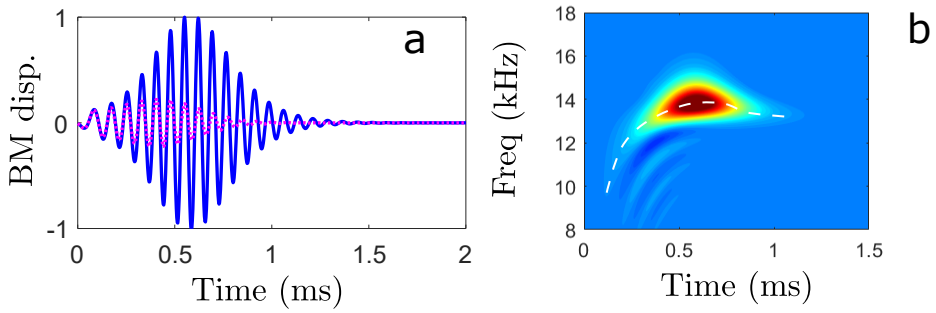

Figure 5.6: The temporal pattern of the BM vibration. (a) Time history of BM vibration at 4 mm from the stapes calculated from Model 1 (dotted) and Model 3 (solid). The displacements are normalized to the peak displacement of the response from Model 3. The peak amplitude as well as the group delay of the wave packet is reduced in Model 1, making it more 'passive'. This is reflected in the lower amplitude and shallower phase spectra of Model 1 in Fig. 5.5. (b) The Wigner transform of the BM displacement in Model 3 at the same location. The Hilbert transform of (a) is overlaid to emphasize the glide in the frequency spectrum. Model 1 shows a similar glide (not shown) but the CF and the group delay at CF are lower than (b).

To study the temporal dynamics of the BM in these three models, we converted the BM response to the time domain using the inverse Fourier transform. Fig. 5.6(a) shows the model calculations of BM displacement due to a click at the stapes. The calculations from model 1 are shown with purple dotted lines and those from model 3 are shown with solid blue line. The BM response from Model 2 is not shown because they were identical to those obtained from Model 3 (as is evident from Fig. 5.5).Both responses have been normalized to the peak response from Model 3. The wave envelope calculated from Model 3 has a higher amplitude as well as a longer forward group delay (t_g) than the wave packet from model 1. Further, the wave envelope from both models have very similar phase delays, leading to similar zero-crossings in both models. This is similar to the near-invariance of the zero-crossing times with stimulus

levels observed in experimental observations [133] and included in theoretical models, and implies an effective loss of somatic electromotility in model 1 as compared to model 3. To further confirm that the presence of the ST cables do not results in non-physiological responses, we calculated the temporal-spectral response of the BM displacement from model 3. Fig. 5.6(b) shows the Wigner transform of the BM displacement at 4 mm from the stapes due to the click stimulus. The white dashed line is then smoothened Hilbert transform of Fig. 5.6(a), and is overlaid to emphasize the increase in the instantaneous frequency of the BM with time, a phenomenon known as the frequency glide [25]. This is a direct consequence of the cochlear dispersion, resulting in lower frequencies reaching the location with shorter group delays and frequencies close to the CF reaching the location with a greater group delay, and can be observed in the BM as well as the auditory nerve response [25, 10].

5.3.2 Bipolar electrical stimulation

To study the electrical response in the three models, we simulated the excitation of the cochlea to bipolar electrical stimulation in the scalae. First, we study the response of the cochlea when the electrodes are placed in the SV and the ST at the same longitudinal location along the cochlear spiral. Fig. 5.7 shows the BM displacement and stapes velocity spectrum when the bipolar electrodes are placed at 4 mm from the stapes in the SV and the ST. All models show narrowband BM excitation close to the CF of the excitation location. Without any longitudinal cable (model 1), the BM displacement spectrum shows a notch close to the CF, which gives rise to beating in the time domain (see Fig. 5.7(a)). This is due to the interference between the instantaneous BM motion caused by the electrical stimulation and the delayed slow (fluid-structure coupled) wave reflected back from the stapes with a time delay of $2t_g$. This notch was not observed in the other two models. Model 3 showed a pronounced notch as well as phase inversion close to the resonance frequency of the

uncoupled TM radial motion at this location.

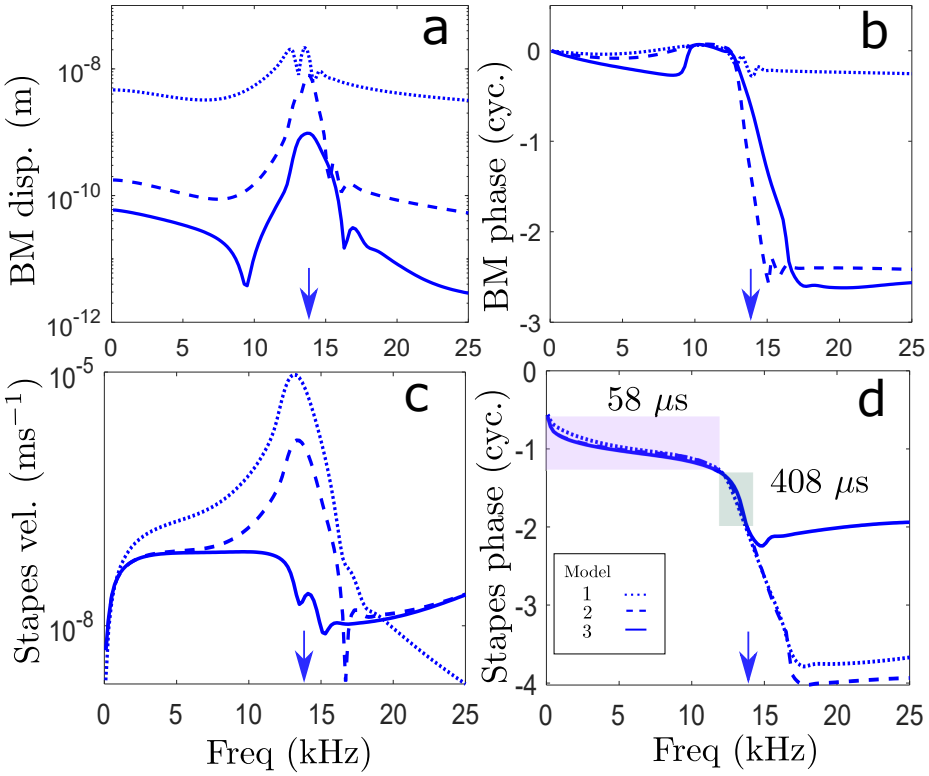

Figure 5.7: The (a,b) displacement spectra of the BM and the (c,d) velocity spectra of the stapes in the three models under bipolar electrical stimulation at 4 mm from the stapes. The purple shaded box shows the "fast" part of the response with an average group delay of 58 μs and the grey shaded box shows the "slow" part of the response with an average group delay of 408 μs.

To avoid complexities associated with the middle ear dynamics, acoustics of the ear canal and the placement of the probe [80], we used the stapes velocity as a surrogate for the EEOAE from the ear canal. Fig. 5.7(c,d) shows the velocity magnitude and phase spectrum of the stapes motion. While the stapes motion in model 1 and mode 2 is narrowband, the stapes motion calculated from model 3 is broadband with a lower cutoff of around 1.5 kHz and and upper cutoff at the CF of the excitation location. The rise in the magnitude spectrum beyond 20 kHz is due to the half wavelength resonance of the scalae in the model (at around 40 kHz). In model 3, most of the energy reaches the stapes with a group delay of around 58 μs (the average slope in the purple shaded region), whereas in models 1 and 2, most of the energy reaches the

stapes with a time delay of around t_g. Note that 58 μs is much shorter than t_g but is much longer than the time for an acoustic pressure wave to travel 4mm in water (2.6 μs). This is further shown with the temporal evolution of the BM displacement and stapes displacement in Fig. 5.8. In both models 1 and 2, the dominant wavelet is tuned at the CF of the stimulation location and it travels to the stapes as a slow wave and is reflected back to the generation location at time $2t_g$. However, in model 3, the stapes is entirely excited by a broadband excitation which in turn generates a broadband traveling wave from the base to the apex which reaches the stimulation location at time t_g. The broadband stapes excitation can also be seen in the initial displacement of the stapes in model 2, but the BM displacement is dominated by the narrowband slow traveling wave.

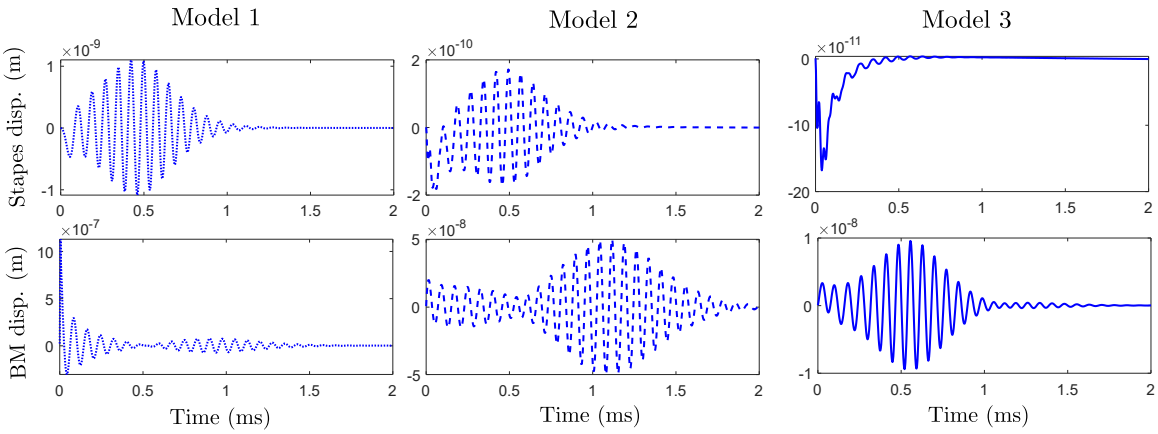

Figure 5.8: The displacement spectra of the BM and the velocity of the stapes in the three models under bipolar SV-ST electrical stimulation at 4 mm from the stapes.

5.3.3 Effect of different stimulation protocols

To study how the placement of the electrodes in the scalae affects the response of the stapes and the BM, we simulated the model with all cables (model 3) with three types of bipolar electrical excitations. First, the two electrodes are located in the SV and the ST (SV-ST stimulation), similar to Figs. 5.7 and 5.8. Second, we moved one of the electrodes in the SV closer to the BM, into the SM (SM-ST stimulation). Third,

we moved the ST electrode closer to the BM, into the interstitial space to simulate very localized electrical excitation (SM-ISP stimulation) of the cochlear partition. Fig 5.9(a,b) shows the temporal response of the stapes and the BM (at the excitation location) to the three protocols. During both SV-ST and SM-ST stimulations, the predominant motion displayed by the stapes is at around 58 μs, indicating excitation by a broadband fast-wave, which is subsequently reflected back to the excitation location at time t_g. This is reflected in the frequency spectum of the stapes velocity response, as shown in Fig. 5.9(c,d). The SM-ST stapes motion also displayed a low amplitude wave tuned to the CF of the excitation region that arrives at the stapes at time t_g, and is subsequently reflected back to the excitation location at time $2t_g$. Although the timing of the primary excitations in the SV-ST and the SM-ST are similar, the SM-ST excitation produces larger motions than the SV-ST excitation (Fig. 5.9(c)) across all frequencies. When the electrodes are placed in the SM and ISP, the stapes response displays an initial peak at 58 μs succeeded by a wavelet tuned to the CF of the excitation location at time t_g. This wave is reflected back to the excitation location at time $2t_g$ as shown in Fig. 5.9(b). The delayed response is reflected in the large magnitude of the stapes velocity at the CF in Fig. 5.9(c) as well as the time delay associated with it (Fig. 5.9(d)).

5.4 Discussion

The space constant (δ) of the cochlear microphonic is estimated to be around 1 mm in the first turn of the guinea pig [92, 144]. In fact the spatial resolution of cochlear implants is often limited by the spread of potentials in the scalae which hinders localized neural stimulation. Calculation of the space constant of the cochlear microphonic from the three models (Fig. 5.10) yield a space constant of around 800 μm for model 3. Deletion of the longitudinal cables in the ST (model 2) drastically reduces the space constant to around 32.9 μm close to the excitation site and around 150 μm

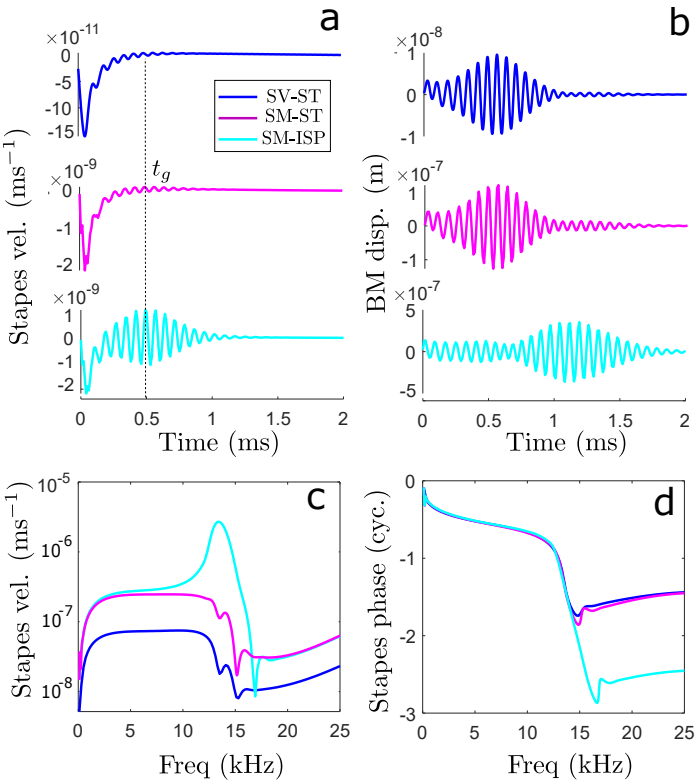

Figure 5.9: The temporal evolution of the (a) velocity of the stapes and (b) the displacement of the BM in model 3 under SV-ST (blue), SM-ST (purple) and SM-ISP (cyan) bipolar electrical stimulation at 4 mm from the stapes. The (c) magnitude and (d) phase of the stapes velocity spectrum.

away from it, much less than what is observed experimentally. A similar pattern was obtained for the ϕ_{ST} spread in model 1 (not shown). The longitudinal spread of electrical current in the cochlea in model 3 leads to activation of the cochlear amplifier over a larger region leading to a higher BM gain when the cochlea is stimulated acoustically (Fig. 5.5). Further, there is negligible phase accumulation during the current spread in model 3, leading to the coherent activation of the cochlear partition over the region, indicating that the current spread is through the longitudinal cables in the ST. Using a model similar to model 1, Meaud et al. [91] have shown that the effective cochlear electromotility is reduced when the longitudinal cables are severed, and have compensated for the loss of gain by increasing the MET sensitivity (and effectively the OHC electromotile force) in the model. However, in this study, we

show that although the elimination of cables do not drastically change the acoustic response (other than effectively reducing the somatic electromotile force, see Fig. 5.6), the electrical response of the cochlea is changed considerably and these effects are not entirely captured increasing the strength of somatic motility in the model (see Fig. 5.7).

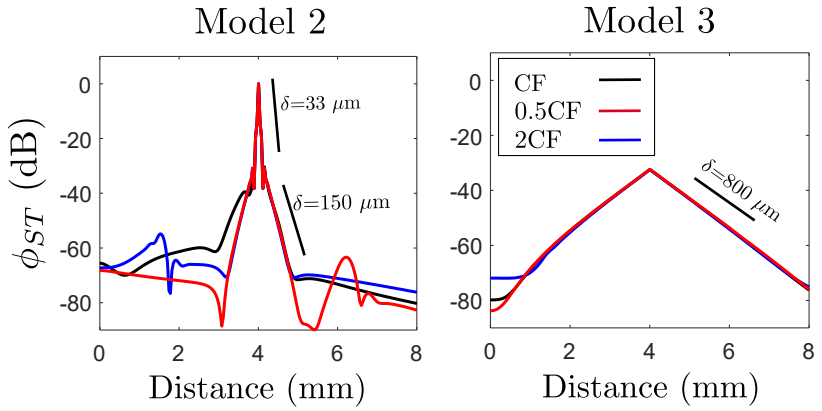

Figure 5.10: The spatial spread of the cochlear microphonic (ϕ_{ST}) in the ST during SV-ST bipolar stimulation is much lower when longitudinal ST cables are severed. The black lines show the amplitude of ϕ_{ST} when excited at CF. The blue lines and red lines show the spatial spread when the excitation is at an octave above CF and an octave below CF respectively. Calculations using model 3 yield a space constant of around 800 μm. Removal of the longitudinal cables in the ST (model 2) leads to more localized increase of the microphonic and a reduction of the space constant to around 33 μm (dashed lines). The spatial spread in model 1 was found to be similar to model 2 and is not included. Note that the spread in the longitudinal cables The magnitudes have been normalized to the peak value of the microphonic without ST cables.

During SV-ST and SM-ST bipolar stimulation, the large spread of the electrical current in the scalae leads to the engagement of somatic motility over several millimeters by the modulating the extracellular potential of the outer hair cells. This leads to a delocalized coherent broadband excitation of the cochlear partition over many millimeters which couples directly with the stapes through the lymphatic fluid. The motion of the stapes, in turn launches a broadband slow propagating wave on the cochlear partition that travels from the base to the apex exciting the BM at each location. Consequently, the delay at the BM is equal to the forward delay t_g, as shown

in Fig. 5.8(c). This is in agreement with experiments in the guinea pig [48] where bipolar excitation in the SV and the ST resulted in a BM response at time t_g. The model predictions are compared with the measurements from [48] in Fig. 5.11. The frequency is normalized to the characteristic frequency and the time in Fig. 5.11(c) is normalized to t_g in each case (t_g in the model is around 0.5 ms and for the experiment is around 0.41 ms). The MET sensitivity was set to 90% of the peak value and a 5% roughness was added to the BM stiffness. Note that the roughness profile can be added to the MET sensitivity instead (as in [76]) but the choice of adding the roughness profile to the BM stiffness ensured cochlear roughness even at high stimulus levels where the MET sensitivity is close to zero in the linearized model. The model predictions for the acoustic response are in good agreement with the experiments except at $t = 0$. The model does not predict the initial high BM response during SV-ST stimulation that is seen in the experiments. This is reflected in the frequency domain as the splitting of the peaks near CF (Fig. 5.11(c)), which is not seen in the model. This could be due to overestimation of the longitudinal cable conductance in the model, or the ST electrode being placed closer to the BM in the experiments than is assumed in the model. However, the temporal delay of the wave packet in the model matches well with the experiments, with the wave packet arriving at the excitation location at the forward acoustic delay t_g. Further, our model also predicts the half cycle phase shift half octave below the CF, which is not predicted by model 1 or model 2. This could have implications for the phase of the otoacoustic emissions generated during intracochlear electrical stimulation, and could be correlated with the half cycle phase shift seen in the DPOAE spectrum [82].

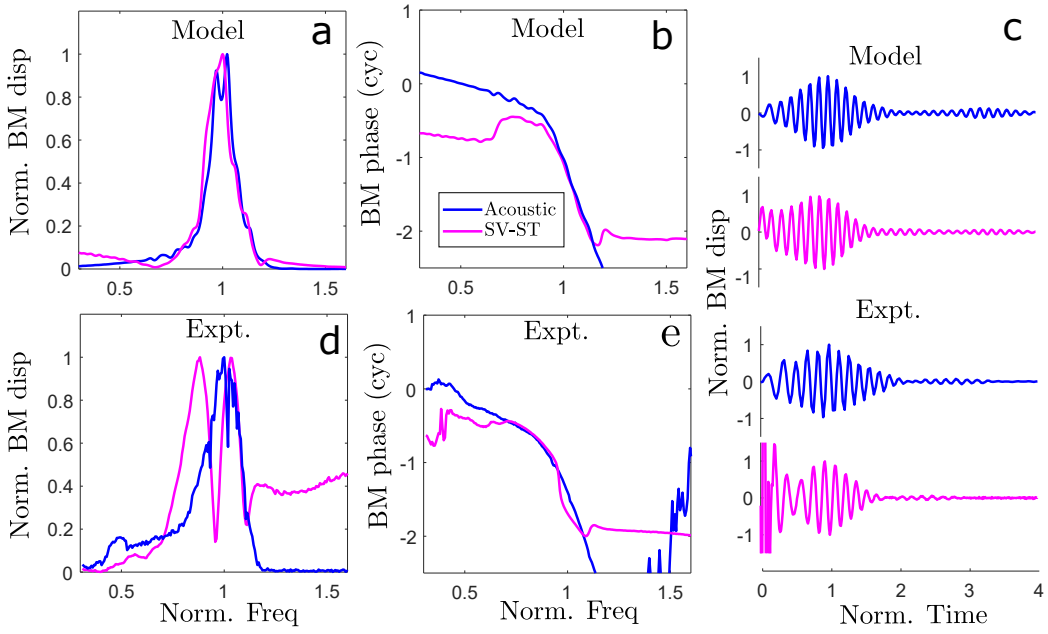

Figure 5.11: The comparison of acoustic and SV-ST bipolar response in the model with experimental measurements in the guinea pig [48]. In the model, the MET sensitivity is reduced to 90% its peak value to effectively account for surgical injuries, and a 5% roughness in the BM stiffness profile is added to generate reflections within the cochlea. (a,b) shows the BM amplitude and phase spectrum obtained from model 3 to SV-ST bipolar excitation (purple) and acoustic excitation at the stapes (blue). (d,e) shows the experimental measurements in the guinea pig cochlea [48]. (c) shows the impulse response due to SV-ST bipolar excitation and acoustic click at the stapes, obtained from model calculations and from the experimental data. The model results are in good agreement with the experimental measurements except at $t = 0$ where the model results do not show the initial transient. Both the experimental measurements and model results show that the wavelet reaches the excitation location at time t_g. The frequencies are normalized to the CF and the maximum amplitudes are normalized to 1 in the spectral data. The time axis is normalized to t_g and the maximum wavelet amplitude is normalized to 1 in (c).

To further test our model, we compared the model response to SM-ST bipolar excitation to the experimental measurement of the cochlear response to the same protocol in the mouse [118]. The BM and RL spectrum at the excitation location is shown in Fig. 5.12(a,b). The model calculations for the RL and BM magnitude and the RL phase agrees well with the experimental measurements. Fig. 5.12(c) shows the time trace of the BM and RL motion in the model and the experiment. Both the model and experiment show an initial high RL response that is absent in the BM response. Further, the model calculations of the wave delay at the BM (at time t_g) agrees with what is seen in the experiments, supporting the model prediction that the electrical spread in the ST leads to a delocalized excitation of the BM, as shown in Fig. 5.9.

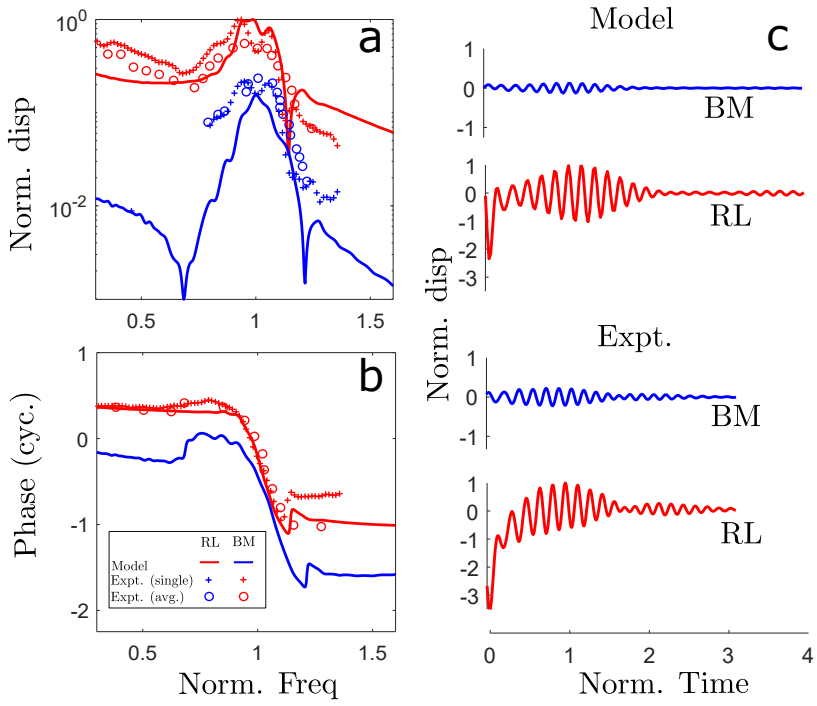

Figure 5.12: The comparison of SM-ST bipolar response in the model with experimental measurements in the mouse. In the model, the MET sensitivity is reduced to 90% its peak value to effectively account for surgical injuries, and a 5% roughness in the BM stiffness profile is added to generate reflections within the cochlea. The experimental data is adapted from [118]. (a) The BM and RL spectrum obtained from model calculations. The data from a single animal is shown with crosses and the averaged data is shown with circles. The BM phase uncertainty was high in the experiment and bore no relationship with the RL phase (personal communication) and hence is not included in (b). Also, the experimental BM magnitude data below 30 kHz is close to the noise floor and is not included. (c) The normalized time response of the BM and the RL displacement obtained from model calculations and from experimental measurements. The time axis is normalized to t_g for both model results and the experimental data.

To study the effect of the decoupling of the hair bundles from the TM, as in Tecta$^{G/G}$ mice, we simulated the cochlear response to SM-ST bipolar excitation in both model 2 and model 3 with the hair bundles detached from the TM radial motion. Fig. 5.13(a,b) shows the spectral response obtained from the models (compare with Fig. 5.7). The tuning is completely abolished and the RL spectrum is low-pass in both models. These model results are in line with measurements of BM and RL displacement during SM-ST stimulation in Tecta$^{G/G}$ mice ([118], Fig. 3). In the time domain, the RL and the BM show an instantaneous response but no delayed wave response at time t_g. Moreover, the response of the stapes at time t_g in model 2 is eliminated but the fast wave response at around 58 μs in model 3 is still retained (not shown) demonstrating that, unlike the slow response, the fast stapes response does not depend on the tuning of the cochlea. The lack of the delayed wave on the BM and the RL can be explained by the lack of tuned amplification in the forward propagating wave when the TM is decoupled from the hair bundles [30].

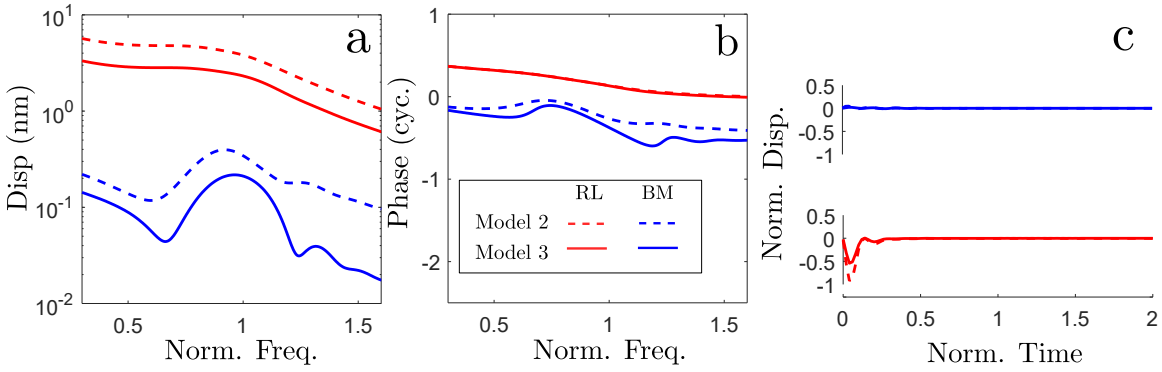

Figure 5.13: The frequency and time response of the BM and the RL when the hair bundles are decoupled from the TM as in Tecta$^{G/G}$ mutation. The frequency axis is normalized to the CF and the time axis is normalized to t_g.

To summarize, when the longitudinal cables are severed (model 1), the fast broadband response of the stapes is abolished and the stapes only receives the slow wave packet tuned to the CF of the excitation region at time t_g (Fig. 5.8(a)) which is reflected back to its generation site at time $2t_g$. This response is markedly similar to

the response of the BM to bipolar internal force excitation on the BM as discussed in [75]. On partially restoring the cables (model 2), the fast response of the stapes is recovered and the dominant excitation of the BM occus at t_g, although the slow CF-tuned wavelet still exists and can be seen at time $2t_g$ (Fig. 5.8(b)). Note that the high frequency response at the stapes in all three models is limited by the CF of the location of the stimulation (Fig. 5.9). At frequencies higher than the CF of the stimulation location, the reverse traveling wave is shunted at its own best place (at a location between the stapes and the stimulation location). Note that if the reverse wave were a pure fluid compression wave, this low-pass filtering at the CF of the stimulation location would not exist because the frequencies higher than the CF would not be filtered by the response of the cochlear partition between the stimulation site and the stapes. Hence, we conclude that the reverse wave is not an acoustic wave that travels through the fluid as a pure compression wave but exists as a fast electric-fluid-structure coupled wave that travels with a group delay of around 50 μs as shown in Fig. 5.7.

We have also shown that the location of the electrodes in the endolymph or perilymph can significantly affect the response of the stapes and the BM. Moving the electrodes closer to the BM in the perilymph leads to a pronounced increase in the amplitude of the slow CF-tuned wave, and the BM is predominantly excited by the slow traveling wave after it is reflected back from the stapes at time $2t_g$ (Fig. 5.9). On the other hand, the cochlear response is comparatively less sensitive to the location of the electrode in the SV or the SM (other than the increase in the amplitude across the spectrum for SM), and the BM is primarily excited by the broadband wave generated by the fast motion of the stapes at time t_g.

Intracochlear electrical excitation is not a physiological form of stimuli *in vivo*. However, in the laboratory, they provide insights into how waves generated within the cochlea propagate out of the inner ear, and help with the understanding of DPOAEs

in a controlled setting. Canonically, these waves are thought to propagate either as a fast acoustic wave or as a slow fluid–structure coupled wave. In the current study, we identify a third pathway and show that electrical excitation can lead to delocalized excitation of the cochlear partition over several millimeters, and produce EEOAE delays that are could be different from that from DPOAEs. Although no conclusions about DPOAE delay can be drawn from this study, the results presented here show that EEOAE delays can be dramatically affected by the position of the electrode within the cochlea, and care must be taken while correlating EEOAE delays with DPOAE delays.

CHAPTER VI

Cochlea-inspired Linear Nonreciprocal Metamaterial

6.1 Introduction

Reciprocity in wave-bearing acoustic media is remarkably robust, especially in linear systems, maintained in viscoelastic solids [40], fluid-structure systems [101], and structural-piezoelectric-electrical coupled systems [6]. Further, as is well-established, anisotropy and inhomogeneity, while generating interesting wave propagation phenomenon, do not engender linear nonreciprocity [40]. Acoustic reciprocity, formally introduced by Helmholtz in 1860 (as discussed in [146]) and later generalized by Lyamshev [83] to include fluid-structure interaction and multiple scatters, dictates that the response to a disturbance is invariant upon interchange of the source and receiver. Fluid and solid acoustic media that break reciprocity over broad frequency ranges would enable new and unexplored forms of control over vibrational and acoustic signals, with enormous implications for spectral filtering and duplexing in the communications industry [106], and noise control [84], [20]. Efforts aimed at achieving nonreciprocity in both linear and nonlinear electromagnetic systems have been particularly successful primarily because of the effectiveness of a biasing magnetic field in devices such as the Faraday isolator [140]. These successes have spurred re-

search in analogous acoustic systems where instead of an external magnetic field, introduction of mean flow in the acoustic medium [10] has been used to achieve a high level, narrowband nonreciprocity. Similarly, biasing in a solid using a DC electric field can result in asymmetric damping and nonreciprocal wave propagation in piezoelectric semiconductors [55], [46] as well as in a two-dimensional electron gas coupled to piezoelectric semiconductors [132]. In magnetoelastic and polar media, a DC magnetic field can lead to nonreciprocal effects, although these nonreciprocal effects are often relatively weak (as discussed in [40]). Other approaches to acoustic nonreciprocity rely on breaking the spatial or temporal symmetry in the governing equations by introducing nonlinear interactions [37], [107] or spatiotemporal modulation of the properties of the medium [139], [156]. Theoretical analysis has shown that spatiotemporal modulation of strongly magnetoelastic materials, like Terfenol, and piezoelectric materials, like PZT, can lead to impressive nonreciprocity, as shown in [5]. Both nonlinearity and spatiotemporal modulation introduce secondary tones that require later demodulation or signal processing to prevent signal corruption. To circumvent the disadvantages associated with background bias or spatiotemporal parametric modulation, other studies have utilized collocated sensor-actuator pairs to modulate the wave propagation in the medium in a linear fashion [15, 161, 12]. To our knowledge, we are the first to exploit a system with distributed control using non-collocated sensor-actuator pairs to introduce inherent violation of parity and time symmetry, and achieve linear acoustic nonreciprocity.

6.2 Methods

In our approach, we use an asymmetric unit cell consisting of a sensor and actuator pair, separated from one another by a subwavelength distance , as shown in Fig. 6.1. The pairs are arrayed and interlaced along the length of the waveguide. This arrangement breaks spatial symmetry and creates a preferential direction be-

cause information is transmitted nearly instantaneously in a unidirectional fashion from sensor to actuator via a distributed amplifier network, while acoustic disturbances propagate bidirectionally at the much slower group velocity of the waveguide. This nonlocal spatial feed forward (NAM) concept is similar to the canting of the hair cells and phalangeal processes seen in the mammalian cochlea, a feature hypothesized to play a role in wave amplification and dispersion in the hearing organ [44].

To illustrate this general NAM concept as a tool to engineer nonreciprocal behavior, we use an airborne acoustic system as shown in Fig. 6.1(A), although this paradigm could be adapted for other wave-bearing media, like piezoelectric or magnetoelastic materials, with appropriate electronic control. First we consider the system in the limit where the acoustic wavelength is much larger than the spacing between successive sensors or actuators (Δx) so we can treat the active medium as a continuum. The sensed pressure is fed forward to the monopole sources located at a distance d_{ff} downstream. If we assume that the source can be manipulated electronically to precisely match the upstream pressure and that the electronic control is instantaneous, the acoustic source strength can be written as $g_p p(x - d_{ff})$, where g_p is the open loop gain between the sensor and the actuator. This simplifying assumption will be relaxed later to reflect the dynamics of the acoustic source. In the long wavelength regime, where the acoustic wavelength is much larger than the spacing between consecutive actuators ($\lambda >> \Delta x$), the discrete acoustic sources can be treated as a continuum source of strength $g_p p(x - d_{ff}$. In this limit, the pressure in the waveguide (p) can be modeled using the one dimensional Helmholtz equation as

$$\frac{d^2p}{dx^2} + k^2 p = \begin{cases} g_p p(x - d_{ff}), & 0 \leq x \leq L \\ 0, & \text{otherwise,} \end{cases} \tag{6.1}$$

where $k = \omega/c$, ω is the angular frequency, and c is the acoustic speed in air. The

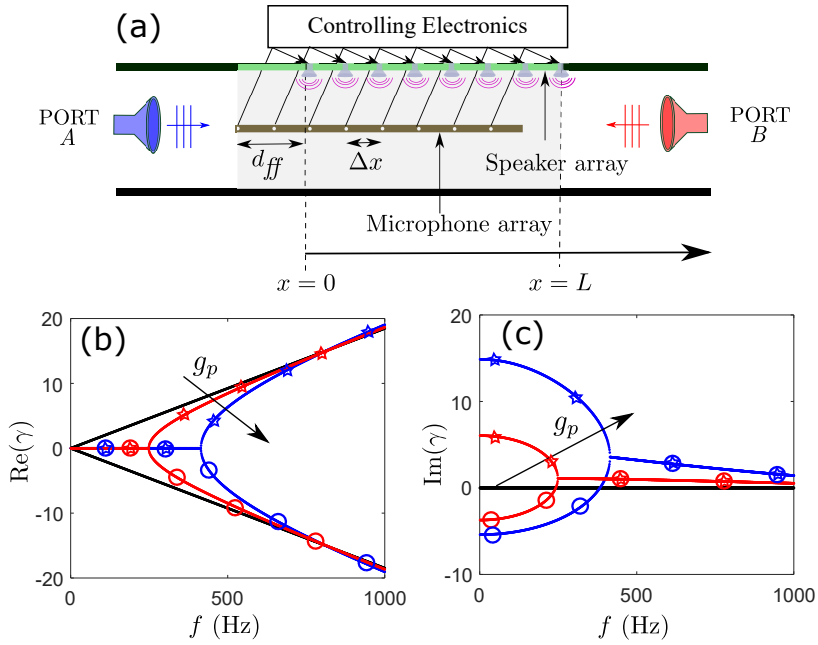

Figure 6.1: (A) Example configuration of the NAM concept applied to an air-borne acoustic medium. The sensors (microphones) and actuators (speakers) are arrayed along the waveguide and the output of each sensor is fed forward a distance d_{ff} to its corresponding actuator. (B) Real part and (C) imaginary part of the first two root loci of the complex wavenumber solutions to Eq. (3) for $d_{ff} = 10$ cm, and g_p set to three values, $g_p = 0$ m^{-2} (black), $g_p = 20$ m^{-2} (red) and $g_p = 50$ m^{-2} (blue). Colored stars (circles) are used to delineate the right (left) going waves.

active section of the waveguide ($g_p \neq 0$) extends from $x = 0$ to $x = L$. Let $p^I(x)$ be the solution of Eq. 6.1 due to a point source Q^I at $x = x_1$ and $p^{II}(x)$ the solution due to a point source Q^{II} at $x = x_2$, where $x_1 < 0$ and $x_2 > L$.

$$\frac{d^2p^I}{dx^2} + k^2 p^I = \begin{cases} g_p p^I(x - d_{ff}), & 0 \leq x \leq L \\ Q^I \delta(x - x_1), & \text{otherwise,} \end{cases} \tag{6.2}$$

$$\frac{d^2p^{II}}{dx^2} + k^2 p^{II} = \begin{cases} g_p p^{II}(x - d_{ff}), & 0 \leq x \leq L \\ Q^{II} \delta(x - x_2), & \text{otherwise,} \end{cases} \tag{6.3}$$

Multiplying Eq. 6.2 with p^{II} and Eq. 6.3 with p^I, subtracting and integrating from $((\infty, \infty))$ along with the continuity of pressure and velocity yields

$$-\int_0^L g_p(p^I I(x)p^I(x-d_{ff}) - p^I(x)p^{II}(x-d_{ff}))dx = p^I I(x_1)Q^I - p^I(x_2)Q^I I. \quad (6.4)$$

Acoustic reciprocity requires $p^I I(x_1)Q^I - p^I(x_2)Q^I I = 0$, which is possible only if $d_{ff} = 0$. Since the non-local active mdium (NAM) mechanism requires that the sensors and actuators be non-collocated, i.e. $d_{ff} \neq 0$, this system is inherently nonreciprocal, except at certain exceptional frequencies.

The spatial separation of the sensor and the actuator and the unidirectional sensor-signal transmission are the crucial elements in achieving inherent nonreciprocity in the NAM system. This is fundamentally different from the case where active elements of an acoustic waveguide are coupled via a bidirectional transmission line [8], because such a system is reciprocal. The nonlocal approach is also different from case where the sensor and source are collocated and local impedance modification or bianisotropy is utilized to achieve nonreciprocity, because the nonlocality, even though subwavelength, affords addition flexibility in achieving nonreciprocity.

6.3 Results

6.3.1 The Continuous-Source NAM System

To further investigate the nonreciprocal wave characteristics of the NAM, we assume harmonic waves of the form to obtain the dispersion relation in the active region (Eq. 6.1) given by

$$-\gamma^2 + k^2 = g_p e^{-i\gamma d_{ff}}, \quad (6.5)$$

where γ is the wavenumber. Owing to the exponential term on the right-hand side of Eq. 6.5 there are an infinite number of complex root loci and the equation is not

even in γ. In order to show the evolution of the complex wavenumber-frequency loci with increasing gain, we plot the real part of the wavenumber in Fig. 6.1(B) and the imaginary part in Fig. 6.1(C) for the first two root loci. Two nonzero values of are chosen, $g_p = 50$ m^{-2} (in blue) and $g_p = 20$ m^{-2} (in red). The nondispersive and purely real wavenumber loci of the passive case ($g_p = 0$ m^{-2}) are shown for reference with black lines. For both active loci, the allowed waves are purely evanescent at low frequencies and asymmetric about the ordinate, indicating directionally dependent phenomena. The loci for both choices of nonzero gains exhibit a bifurcation point beyond which the solutions exhibit decay in the left-to-right direction ($A \rightarrow B$ in Fig. 6.1) and growth in the right-to-left direction ($B \rightarrow A$), demonstrating spatial nonreciprocity of the active waveguide. These gains yielded stable temporal solutions for the unbounded case, as confirmed by simulating the impulse response of the active waveguide. Increasing the gain changes the asymmetry of the evanescent component of the wavenumber, increases the frequency where the bifurcation point occurs, and eventually results in instability.

6.3.2 The Discrete Source NAM

To determine if the nonreciprocity seen in the continuous system is conveyed to a system composed of discrete sensors and actuators, we consider an array of uniformly spaced pairs ($\Delta x = 10$ cm) arranged in the active section in an infinite acoustic duct as shown in Fig. 6.1(A). We retain the assumption that the electronics can provide the gain necessary to guarantee that the acoustic source strength of each actuator is equal to the discrete gain, g_d , times the measured pressure at a distance 10 cm upstream, similar to the source term in Eq. 6.1. We modeled this numerically in two ways. First, we used one-dimensional (1D) acoustic theory, with the actuators idealized as point sources. Second, we used a full-wave (FW) solution that consisted of a complete three-dimensional finite element acoustic model in Comsol Multiphysics

that included the finite extent of the sources, treated as boundary velocity forcing, and three dimensionality of the fluid domain. Parameters for the 1D and FW models are given in Appendix C.

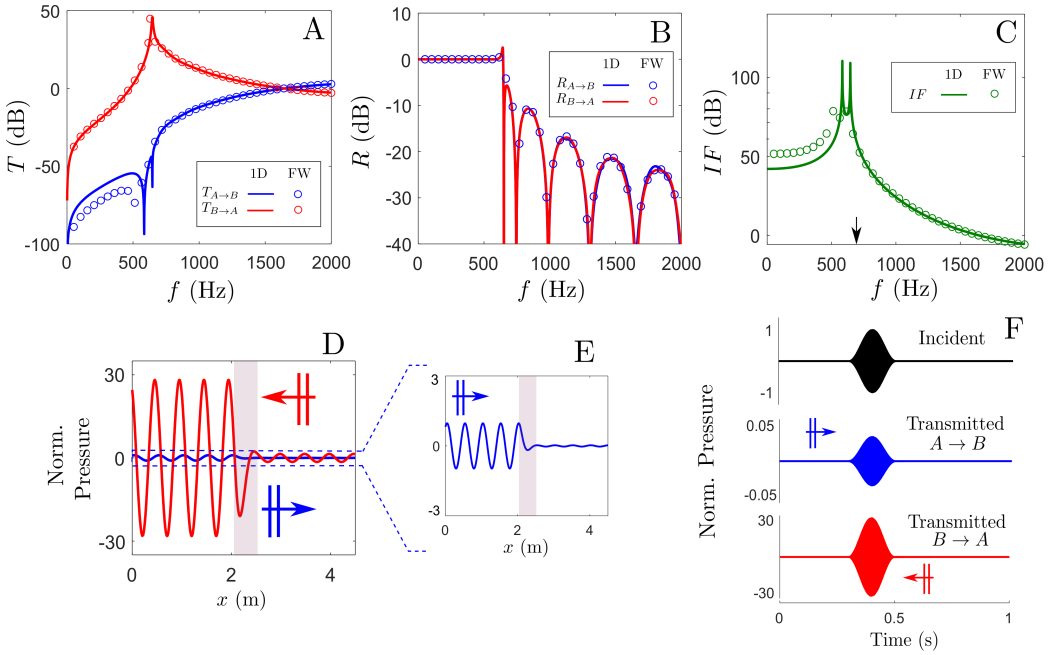

Figure 6.2: The (A) transmission and (B) reflection coefficients of the discrete realization of the active waveguide for a wave traveling from port A to B (blue) and from port B to A (red) as obtained from full wave (FW) simulations (solid lines) and 1-D simulations (circles). (C) The isolation factor (IF) derived from the transmission and reflection spectra from (A) and (B). (D) FW simulation of the spatial pressure field for a plane wave incidence from port A (blue) and port B (red) at 692 Hz (frequency shown with black arrow in (C)) showing 29 dB of amplification for propagation from B to A and 31 dB of attenuation for propagation from A to B. A magnified view of the wave propagating from A to B is shown in (E). (F) The time evolution of the wave envelopes of the transmitted pressure at the output of the waveguide due to a 0.2 s cosine squared pulse centered at 692 Hz incident from port A (blue) and port B (red) are shown. The incident pulse is shown (black) for reference. Notice the different pressure scales associated with the incidence directions in (D–F). A constant and uniform gain of $g_d = 4.5$ m^{-1} has been used for each sensor-actuator pair in all simulations.

We define the transmission coefficient (T) as the ratio of the amplitude of the transmitted and the incident pressure field, and the reflection coefficient (R) as the ratio of the amplitude of the reflected and the incident field, expressed in dB. For a plane wave incident from port A, the subscript $A \to B$ is used while the subscript

$B \rightarrow A$ represents the opposite situation. As shown in Fig. 6.2, over the frequency range plotted (except at an exceptional frequency) $T_{A\rightarrow B} \neq T_{B\rightarrow A}$ resulting in a non-symmetric scattering matrix, demonstrating the nonreciprocal nature of the system. The reflection coefficients (Fig. 6.2(B)) are equal in amplitude, but differ in phase by $2kd_{ff}$ radians for our equispaced sensor-actuator system. This is in stark contrast with $\mathcal{PT}$ symmetric systems, where the transmission coefficients from either direction are the same and the reflection coefficients differ[163].

To understand this deviation of the transmission and reflection coefficients from other systems in literature, consider a set of N pairs of sensors and actuators cascaded along the duct. Let the coordinates of the sensors be at $X_p = x_{p,1}, x_{p,2}, {x_{p,N}}^T$ and the coordinates of the actuators be at $X_S = x_{s,1}, x_{s,2}, {x_{s,N}}^T$. Without loss of generality, let $x_{s,1} = 0$ and $x_{s,N} = L$. The coordinates of the m$^{\text{th}}$ sensor can be written as $x_{p,m} = (m-1)\Delta x - d_{ff}$, and the coordinate of the n$^{\text{th}}$ actuator can be written as $x_{s,n} = (n-1)\Delta x$. The total pressure field at any location x can be written as a linear superposition of the incident pressure field, $p_{inc} = p_0 e^{ikx}$ and the scattered pressure field, $p_{sc} = \frac{g_d}{2ik}\sum_{j=1}^{N} e^{ik|x_{s,j}-x|}P_p^j$, where P_p^j is the pressure detected at the j$^{\text{th}}$ sensor and are given by Eq. S4. The reflection and transmission coefficients can be written as

$$\begin{aligned} R_{A\rightarrow B} &= \sum_{n=1}^{N}\sum_{m=1}^{N}\frac{1}{2ik}e^{ik(n-1)\Delta x}H_{nm}e^{ik(m-1)\Delta x}e^{-ikd_{ff}}, \\ T_{A\rightarrow B} &= e^{ik(N-1)\Delta x} + \sum_{n=1}^{N}\sum_{m=1}^{N}\frac{1}{2ik}e^{ik(n-1)\Delta x}H_{nm}e^{ik(m-1)\Delta x}e^{-ikd_{ff}}, \end{aligned} \tag{6.6}$$

where $H = g_d(I - gG)^{-1}$. Here G_{ij} is the Greens function from the j$^{\text{th}}$ actuator to the i$^{\text{th}}$ sensor. To simplify the calculation of the reflection and transmission coefficients for waves impinging from port B, we choose a different set of coordinates such that $x_{s,1} = L$ and $x_{s,n} = 0$, as shown in Fig. S4B. In this coordinate system, the coordinate

of the m$^{\text{th}}$ sensor can be written as $(N-m)\Delta x + d_{ff}$, and the coordinate of the n$^{\text{th}}$ actuator is $(N-n)\Delta x$. Note that the choice of coordinates does not affect the calculation of the reflection and transmission coefficients. The reflection and transmission coefficents for a wave impinging on the NAM system from port B can be written as

$$\begin{aligned} R_{B\to A} &= \sum_{n=1}^{N}\sum_{m=1}^{N} \frac{1}{2ik} e^{ik(N-n)\Delta x} H_{nm} e^{ik(N-m)\Delta x} e^{ikd_{ff}}, \\ T_{BA} &= e^{ik(N-1)\Delta x} + \sum_{n=1}^{N}\sum_{m=1}^{N} \frac{1}{2ik} e^{ik(N-n)\Delta x} H_{nm} e^{ik(N-m)\Delta x} e^{ikd_{ff}} \end{aligned} \tag{6.7}$$

Now, under the assumption that d_{ff} and the sensor-actuator gain g_d is constant across all pairs, the matrix G is a persymmetric matrix, i.e. $G_{m,n} = G_{N-n+1,N-m+1}$. This results in $H = g_d(I - g_d G)^{-1}$ inheriting persymmetry, and consequently $H_{m,n} = H_{N-n+1,N-m+1}$. The reflection and transmission coefficients can now be simplified to

$$\begin{aligned} R_{B\to A} &= \sum_{n=1}^{N}\sum_{m=1}^{N} \frac{1}{2ik} e^{ik(n-1)\Delta x} H_{nm} e^{ik(m-1)\Delta x} e^{ikd_{ff}}, \\ T_{B\to A} &= e^{ik(N-1)\Delta x} + \sum_{n=1}^{N}\sum_{m=1}^{N} \frac{1}{2ik} e^{ik(n-1)\Delta x} H_{nm} e^{ik(m-1)\Delta x} e^{id_{ff}} \end{aligned} \tag{6.8}$$

Comparing Eq. 6.6 and Eq. 6.8, we see that $|R_{A\to B}| = R_{B\to A}|$ and the reflection coefficients differ in phase by $2kd_{ff}$ radians. The transmission coefficients do not have any simple relationship. It is remarkable that the persymmetry in the NAM system yields very different results from $\mathcal{PT}$ symmetric reciprocal systems. In $\mathcal{PT}$ symmetric systems, calculation of reflection and transmission coefficients yields $|T_{A\to B}| = |T_{B\to A}|$ (which support reciprocity) and $R_{A\to B}| \neq |R_{B\to A}|$, whereas in the NAM system, $|T_{A\to B}| \neq |T_{B\to A}|$ and $R_{A\to B}| = |R_{B\to A}|$.

Further, if the actuator has sufficient authority to deliver pressure at very low frequencies, this system reflects incoming waves from both directions at those frequencies, acting as a subwavelength wall for sound. The FW simulations are in good agreement with the 1D acoustic theory in this frequency range. The degree of non-reciprocity quantified by the isolation factor (IF), defined as the difference of $T_{A\to B}$ and $T_{B\to A}$, exceeds 40 dB over a broad range of frequencies from DC up to 800 Hz, as shown in Fig. 6.2(C), and displays a 20 dB IF bandwidth of more than 1 kHz.

To further elucidate the effectiveness of the NAM, the spatial variation of the real part of the total pressure field due to incidence of 692 Hz plane wave from port A is shown in Fig. 6.2(D) and incidence from port B in Fig. 6.2(E). This frequency was chosen to establish the efficacy of the active waveguide away from the maximum IF. The plane wave incident from port B (Fig. 6.2(D)) is amplified by 29 dB whereas the wave incident from port A (Fig. 6.2(E)) is attenuated by 31 dB, leading to a remarkable net acoustic IF of 60 dB. To determine the effectiveness of the distributed active media under transient loading, we simulated the response of the active waveguide to a cosine squared windowed incident pulse 0.2 s in duration and centered at frequency of 692 Hz, the envelope of which is shown in Fig. 6.2(F). Time domain calculations show that the transmitted wave packets exhibit minimal distortion, and the wave packet traversing from port B to A (red line) is amplified, whereas the transmitted wave packet traveling from port A to B (blue line) is reduced, consistent with the 60 dB IF predicted by the steady state response.

6.3.3 Stability of the NAM System

Stability in active feedback systems is of paramount interest while designing the system. We studied the stability of the NAM system to delineate our operational bounds for the gain g_d between the sensors and actuators. We demonstrate our calculations by considering the air-borne acoustic feedforward system is shown in

Fig. 6.1(A). The N sensors and actuators are aligned along the duct and the spacing between two consecutive sensors is Δx. The Greens function for a one dimensional infinite acoustic duct is given by

$$G(x,y) = \frac{1}{2ik} e^{ik|x-y|}. \tag{6.9}$$

The pressure at each sensor can be written as a superposition of the pressure from the incoming plane wave and the pressures due to each of the N actuators as

$$P_p^i = p_0 e^{ikx} + \frac{1}{2ik} \sum_{j=1}^{N} e^{ik|x_{p,i} - x_{s,j}|} S(x_j), \tag{6.10}$$

where the pressures at the i$^{\text{th}}$ sensor located at position $x_{p,i}$ is P_p^i and the strength of the acoustic source due to the j$^{\text{th}}$ actuator located at position $x_{s,j}$ is $S(x_j)$. If the source strength of each actuator $S(x_j)$ is set to the value of the pressure detected by its corresponding upstream sensor (P_p^j) modulated by a gain g_d, the pressures at the N sensors can be written in a vector form as

$$P_p = p_0 (I - g_d G)^{-1} e^{ikX_p}, \tag{6.11}$$

where $P_p = [P_p^1, P_p^2, \ldots, P_p^N]^T$, $X_m = [x_{p,1}, x_{p,2}, \ldots, x_{p,N}]^T$, and $G_{ij} = \frac{1}{2ik} e^{ik|x_{p,i} - x_{s,j}|}$. The above equation is in the canonical form of a multiple input multiple output closed loop control system, and we determined the range by determining the winding number of the scalar function $\det(I - g_d G)$ along the Nyquist contour. Fig. 6.3 shows the variation of winding number with gain for $N = 10$ sensor-actuator pairs as discussed in the previous section. The gains corresponding to trivial winding numbers are associated with stable NAM system and are shown with the shaded region.

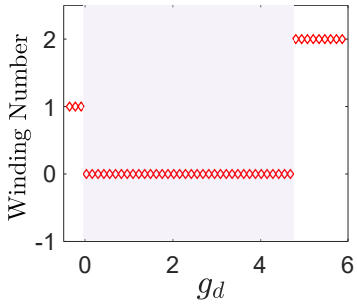

Figure 6.3: The winding number variation with gain for $N = 10$ pairs of probes and actuators. The source strength is assumed to be equal to the pressure at the upstream probe modulated by a scalar gain g_d. The system is stable when the winding number of $\det(I - g_d G)$ along the Nyquist contour is equal to zero. Using this design, the system is stable when the discrete gain $g_d \in (0, 4.6)$, and the stability boundary is shown with the shaded box.

6.3.4 NAM with speaker and microphones

To verify the viability of the spatial feed-forward control with real electromechanical transducers, we relaxed the assumption that the source strength is precisely equal to the sensed pressure, as introduced in Eq. 6.1. Instead, we used the voltage output from each microphone (sensor) multiplied by a gain factor as the input voltage to the corresponding electrodynamic speaker (actuator) to simulate a real experiment. Using standard electrodynamic driver theory, we modeled each of the 10 sources with the nominal Thiele-Small parameters for a typical minispeaker, as documented in Appendix C. Fig. 6.4(A) shows the IF spectrum for the stable discrete gains, $g_d = 0.01$, 0.04, 0.086 m^{-1} (light to darker shades of green), and passive waveguide ($g_d = 0$ m^{-1}) to show the change in the IF spectrum with decreasing gain. To demonstrate the electronic tunability of the system, we added a single pole low pass filter to the electronic controller. Fig.6.4(b) shows the effect of adding the low-pass filter in series with the scalar gain g_d. The low pass filters have corner frequencies 2000 Hz (LPF_1) and 600 Hz (LPF_2). The gain was reduced $g_d = 0.07\mathrm{m}^{-1}$ to ensure stability. Addition of the low pass filters lowered the peak IF frequency by 140 Hz and 290 Hz for LPF_1 and LPF_2 respectively, as shown in Fig. 6.4(b). Fig.6.4(c) shows the spatial variation

of the pressure field at 900 Hz with no low pass filtering. For 1 Pa incident field, the voltage applied to the speakers remained under the maximum voltage rating for this speaker over the entire range of frequencies. Our calculations predict a maximum stable IF of 70 dB at 900 Hz. We define Δf_{IF} as the 20 dB IF bandwidth, and calculated it to be 456 Hz for this system, equal to 50% of the peak IF frequency. Other studies utilizing linear mechanisms to achieve nonreciprocity have reported peak IF magnitudes of around 40 dB (Δf_{IF}=4 Hz) for the acoustic circulator [37] and 25 dB (Δf_{IF}=250 Hz) for the Willis metamaterial [161]. Hence, this proposed mechanism has the potential to exceed the maximum level and bandwidth achieved by other approaches [37, 161] without disrupting mean fluid flow. Further, the IF spectrum can be manipulated by electronically modulating g_d, either in magnitude or in phase (see Fig.6.4(a) and (b)), providing a highly flexible mechanism for *in situ* optimization of the NAM system for specific applications.

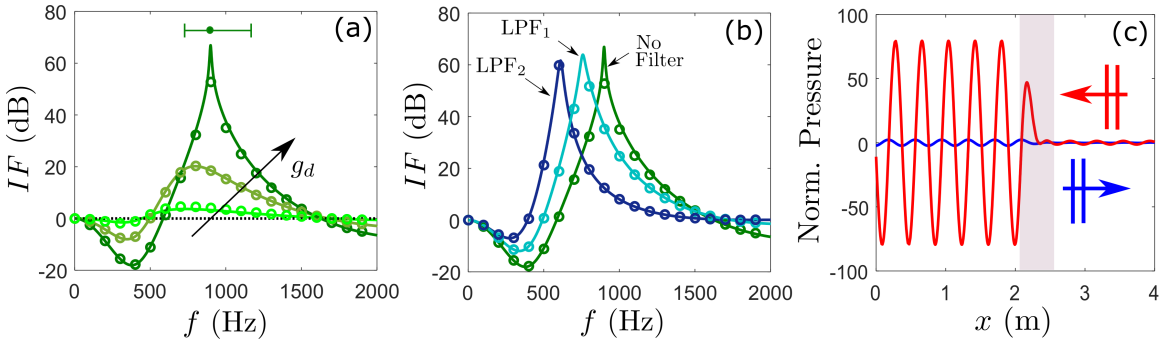

Figure 6.4: Nonreciprocity in the NAM system with actuators modeled as electrodynamical speakers. (a) The curves show the transition of the IF for $g_d = 0.01\,\mathrm{m}^{-1}$, $0.04\,\mathrm{m}^{-1}$, and $0.086\,\mathrm{m}^{-1}$ (light to dark shades of green) along with $g_d = 0\,\mathrm{m}^{-1}$ (black). The solid lines are from 1D calculations and the symbols are from FW calculations. The 20 dB IF bandwidth is shown as a horizontal line at the top of the plot with the peak IF frequency indicated with a filled circle. (b)Modification of the IF spectra by electronic filters, demonstrating electronic tunability of the system. Addition of a low pass filter in the electronic control moved the frequency of the peak IF by more than half an octave. The gains used were $g_d = 0.086\,\mathrm{m}^{-1}$ without any filter, and $g_d = 0.07\,\mathrm{m}^{-1}$ for filters with corner frequencies at 2000 Hz (LPF$_1$) and 600 Hz (LPF$_2$). (c) FW simulation of the spatial distribution of the pressure field for a 900 Hz unit amplitude plane wave propagating from B to A (red) and from A to B (blue). The active section is shown with the shaded box.

6.4 Discussion

We have shown that it is possible to induce linear broadband nonreciprocity in acoustic systems, essentially creating a new stable media using the NAM mechanism. This mechanism consists of an array of interlaced subwavelength sensor-actuator unit cells (the total active region can be sub- or supra-wavelength). Although we have demonstrated the approach using a fluid-acoustic medium, this technique can be adopted and applied to many different wave-bearing media and systems. For instance, the locally sensed force or strain in either an interdigitated surface acoustic wave device [6, 68, 137] or a layered stack of bulk-wave piezoelectric elements [70, 108] can be fed forward to actuator elements using the NAM approach, creating a preferred direction and nonreciprocity. The NAM approach expands the design space, holding the potential to enhance the desired capability of the device (e.g., filtering or sound output). An extensively studied prototype for wave propagation and control in dispersive systems is an elastic beam bounded to piezoelectric patches arrayed down the beam. When the piezoelectric elements are electrically interconnected by a transmission line, a coupled elastic-electric waveguide is created [151]. While this coupled waveguide system can be designed to achieve excellent stop-band behavior or high losses, it is still reciprocal. By breaking the bidirectionality of the transmission line using the feed forward distributed control of the NAM, these reciprocal systems would be converted to nonreciprocal ones. Another popular approach is to use collocated sensor-actuator patch approaches to control wave propagation on beams, as in [2]. These too can be converted to nonreciprocal systems by feeding forward the control signal to the neighboring patch. Finally, one can also envision creating nonreciprocal anisotropy in two-dimensional media, potentially enabling one-way waveguding. Hence, our theoretical work opens up the possibility of reconfiguring a vast array of well-studied systems rendering them nonreciprocal. While we have used a gain which is spatio-spectrally constant, exploring the vast design space associated with

the spatio-spectral variation of the amplitude and phase of the gain associated with each sensor-actuator pair as well as the distance between them holds great potential for noise control as well as for enhancement of the performance of electromechanical filters and amplifiers.

CHAPTER VII

Contributions and Future Work

7.1 Contributions

7.1.1 Computational Model of the Cochlea

Over the last several decades, numerical models of the cochlea have undergone significant development and are now capable of predicting and explaining many subtle phenomena that have been experimentally observed and correlated with cochlear physiology. However, there are several fundamental questions remain unanswered by these models. In this thesis, we have explored some of these questions and answered them qualitatively and quantitatively through a computational model of the cochlea.

- The MET channel noise dominates the hydrodynamic viscous noise in the bullfrog transduction process [95]. However, the same may not be true for mammalian transduction. This is because the hair bundles in the bullfrog cochlea are free standing whereas the hair bundles in the mammalian cochlea are embedded in a very narrow subtectorial space. Consequently, the fluid environment around the mammalian hair bundles is significantly different from that of the bullfrog. This had led to a longstanding question whether the MET channel noise dominates the transduction noise in mammals as well. In this thesis, we have developed quantitative estimates for the MET and viscous noise in the

mammalian cochlea through a combination of numerical and analytical frameworks. We have shown that the viscous noise dominates mammalian transduction at the base of the cochlea whereas MET noise dominates the transduction noise at the apex. This might hint at common transduction mechanisms for low frequency hearing shared by mammals and other low-frequency hearing animals, and that mammals might have developed specialized adaptations for high frequency transduction [24]. This work was published in the Biophysical Journal [129].

- The mechanical [115, 18], neural [123] and otoacoustic delays [136] at the apex are distinctly different from those at the basal turn of the cochlea. This violation of scaling symmetry at the apex of the mammalian cochlea has been a challenge for cochlear mechanics modelers for the last several decades. In this thesis, we have developed the first physiologically based model of the mammalian cochlea that can recreate the tuning of the cochlea at all locations. We have shown that the apical-basal differences can be explained by accounting for the boundary layer interactions at the apex along with the change in the cytoarchitecture of the organ of Corti. Including these physical effects lead to a unified model that can explain the mechanical and neural tuning at all turns of the cochlea without the need for any special cellular mechanism at the apex as hypothesized in [116]. This work was published in the Proceedings of the National Academy of Sciences [130].

- Intracochlear electrically evoked otoacoustic emissions (EEOAE) are an excellent controlled experimental paradigm to study the forward and reverse delay of waves inside the cochlea. However, reverse delays calculated from 1-D theoretical models disagree with the delays estimated from EEOAEs measured in the mouse and gerbil cochlea [52, 118]. Previous model results predict that

waves generated inside the cochlea travels on the cochlear partition as a reverse propagating wave, reaching the stapes at time approximately equal to the forward acoustic delay t_g, and are reflected back to the generation site at time $2t_g$. However, experimental EEOAE measurements show that bipolar stimulation of the cochlea with electrodes placed in the walls of the scala media (SM) and scala tympani (ST) results in EEOAEs with delay of around 50 μs followed by a delayed excitation at the stimulation location at t_g. In this thesis, we developed the first computational model of the mammalian cochlea that can accurately predict EEOAEs and cochlear response to electrical stimulation. We have shown that the experimental measurements can be explained by considering the spatial spread of the current in the ST and that the placement of the electrode in the ST can drastically change the temporal response at the stapes and the stimulation location. We have used this model to interpret of otoacoustic delays generated by various experimental paradigms. Our model has the potential to better understand otoacoustic emissions of all kinds and aid in accurately correlating otoacoustic emissions with pathologies in the auditory periphery.

7.1.2 NAM

The ability to create compact nonreciprocal media has long been an outstanding challenge in wave dynamics. In electrodynamical media, this is often achieved with Faraday isolators and circulators [146]. However, the speed of light is much higher than the speed of sound in acoustic media and hence strategies that work for electrodynamical media are often not best suited for acoustics. Recently, various methods of achieving nonreciprocity in acoustics have been proposed [8, 36]. However, these methods are nonlinear, exhibit narrowband nonreciprocity and/or are not compact. In this thesis, we have proposed a generalized framework for a compact acoustic

metamaterial that achieves linear, nonreciprocity over a broad range of frequencies through a distributed sensor-actuator control system. Further, this system is electronically tunable, a property that is not found in the other nonreciprocal systems in literature. Our electronic control framework is flexible in its implementation and can be used to modify existing acoustic media to break reciprocity. This work is currently a preprint on arXiv [128], and has been submitted for publication in a refereed journal.

7.2 Future Work

7.2.1 Computational Model of the Cochlea

We have presented results from a physiologically based model of the cochlea that replicates the mechanical responses to acoustic and electrical stimuli over the entire length of the spiral, and predicts ANF thresholds. Like most models that use a simplified geometry, the helicotrema was modeled as an opening in the cochlear partition at the apical end. However, the *in vivo* geometry of the helicotrema is complex and warrants more detailed 3D finite element modeling, especially to model the response below 100 Hz. In addition, only the Couette flow was included in the STS, and other modes of fluid structure interaction [102] were not modeled due to the additional complexity. However, these modes might play an important role in predicting the non-tip response in the threshold ANF FTCs [96].

Moreover, although we have analyzed the signal and noise in the cochlea over many spatial and temporal scales, and to a variety of excitation, we have made a key assumption that the linearized cochlear model can accurately capture the nonlinear effects by changing the MET sensitivity [114], inline with the EQ-NL theorem [25]. However, several nonlinear phenomenon like the generation and emission of DPOAEs and SFOAEs cannot be explained using a linearized model. CSound has provisions for

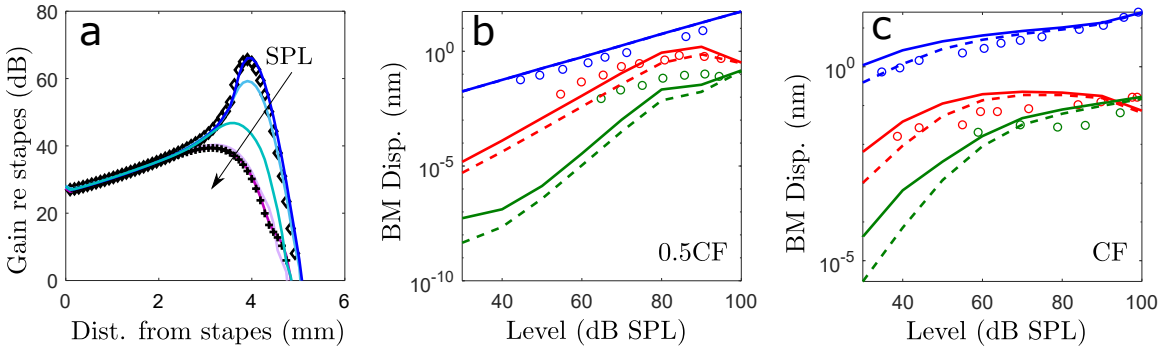

Figure 7.1: Calculations from the nonlinear cochlear model. (a) Comparison of BM gain at varying SPLs (colored lines) with results from the linearized model (black symbols). (b,c) Comparison of fundamental (blue), second harmonic (red) and third harmonic (green) I/O growth curves from the model with growth curves obtained from experiments in the guinea pig cochlea [16] shown with colored symbols. Note that the strength of the higher harmonics calculated from the model at low SPLs are lower than the displacement resolution that was available in this experiment.

nonlinear simulation using both time domain (TD) as well as alternate time-frequency (ATF) analysis, as documented in Chapter I. One of the key advantages of ATF over time domain formulations is the ability to include boundary layer interaction within the nonlinear framework. This is necessary to obtain realistic results at the apical end of the cochlea. Preliminary results in the basal end of the cochlea (Fig. 7.1(a)) show good agreement between the results obtained from ATF (colored lines) with the calculations from the linearized frequency domain formulation (symbols) at low and high stimulus levels. The nonlinear calculations are in good agreement with the linearized results at both high and low SPLs. Further, the BM input-output (I/O) growth curve obtained from the ATF formulation are in good agreement with the data obtained from experimental measurements (Fig. 7.1(b,c)). With the inclusion of the duct taper and boundary layer viscosity, the current model can be used to probe the nonlinear mechanics at the apical end of the cochlea, which has not been investigated in literature.

Recent experiments in the gerbil cochlea [32, 19] have shown that the I/O growth curves for the RL or the OHC region shows hypercompression instead of the usual

compressive behavior seen in the BM. Moreover, this hypercompressive growth is present much below the CF whereas the BM nonlinear growth is only observed close to the CF. Calculations from our model show similar hypercompression in the I/O growth curve of the RL (apical surface of the OHC). Fig. 7.2(a,b) shows the spatial distribution of the RL and BM amplitude with increasing stimulus levels. The BM compression stays localized to the best place but the RL shows compressive growth at locations basal to the best place. Fig. 7.2(c) shows the I/O growth curvs for the RL and the BM at the fundamental and the second harmonic. The BM growth curve is monotonous and compressive, whereas the RL growth curve is non-monotonous and hypercompressive. Using this model, it will now be possible to study the non-linear growth in the OHC electromotility and the cochlear microphonic and their implications for non-invasive diagnoses of cochlear health.

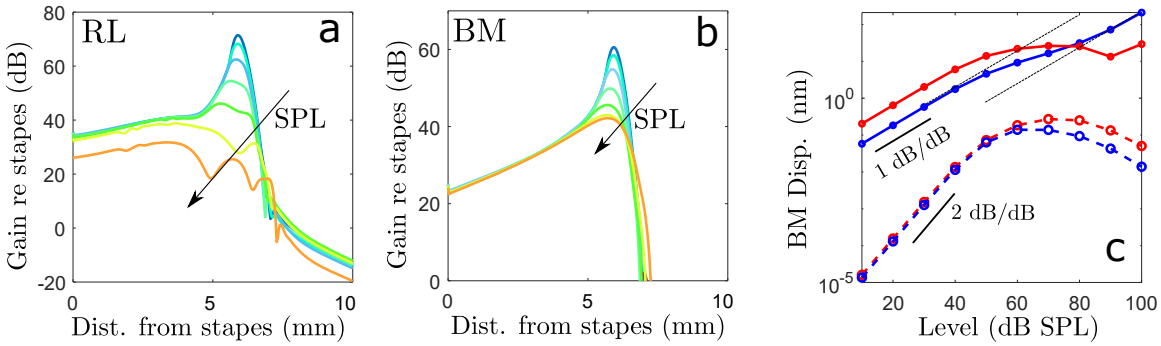

Figure 7.2: Calculation of RL and BM response from model with increasing stimulus level. (a,b) show the spatial distribution of the (a) RL and (b) BM amplitude as the stimulus level is increased (different colored lines). The BM nonlinear response is localized to the best place wherea the RL nonlinear response extends basally. (c) shows the I/O growth curves for the BM (blue) and the RL (red) at the fundamental (solid lines) and the second harmonic (dashed lines) calculated from the model at the location corresponding to the maximal response at the fundamental. The symbols show the discrete levels where the calculations were performed and the lines are extrapolated between them. At the fundamental, the BM growth curve shows compression whereas the RL growth curve shows hypercompression. Both the BM and the RL exhibit non-monotonous growth at the second harmonic. The black lines show the asymptotic slopes of the BM growth curve at low and high stimulus levels.

Past computational models of the cochlea have modeled the OoC as acoustically

transparent, such that the the fluid pressure in the SM is coupled only to the BM. However, in the physiological cochlea, the fluid in the SM is partially coupled to the TM as well. This work can be extended to develop a computational model of the cochlea where the scala vestibuli fluid pressure is distributed on both the TM as well as the BM in accordance with the geometry of the OoC, and study its implications on the excitation of the cochlear hair cells, and the generation and propagation of otoacoustic emissions out of the cochlea.

7.2.2 NAM

In this thesis, we have presented a generalized framework to analyze and design nonreciprocal feedforward systems, and demonstrated a single instantiation of the system in one dimension using electrodynamic speakers and microphones. However, one can envision using a similar strategy to control the acoustic propagation of waves on beams or plates in two dimensions or even a composite structure in three dimensions. For example consider the system shown in Fig. 7.3. The sensors (green cylinders) and actuators (blue cylinders) are staggered and cascaded along the plate, with each sensor feeding information to a downstream actuator as shown with red arrows. The whole system is symmetric about the centerline. Such a system is highly anisotropic and nonreciprocal in the both the x and y directions, and could be used to generate directional bangaps with applications in MEMS devices. Using the formulation introduced in Chapter VI, it is possible to analyze the different instantitions of the NAM and develop control strategies to achieve the designed directional wave dynamics.

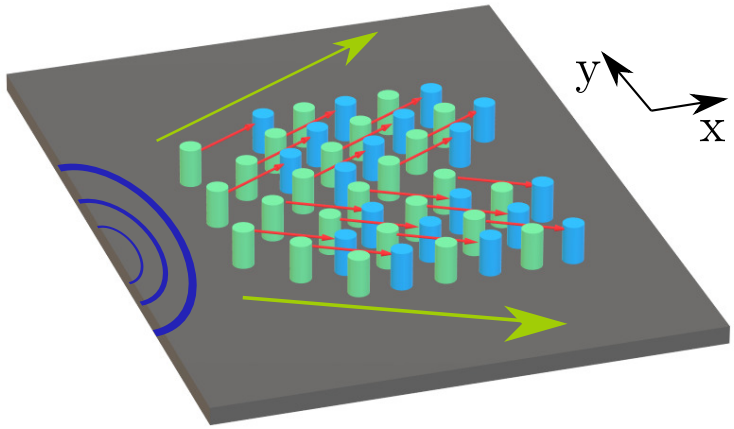

Figure 7.3: Conceptual design of the NAM on a plate. The incoming acoustic wave is shown on the left. Each sensor (green cylinder) is fed-forward to an upstream actuator (blue cylinder). The direction of information flow is shown with the red arrows. The whole system is symmetric about the centerline. By leveraging the NAM control architecture, such a system can show electronically tunable anisotropy and nonreciprocal behavior in both x and y directions.

APPENDICES

APPENDIX A

A.1 Model

The cross-section of the organ of Corti (Fig. A.1) has been modeled as shown in Fig. A.2. In this section, the governing equations of the TM, HB and the fluid flow in the gap, along with the boundary conditions are discussed. The fluid domain is divided into two domains: Ω_{STS} and Ω_{sul}, as shown in Fig. A.2. The TM is modeled as a visco-elastic Euler Bernoulli beam of density ρ_b, area A, flexural rigidity D, height H, width W and loss tangent $\delta = 0.3$. The flexural rigidity D is calculated as $D = EWH^3(1 - i\delta)/12$, where E is the Young's modulus of the TM, 3 kPa at the base and 0.32 kPa at the apex in line with the measurements by Richter, et al[122]. The TM has been divided into two domains, Γ_{B1} and Γ_{B2} over the STS and sulcus respectively .

A.1.1 The TM beam model

Assuming harmonic excitation frequency ω, the Euler Bernoulli beam equations for the TM transverse displacement w^b in the STS and sulcus are given by

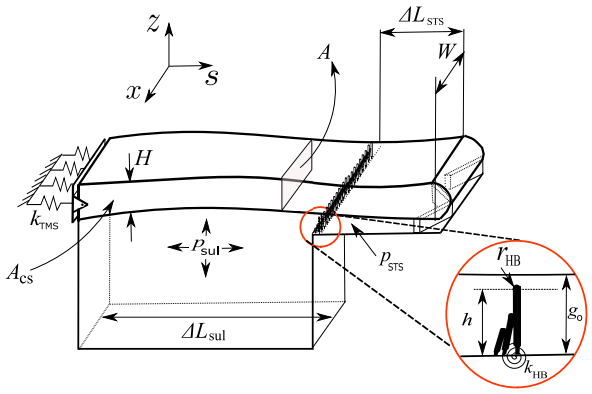

Figure A.1

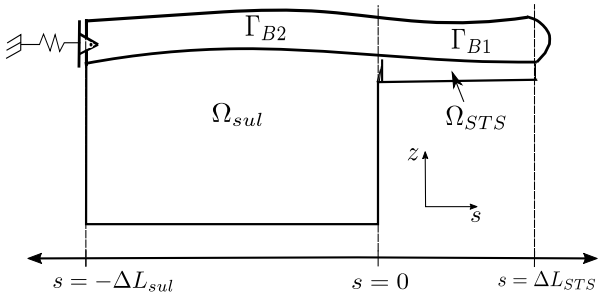

Figure A.2

Figure A.3: The OoC model. (a) The idealised model of the gerbil OoC. The inset shows the magnified view of the IHC HBs. (b) The 2D geometry of the OoC model. The TM has been divided into two domains, Γ_{B1} and Γ_{B2}, over the STS and sulcus respectively. The fluid has been divided into two domains, Ω_{sul} in the sulcus and Ω_{STS} in the STS. The three rows of OHC HBs are approximated as a single row of HBs. The IHC HBs are at the boundary of the sulcus and the STS domains.

$$(\rho_b A\omega^2 - D\frac{\partial^4}{\partial s^4})w^b + Wp_{sts} = 0, \quad s \in \mathbf{\Gamma_{B1}} \tag{A.1}$$

$$(\rho_b A\omega^2 - D\frac{\partial^4}{\partial s^4})w^b + Wp_{sul} = 0, \quad s \in \mathbf{\Gamma_{B2}} \tag{A.2}$$

where p_{sts} is the fluid pressure in the STS and p_{sul} is the pressure in the sulcus.

A.1.2 Fluid model

We assume that thin film lubrication theory holds in the STS space as the thickness of the combined Stokes boundary layers attached to the TM and the RL is greater than the height of the STS gap at acoustic frequencies. From thin film lubrication theory and no-slip boundary condition at the TM and the RL, the STS pressure is constant through the thickness and its x-s distribution is given by [74, 7]

$$(\gamma_x^2 - \frac{\partial^2}{\partial s^2})p_{sts} + (\frac{\rho_f\omega^2}{\bar{A}})w^b = 0, \quad s \in \mathbf{\Omega_{STS}} \tag{A.3}$$

where $\bar{A} = g_0 - 2\frac{\cosh(\beta g_0)-1}{\beta\sinh(\beta g_0)}$, $\beta^2 = \frac{-i\omega\rho_f}{\mu}$, and γ_x is the longitudinal (x) complex wavenumber ($\frac{1}{p_{sts}}\frac{\partial^2 p_{sts}}{\partial x^2} = \gamma_x^2$).

The sulcus fluid flow is governed by the incompressible continuity equation, given by $\nabla.\vec{v}_{sul} = 0$, where $\vec{v}_{sul}(x, s, z)$ is the fluid velocity vector in the sulcus. The flow in the longitudinal (x) direction is assumed to be inviscid as most of the losses come from the interaction with the IHC-STS. Integrating over the area of the sulcus in the $s - z$ plane, the continuity equation can be written as

$$\dot{Q}_{STS}(s = 0) + \frac{A_{sul}\gamma_x^2}{i\omega\rho_f}p_{sul} - i\omega \int\limits_{\Delta L_{sul}} w_{sul}^b(s)ds = 0, \quad s \in \mathbf{\Omega_{sul}} \tag{A.4}$$

where A_{sul} is the cross-sectional area of the sulcus, and $\dot{Q}_{STS}$ is the radial volume

flow rate of the fluid in the STS, given by

$$\dot{Q}_{STS}(s) = \frac{1}{i\omega\rho_f}\frac{\partial p_{sts}}{\partial s}\bar{A} - i\omega\bar{B}u_{TMS}, \tag{A.5}$$

where $\bar{B} = \frac{\cosh(\beta g_0)-1}{\beta \sinh(\beta g_0)}$ and u_{TMS} is the shear displacement of the TM.

In this study, γ_x is a parameter and is obtained from numerical calculations in [134] with guidance from empirical data [117]. In this work, the wave lengths ($2\pi i/\gamma_x$) are taken to be 314 µm for the basal turn, and 1256 µm for the apical turn of the gerbil cochlea. Although the γ_x at any location depends on the frequency of stimulation, in this study we have assumed a stimulation frequency independent wavelength at each location (314 µm at the base, and 1256 µm at the apex) because all results presented in this study were found to be insensitive to variation of longitudinal wavelength.

Parameter	Description	Value
$d1$	Width of the OHC HB bundles	8 µm
$d2$	Gap between the OHC HBs	2 µm
$d3$	Depth of the OHC HBs	5 µm
E	TM Young's modulus	3 kPa(base), 0.32 kPa(apex)
δ	loss tangent	0.3
A_{sul}	Area of sulcus	$40 g_0 \Delta L_{sul}$
ρ_b	Density of TM	1.03×10^3 kg/m^3

Table A.1: Parameters for the cross-section of the organ of Corti

A.1.3 TM Shear Model

The equation of motion of the TM in the radial direction can be written as in [87]

$$(k_{TMS} - GA_{cs}\gamma_x^2 - M_{TMS}\omega^2)u_{TMS} = f_\mu^{TM} + F_{TMS}, \tag{A.6}$$

where A_{cs} is the local TM cross-sectional area in the $s-z$ plane, k_{TMS} is the limbal TM attachment stiffness and G is the shear modulus for the isotropic TM. f_μ^{TM} is the

viscous force on the TM in the radial direction obtained by integrating the fluid shear force across the lower surface of the TM [7]. The fluid velocity in the STS (Ω_{STS}) is given by thin film lubrication theory, while a plane Couette flow is assumed in the radial direction in the sulcus (Ω_{sul}). The flow over the IHC and through the OHC HB gaps also causes drag. The fluid velocity profile in the IHC and OHC HB gaps are discussed later in the boundary conditions, $BC9$ and $BC10$. F_{TMS} is the external radial force on the TM used to stimulate the TM akin to the radial force applied at the outer portion of the TM by the OHC HBs. This causes the TM to displace in the radial direction, shearing the STS fluid and displacing the IHC HBs.

A.1.4 IHC HB model

The IHC HB is modeled as a stiff rod with pivot stiffness k_{HB} and height h. The equation for the IHC HB is given by

$$(k_{HB} + k_G - i\omega R_{ch})u_{HB} = f_p^{HB} + f_\mu^{HB}, \tag{A.7}$$

where the gating stiffness is given by $k_G = N k_{gs} \gamma_{HB}^2 (1 - \frac{k_{gs} d^2}{k_B T \sqrt{1+\omega^2 \tau_c^2}} P(1-P))$, where $k_{gs}d$ is the single channel gating force, γ_{HB} is the geometrical gain, P is the average MET resting probability and N is the number of MET channels. f_p^{HB} and f_μ^{HB} are equivalent tip force on the IHC HB due to the pressure differential across the HB and the shear of the fluid respectively, given by

$$\begin{aligned} f_p^{HB} &= \frac{Wh}{2}(p_{sul} - p_{STS}^+), \\ f_\mu^{HB} &= W \int_{s=-R_{HB}}^{R_{HB}} \mu \frac{\partial v_{IHC,gap}}{\partial z}\bigg|_{z=h} ds, \end{aligned} \tag{A.8}$$

where p_{STS}^+ is the pressure at the HB in $\boldsymbol{\Omega_{STS}}$.

A.1.5 TM-fluid coupling

The solutions of Eq. A.1 and Eq. A.3 are harmonic functions and the dispersion relation for the coupled STS fluid-TM system arise from the determinantal condition given by

$$\det \begin{vmatrix} \gamma_x^2 - k_{sts}^2 & \frac{\rho_f \omega^2}{\bar{A}} \\ W & \rho_b A\omega^2 - D k_{sts}^4 \end{vmatrix} = 0 \quad , \tag{A.9}$$

where k_{sts} is the radial wave number. The six roots of Eq. A.9 are $k_{1,sts}$ through $k_{6,sts}$. The coupled solution of pressure and TM displacement in the STS is given by

$$\begin{pmatrix} p \\ w_{sts}^b \end{pmatrix} = \sum_{m=1}^{6} \begin{pmatrix} \frac{\rho_f \omega^2}{\bar{A}(-\gamma_x^2 + k_{m,sts}^2)} \\ 1 \end{pmatrix} \psi_m e^{ik_{m,sts}s}, \tag{A.10}$$

where ψ_ms represent the amplitude of the solutions. From Eq. A.2, with our assumption of constant sulcus pressure in the cross-section, the TM displacement in the sulcus is given by

$$w_{sul}^b = \sum_{n=1}^{4} \zeta_n e^{ik_{n,sul}s} - \frac{p_{sul}}{\rho_b H \omega^2}, \tag{A.11}$$

where $k_{1,sul}..k_{4,sul}$ satisfy the dispersion relation given by

$$k_{sul}^4 = \frac{\rho_b A \omega^2}{D}, \tag{A.12}$$

and ζ_n are the amplitude of the solutions.

At this point, we have 13 unknowns, ψ_1 through ψ_6, ζ_1 through ζ_4, u_{HB}, u_{TMS} and p_{sul}. Along with Eq. A.4, Eq. A.6 and Eq. A.7, ten boundary conditions are required to close the problem. The boundary conditions are summarized in the next section.

A.1.6 Boundary Conditions

$BC1, BC2$: The TM is assumed to be clamped by the three rows of OHC HBs at the SM. This gives

$$w^b_{sul}(s = \Delta L_{STS}) = \frac{\partial w^b_{sul}}{\partial s}|_{s=\Delta L_{STS}} = 0 \quad . \tag{A.13}$$

$BC3, BC4$: The TM is assumed to be simply supported at the sulcus limbal attachment. This gives

$$w^b_{sul}(s = -\Delta L_{sul}) = \frac{\partial^2 w^b_{sul}}{\partial s^2}|_{(s=-\Delta L_{sul})} = 0 \quad . \tag{A.14}$$

$BC5, BC6, BC7, BC8$: Displacement, slope, moment and shear force continuity at the boundary between Γ_{B1} and Γ_{B2}.

$BC9$: Thin film lubrication theory is assumed to hold in the gap between neighboring OHC HBs along with no-slip boundary condition at the solid fluid interfaces (see Fig. A.4). From [74] and [7] the velocity in the gap between two neighboring OHCs ($v_{OHC,gap}$) is given by

$$v_{OHC,gap}(s,x,z) = \frac{1}{i\omega\rho_f}\frac{\partial p_{OHC,gap}}{\partial s}\left(1 - \frac{\sinh(\beta(d/2-x)) + \sinh(\beta(d/2+x))}{\sinh(\beta d)}\right) \tag{A.15}$$
$$-\frac{i\omega z}{g_0}\left(\frac{\sinh(\beta(d/2-x)) + \sinh(\beta(d/2+x))}{\sinh(\beta d)}\right)u_{TMS},$$

and the volume flow rate in the gap between two neighboring OHCs ($\dot{Q}_{OHC,gap}$) is given by

$$\dot{Q}_{OHC,gap}(s) = \frac{1}{i\omega\rho_f}\frac{\partial p_{OHC,gap}}{\partial s}\frac{\beta^2 g_0 d(s)^3}{12} - \frac{i\omega d(s) g_0}{2}u_{TMS}, \tag{A.16}$$

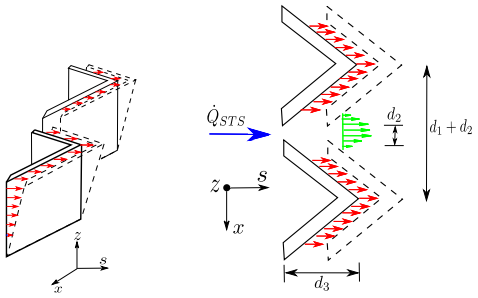

Figure A.4

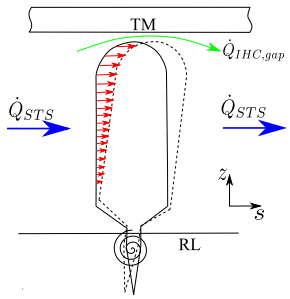

Figure A.5

Figure A.6: The boundary conditions at the sulcus and scala media end of the STS fluid. Then film lubrication theory is assumed to hold in the fluid space between the space between neighboring OHC HBs, and the TM and the apical surface of the IHC HB. (a) The volume flow rate in the radial (s) direction in the STS, $\dot{Q}_{STS}(s = \Delta L_{STS})$ (blue arrows), is equal to the volume of fluid displaced by the OHC HB (red arrows) and the volume flow rate of fluid through the space between neighboring OHC HBs, $\dot{Q}_{OHC,gap}$ (green arrows). Integration of the radial pressure drop in the OHC HB gap yields a Robin boundary condition at the scala media end of the STS, as discussed in $BC9$. (b) The volume flow rate in the radial (s) direction in the STS, $\dot{Q}_{STS}(s = 0)$ (blue arrows), is equal to the volume of fluid displaced by the IHC HB (red arrows) and the volume flow rate of fluid through the TM-HB space, $\dot{Q}_{IHC,gap}$ (green arrow). Integration of the radial pressure drop in the TM-HB space yields a Robin boundary condition at the sulcus end of the STS, as discussed in $BC10$.

where $p_{OHC,gap}$ is the pressure in the gap and $d(s) = d_2 + \frac{d_1}{d_3}(s - \Delta L_{STS})$. d_1, d_2 and d_3 are parameters describing the shape of the OHC HBs and are shown in Fig. A.4. In this study, $d_1 = 8$ µm, $d_2 = 2$ µm and $d_3 = 5$ µm. The flow rate of the fluid flowing through the sub-tectorial space ($\dot{Q}_{STS}$) is equal to the volume displaced by the radial shear of the OHC HBs ($-i\omega\frac{g_0 d_1}{2}u_{TMS}$), and the flow rate in the gap between the OHC HBs ($\dot{Q}_{OHC,gap}$),

$$(d_1 + d_2)\dot{Q}_{STS}(s = \Delta L_{sts}) = \dot{Q}_{OHC,gap} - i\omega\frac{g_0 d_1}{2}u_{TMS}. \tag{A.17}$$

Fig. A.4 shows the different flow rates in the STS and the OHC HBs. Substituting Eq. A.5 and Eq. A.16 in Eq. A.17 and integrating across the OHC HB gap yields a Robin boundary condition for the pressure at the scala media end of the STS.

$BC10$: Thin film lubrication theory is assumed to hold in the gap between the TM and the tip of the IHC HBs along with no-slip boundary condition at the solid fluid interfaces . Similar to the derivation of the OHC boundary conditions, the velocity of the fluid in the gap ($v_{IHC,gap}$) is given by

$$\begin{aligned} v_{IHC,gap}(s,z) = \frac{1}{i\omega\rho_f}\frac{\partial p_{IHC,gap}}{\partial s}\left(1 - \frac{\sinh(\beta(g_0 - z)) + \sinh(\beta(z - \tilde{h}(s)))}{\sinh(\beta(g_0 - \tilde{h}(s)))}\right) \\ -i\omega\left(\frac{\sinh(\beta(g_0 - z))}{\sinh(\beta(g_0 - \tilde{h}(s)))}\right)u_{HB} - i\omega\left(\frac{\sinh(\beta(z - \tilde{h}(s)))}{\sinh(\beta(g_0 - \tilde{h}(s)))}\right)u_{TMS}, \end{aligned} \tag{A.18}$$

where $p_{IHC,gap}$ is the pressure in the gap between the TM and the HB, and $\tilde{h}(s)$ is the local height of the HB given by $\tilde{h}(s) = h + \sqrt{r_{HB}^2 - s^2}$. The volume flow

rate through the gap between the tip of the HB and the TM can be written as

$$\dot{Q}_{IHC,gap}(s) = \frac{1}{i\omega\rho_f}\frac{\partial p_{IHC,gap}}{\partial s}\frac{\beta^2(g_0 - \tilde{h}(s))^3}{12} - i\omega\frac{g_0 - \tilde{h}(s)}{2}(u_{TMS} + u_{HB}). \tag{A.19}$$

The volume of the fluid flowing through the sub-tectorial space ($\dot{Q}_{STS}$) is equal to the volume of fluid displaced by the radial shear of the IHC HBs ($-i\omega\frac{hu_{HB}}{2}$), and the volume of fluid flowing through the gap in the TM-IHC, $\dot{Q}_{IHC,gap}$,

$$\dot{Q}_{STS}(s=0) = \dot{Q}_{IHC,gap} - i\omega\frac{h}{2}u_{HB}. \tag{A.20}$$

Fig. A.5 shows the different flow rates in the IHC HB-TM gap. Substituting Eq. A.5 and Eq. A.19 in Eq. A.20 and integrating radially in the gap around the tip of the IHC HB from $s = -r_{HB}$ to $s = r_{HB}$ yields a Robin boundary condition for the pressure at the sulcus end of the STS, which depends on the curvature of the IHC HB tip (r_{HB}).

A.1.7 System Dynamics

Eq. A.10 and Eq. A.11, along with Eq. A.6, Eq. A.7 and Eq. A.4, and the boundary conditions $BC1$ through $BC10$, leads to the closure of the problem. The whole system can be written in the matrix form as

$$\boldsymbol{M}\begin{pmatrix} \boldsymbol{\zeta} \\ \boldsymbol{\psi} \\ u_{TMS} \\ u_{HB} \\ p_{sul} \end{pmatrix} = \boldsymbol{V} \Rightarrow \begin{pmatrix} \boldsymbol{\zeta} \\ \boldsymbol{\psi} \\ u_{TMS} \\ u_{HB} \\ p_{sul} \end{pmatrix} = \boldsymbol{M}^{-1}\boldsymbol{V}, \tag{A.21}$$

where $\boldsymbol{M} \in \mathbb{C}^{13\times13}$ is the system matrix, and $\boldsymbol{V} \in \mathbb{C}^{13\times1}$ contains the forcing

terms. From Cramer's rule, the effective HB tip transfer function is calculated as

$$\chi = \frac{\det(\boldsymbol{M_{HB}})}{\det(\boldsymbol{M})}, \tag{A.22}$$

where $\boldsymbol{M_{HB}}$ is formed by replacing the column of $\boldsymbol{M}$ corresponding to u_{HB} with $\boldsymbol{F_{HB}} \in \mathbb{Z}^{13\times 1}$, where

$$\boldsymbol{F_{HB}}(i) = \begin{cases} 1, & \text{if } i = 12 \\ 0, & \text{otherwise} \end{cases}. \tag{A.23}$$

The HB tip impedence can be derived as

$$Z_{HB} = \frac{1}{-i\omega\chi}, \tag{A.24}$$

The real part of the HB impedence gives the effective resistance on the system, which is given by

$$R_{tot} = \mathrm{Re}(Z_{HB}). \tag{A.25}$$

A.1.8 Noise and Sensitivity

The PSD of the total noise force on the HB is given by the one-sided power spectrum

$$S_F(\omega) = 4k_BTR_{tot}, \tag{A.26}$$

where k_BT is the Boltzmann energy.

The MET channel opening probability, is given by [57]

$$P(u_{HB}) = \frac{1}{1 + e^{-\frac{(u_{HB} - u^0_{HB})}{\delta}}}, \tag{A.27}$$

where $\delta = \frac{k_BT}{k_{gs}d\gamma_{HB}}$, $k_{gs}d$ is the single channel gating force, γ_{HB} is the geometrical gain and u^0_{HB} is the position of the HB corresponding to a channel open probability of 0.5.

The noise in the channels due to stochastic gating gives rise to a fluctuation of the gating force. The auto-correlation of the channel gating force in the tip link can be written as [95]

$$< F(\tau)|F(0) >= Nk_{gs}^2 d^2 \gamma_{HB}^2 P(1-P) e^{\frac{-|\tau|}{\tau_c}}, \tag{A.28}$$

where τ_c is the channel correlation time. The τ_c has an upper bound set by the CF of the location of the cochlea. The PSD of the channel gating force is given by

$$S_{F_{ch}}(\omega) = Nk_{gs}^2 d^2 \gamma_{HB}^2 P(1-P) \frac{4\tau_c}{(1+\omega^2\tau_c^2)}, \tag{A.29}$$

such that

$$\frac{1}{2\pi} \int_0^\infty S_{F_{ch}}(\omega) d\omega = Nk_{gs}^2 d^2 \gamma_{HB}^2 P(1-P). \tag{A.30}$$

The effective channel resistance for the whole bundle is given by

$$R_{ch}(\omega) = \frac{Nk_{gs}^2 d^2 \gamma_{HB}^2 P(1-P)\tau_c}{k_B T(1+\omega^2\tau_c^2)}. \tag{A.31}$$

The resistance at low freq ($\omega \to 0$) is given by $R_{ch}^0 = \frac{Nk_{gs}^2 d^2 \gamma_{HB}^2 P(1-P)\tau_c}{k_B T}$ [95]. The channel correlation time τ_c in the two state model is given by [9]

$$\tau_c = \frac{\tau_{0.5}}{\cosh(\frac{k_{gs} d}{k_B T}\Delta x)}, \tag{A.32}$$

where Δx is the equilibrium channel extension and $\tau_{0.5}$ is the activation time when $P = 0.5$. In this study, τ_c has been set to $\frac{1}{10CF}$.

From A.26 and A.29, the viscous contribution of the noise can be extracted as

$$R_{visc} = \frac{S_F - S_{F_{ch}}}{4k_B T}. \tag{A.33}$$

The sensitivity of the IHC HB (u_{HB}) and the TM radial motion (u_{TMS}) to a radial

force F_{TMS} applied at the outer edge of the TM are given by

$$H^{HB}_{F_{TMS}} = \frac{u_{HB}}{F_{TMS}},\ H^{TMS}_{F_{TMS}} = \frac{u_{TMS}}{F_{TMS}}.$$

The sensitivity of the IHC HB to the TM radial displacement can be defined as

$$H^{HB}_{TMS} = (H^{TMS}_{F_{TMS}})^{-1} H^{HB}_{F_{TMS}}. \tag{A.34}$$

A.2 Active IHC HB

We use the active HB model from [95]. The linearized impedence for an isolated active hair bundle is given by

$$Z_{ihb,act} = \frac{\lambda\Delta}{-i\omega}\left\{\frac{1}{\frac{\bar{k_G}+\bar{k_f}+k_{es}}{\lambda_a} - i\omega}\right\},$$

where,

$$\begin{aligned}
\bar{k_G} &= N k_{gs}\gamma^2_{HB}\left(1 - \frac{k_{gs}d^2}{k_B T(1-i\omega\tau_c)}P(1-P)\right)\\
\bar{k_f} &= \frac{k_{gs}d\gamma^2_{HB}f_{max}SP(1-P)}{k_B T(1-i\omega\tau_c)}\\
\Delta &= \left(\frac{\bar{k_G}+k_{HB}}{\lambda} - i\omega\right)\left(\frac{\bar{k_G}+k_{es}+\bar{k_f}}{\lambda_a} - i\omega\right)\\
&\quad + \left(\frac{\bar{k_G}(\bar{k_G}+\bar{k_f})}{\lambda\lambda_a}\right),
\end{aligned} \tag{A.35}$$

where, S is the calcium feedback parameter, λ is the resistance of the isolated hair bundle, λ_a is the resistance of the adaptation motor, k_{es} is the extention spring and f_{max} is the maximum stall force on the adaptation motor [95]. For $\lambda_a \to \infty$, the adaptation motor is stationary and the resistance of the active hair bundle matches that of the passive hair bundle ($\lambda + R_{ch}$). In this formulation, the noise from the

adaptation motor is absorbed into the hydrodynamic drag. For a generative system, the hydrodynamic drag is reduced by the power generated by the active mechanism, which provides an effective negative damping given by

$$\lambda_{-} = \mathrm{Re}\left(\frac{\bar{k_G}(\bar{k_G}+\bar{k_f})\lambda_a}{-i\omega(\bar{k_G}+\bar{k_f}+k_{es})^2(1-i\frac{\omega}{\omega_a})}\right) \tag{A.36}$$

where $\omega_a = \lambda_a^{-1}(k_{es}+\bar{k_f}+\bar{k_G})$. In this study, $S = 2$, $\lambda_a = 1$ µN m^{-1} s, $k_{es} = 1.05$ mN m^{-1} and $f_{max} = 1$ nN.

A.3 Contribution of HB displacement noise to channel clatter

In the present formulation, we have assumed that the HB fluctuation does not affect the MET channel fluctuations and depend solely on the resting probability of the HB. In this section we shall discuss the rationale behind this assumption. Consider a IHC HB with tip displacement u_{HB} and mean tip displacement $\overline{u_{HB}}$. Due to the viscosity and channel clatter, the hair bundle fluctuation about the mean position with a variance σ_{HB}^2. We assume a Gaussian probability distribution of the tip displacement of the HB about the mean. The probability density of u_{HB} is given by

$$\mathcal{P}_{u_{HB}} = \frac{1}{\sqrt{2\pi}\sigma_{HB}} \exp\left(-\frac{(u_{HB}-\overline{u_{HB}})^2}{2\sigma_{HB}^2}\right). \tag{A.37}$$

If the channel opening probability is quantified by $s \in [0,1]$, such that $s = 0$ refers to channels being closed and $s = 1$ refers to channels being open, the probability of the channel opening, given the hair bundle displacement (u_{HB}) is given by the two state Boltzmann distribution,

$$P(s=1|u_{HB}) = \frac{1}{1+e^{-\left(\frac{u_{HB}}{\delta}\right)}}, \tag{A.38}$$

where $\delta = \frac{k_B T}{k_{gs} d \gamma_{HB}}$. The expectation value of the MET channels being open is given by

$$E[s] = \int_{r=-\infty}^{r=\infty} P(s=1|r)\mathcal{P}_{u_{HB}}(r)dr. \tag{A.39}$$

Assuming that $\sigma_{HB} << \delta$, we can linearize the $P(u_{HB})$ about $u_{HB} = \overline{u_{HB}}$ as

$$\begin{aligned} P(u_{HB}) = P(\overline{u_{HB}}) + \frac{\partial P}{u_{HB}} \mid_{\overline{u_{HB}}} (u_{HB} - \overline{u_{HB}}) \\ + \frac{\partial^2 P}{\partial u_{HB}^2} \mid_{\overline{u_{HB}}} \frac{(u_{HB} - \overline{u_{HB}})^2}{2} + h.o.t. \end{aligned} \tag{A.40}$$

Integrating Eq A.39 with the simplified expression in equation A.40 gives:

$$E[s] = P(\overline{u_{HB}}) + \frac{\partial^2 P}{\partial u_{HB}^2} \mid_{\overline{u_{HB}}} \frac{\sigma_{HB}^2}{2} \tag{A.41}$$

Similarly, the variance of the channel opening ($\sigma_s^2 = E[s^2] - E[s]^2$) is given by

$$\begin{aligned} \sigma_s^2 = & P(\overline{u_{HB}})(1 - P(\overline{u_{HB}})) + \\ & \frac{\partial^2 P}{\partial u_{HB}^2}(1 - 2P(\overline{u_{HB}}) \mid_{\overline{u_{HB}}} \frac{\sigma_{HB}^2}{2} \end{aligned} \tag{A.42}$$

Eq. A.41 and Eq. A.42 can be viewed as a general channel response to HB fluctuation. The contribution of HB fluctuation to the channel fluctuation is negligible to the leading order because $\frac{\partial^2 P}{\partial u_{HB}^2}$ is small at $P = 0.4$. Hence, it is reasonable to assume that the probability distribution of the channels are unaffected by the HB fluctuations.

A.4 Noise calculation

The PSD of the total noise in the displacement spectrum of the hair bundle is given by

$$(u_{HB}^{noise}(\omega))^2 = |\chi(\omega)|^2[S_{F_{ch}} + S_{F_{visc}}] \tag{A.43}$$

where $|\chi(\omega)|$ is the transfer function between the HB displacement and the force acting on the HB. The variance of the HB fluctuation is given by

$$\sigma_{HB}^2 = \frac{1}{2\pi} \int_{\omega=0}^{\omega_{max}} (u_{HB}^{noise}(\omega))^2 d\omega. \tag{A.44}$$

APPENDIX B

B.1 Mathematical Model

To study the multi-scale dynamics of the cochlea, we have modeled the cochlea through a combination of analytical and numerical methods. Each scala duct in the cochlea has been modeled as a tapered prismatic box, and the scalae are connected to each other at the helicotrema , as shown in Fig. B.1A. The Reissner's membrane is assumed to be acoustically transparent and the pressure and velocity fields of the scala media (SM) and the scala vestibuli (SV) are assumed to be continuous across the Reissner's membrane. The fluid in the SV is acoustically coupled to the oval window (OW) and the fluid in the scala tympani (ST) is coupled to the round window (RW). The height of the SV (H_{SV}) and the ST ducts (H_{ST}) are varied from base to apex according to anatomical measurements by [33] under the assumption of constant duct width (W) throughout the cochlea, as shown in Fig. B.2. The basilar membrane (BM) is modeled as a plate with variable width (b) that increases from base to apex, as shown with the red surface in Fig. B.1A. The BM is coupled to SV and ST fluid on either surface, and is pinned at the medial and lateral edge as shown in Fig. B.1B.

The governing equation for the fluid pressure (p) in the SV and the ST is given by the compressible Helmholtz equation,

$$\nabla^2 p + \left(\frac{\omega}{c}\right)^2 p = 0, \tag{B.1}$$

subject to the boundary condition at the fluid-structure interface given by

$$-\frac{\partial p}{\partial n} + \frac{1}{\gamma}\nabla_s^2 p = \frac{1}{\alpha}\rho_f \omega^2 u_s, \tag{B.2}$$

where n is the local coordinate normal to the fluid-structure interface, ω is the angular frequency, c is the speed of sound in water, μ is the dynamic viscosity, $\gamma^2 = j\omega\rho_f/\mu$, $\alpha = 1 + \frac{4j\mu\omega}{3\rho_f c^2}$, and u_s represents the normal displacement of the surface at the fluid interface. ∇_s^2 is the in-plane 2-D Laplacian defined as $\frac{\partial^2}{\partial x^2} + \frac{\partial^2}{\partial y^2}$. The effect of fluid viscosity is included through the second term in B.2. A detailed study on the application of the asymptotic method for modeling viscous fluid structure interaction is given in [13].

To reduce the computational cost associated with a 3D finite element mesh in the fluid domain, the pressure distribution in the ducts is decomposed into M orthogonal modes in the radial (y) direction that satisfy the boundary conditions at the walls as

$$p(x, y, z) = \sum_{m=0}^{M-1} p_m(x, z) \cos\left(\frac{m\pi(y + W/2)}{W}\right), \quad -0.5W \leq y \leq 0.5W \tag{B.3}$$

where W is the width of the duct as shown in Fig. B.1A and the walls of the duct are at $y = \pm W/2$. In this study, we use three fluid modes, $m = 0, 2, 4$ to approximate the pressure field in the y direction. Symmetry of the model about the x–z plane ensures that the odd fluid modes are not relevant. Substituting Eq. B.3 in Eq. B.1, and invoking the orthogonality of the fluid modes leads to the reduction of the equation

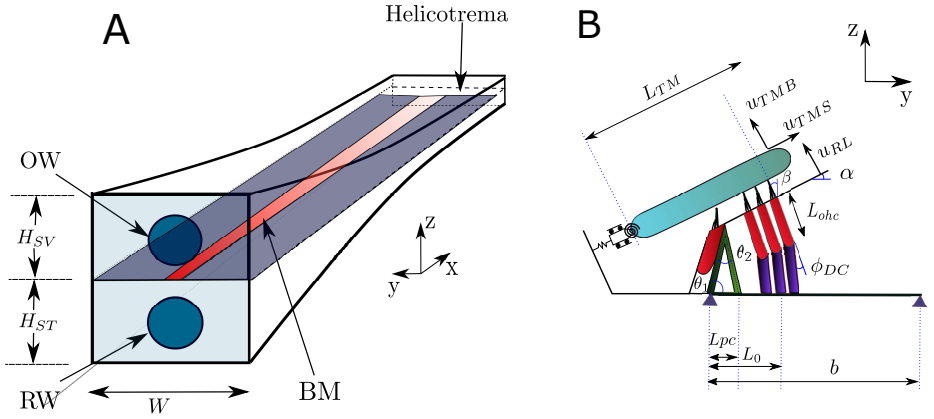

Figure B.1: Schematic of the cochlea in the finite element model. The round window (RW) and oval window (OW) are coupled to the fluid in the scala tympani (ST) and the scala vestibuli (SV) respectively as shown in *A*. The SV and the ST are modeled as tapered ducts connected at the helicotrema. The geometry helicotrema has been simplified in our model as a rectangular slit, although the actual geometry of the helicotrema in the cochlea is more complex. The width of the BM (b) increases from base to apex as shown in *A*. The cross-section of the organ of Corti is shown in *B*. The OHCs are inclined at an angle α with the BM, and are perpendicular to the RL. The DCs connect the base of the OHCs to the BM and are inclined at an angle ϕ_{DC} with the axis of the OHC. The dimensions of the different parts of the organ of Corti vary from base to apex, as tabulated in Tab. B.1.

governing the pressure distribution in the fluid domain to two dimensions as,

$$\frac{\partial^2 p_m(x,z)}{\partial x^2} + \frac{\partial^2 p_m(x,z)}{\partial z^2} + \left[\left(\frac{\omega}{c}\right)^2 - \left(\frac{m\pi}{W}\right)^2\right] p_m(x,z) = 0. \tag{B.4}$$

The BM is modeled as an orthotropic plate [79]. The governing equation for the BM motion is given by [90]

$$\begin{aligned} P_{bm}^{ext}(x,y) =& \frac{2}{b(x)} C_{bm}\dot{u}_{bm}(x,y) + M_{bm}\ddot{u}_{bm}(x,y) - \frac{\partial^2}{\partial x^2}\left(D_{xx}u_{bm}(x,y)\frac{\partial^2 u_{bm}(x,y)}{\partial x^2}\right. \\ &\left. + D_{xy}u_{bm}(x,y)\frac{\partial^2 u_{bm}(x,y)}{\partial y^2}\right) - 2\frac{\partial^2}{\partial x \partial y}\left(D_s \frac{\partial^2 u_{bm}(x,y)}{\partial x^{\partial} y}\right) \\ &+ \frac{\partial^2}{\partial y^2}\left(D_{yy}\frac{\partial^2 u_{bm}(x,y)}{\partial y^2} - D_{xy}\frac{\partial^2 u_{bm}(x,y)}{\partial x^2}\right), \end{aligned} \tag{B.5}$$

where P_{bm}^{ext} is the net external pressure distribution on the BM from the fluid and the OHCs, and D_{xx},D_{xy},D_s and D_{yy} are orthotropic plate stiffnesses. The BM has been

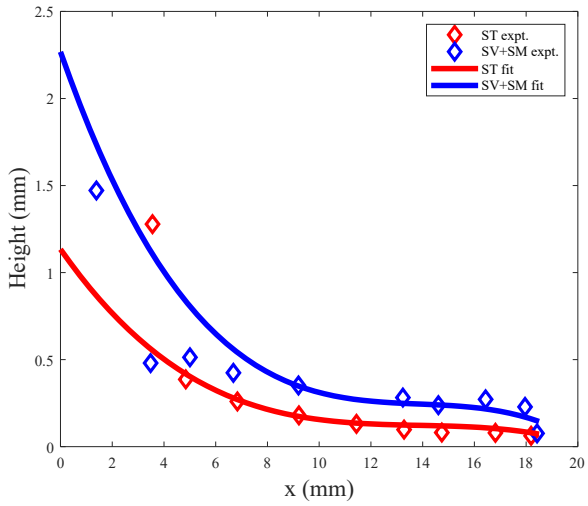

Figure B.2: The height of the scala tympani (ST) and the combined height of scala vestibuli and scala media (SV+SM) in the guinea pig cochlea. The symbols show the height of the scalae ducts derived from experimental measurements of the scalae areas from [33] under the assumption of constant duct width of 1 mm. The solid lines show the smooth theoretical fit of the data used in the model. The theoretical fit of the ST height in the hook region is less than the height seen in experiments. This was required in the model to avoid reflections due to the abrupt change in height.

assumed to vibrate with the mode shape corresponding to the first vibrational mode of a plate under pinned-pinned boundary condition in the radial direction given by

$$u_{bm}(x,y) = u_{bm}(x)\sin\left(\frac{\pi(y+0.5b(x))}{b(x)}\right), \quad -0.5b(x) \le y \le 0.5b(x) \tag{B.6}$$

where $b(x)$ is the width of the BM at distance x from the stapes.

The TM is modeled as a two degree of freedom system with elastic deformations in the radial (y) and transverse direction (z), and is longitudinally coupled through elastic stiffness and shear viscosity. The governing equation of the TM can be written as [90]

$$F_{tm}^{ext} = K_{tms}u_{tms} + C_{tms}\dot{u}_{tms} + M_{tms}\ddot{u}_{tms} + \frac{\partial}{\partial x}\left(A_{tm}G_{tm}\frac{\partial u_{tms}}{\partial x} + A_{tm}\eta_{tm}\frac{\partial \dot{u}_{tms}}{\partial x}\right), \tag{B.7}$$

where F_{tm}^{ext} is the total force on the TM in the radial direction by the OHC HBs.

The kinematics and dynamics of the organ of Corti is derived through a Lagrangian formulation as in [114]. The phalangeal processes are modeled as viscoelastic elements connecting the BM to the RL at a more apical location.

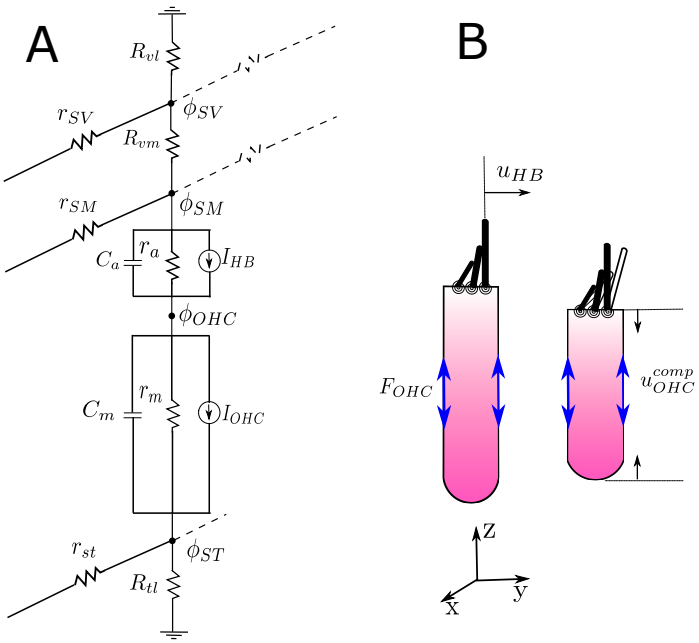

Figure B.3: Model of the electrical cables and hair cell circuit. The schematic of the longitudinal and cross-sectional electrical circuit is shown in (A). The longitudinal cables in the SV, SM and ST connect the different cross-sections of the cochlea. The apical impedence of the hair cell is composed of the apical capacitance (C_a) and resistance (r_a), and the basal impedence of the OHC is composed of the basolateral capacitance (C_m) and the basolateral resistance (r_m). The current conducted by the MET channels (I_{HB}) depends nonlinearly on the deflection of the stereocilia (u_{HB}). The transmembrane potential $(\phi_{OHC} - \phi_{ST})$ produces conformational changes in the basolateral membrane of the OHC, leading to its contraction as schematically shown in (B).

The current flow in the scalae is modeled using cable theory. The electrical potentials in the SV, SM, OHC, and ST are given by ϕ_{SV}, ϕ_{SM}, ϕ_{OHC}, and ϕ_{ST} respectively. The schematic of the electrical circuit is shown in Fig. B.3. The governing equations

are given by

$$\frac{1}{r_{SV}}\frac{\partial^2\phi_{SV}}{\partial x^2} - \left(\frac{1}{R_{vl}} + \frac{1}{R_{vm}}\right)\phi_{SV} + \frac{1}{R_{sm}}\phi_{SM} = 0, \tag{B.8}$$

$$\frac{1}{R_{sm}}\phi_{SV} + \frac{1}{r_{sm}}\frac{\partial^2\phi_{SM}}{\partial x^2} - \left(\frac{1}{R_{sm}} + 3Y_a\right)\phi_{SM} + 3Y_a\phi_{OHC} - I_{HB} = 0, \tag{B.9}$$

$$3Y_a\phi_{SM} - 3\left(Y_a + Y_m\right)\phi_{OHC} + 3Y_m\phi_{ST} + I_{HB} - I_{OHC} = 0, \tag{B.10}$$

$$3Y_m\phi_{OHC} + \frac{1}{r_{st}}\frac{\partial^2\phi_{ST}}{\partial x^2} - \left(\frac{1}{R_{tl}} + 3Y_m\right)\phi_{ST} + I_{OHC} = 0, \tag{B.11}$$

where Y_a and Y_m are admittances at the apical and basal surface of the OHC, respectively. I_{HB} is the current passing through the MET channels in the HBs and is given by

$$I_{HB} = \Delta\phi G_0 \frac{P_{rest}(1 - P_{rest})}{\delta_{HB}} \sum_{j}^{3} u_{HB,j} \tag{B.12}$$

where G_0 is the maximum MET conductance, $\Delta\phi$ is the potential across the apical surface of the hair cell, $u_{HB,i}$ is the HB deflection of the hair bundle of the i^{th} OHC, u^0_{HB} is the resting displacement of the HB, P_{rest} is the resting MET channel opening probability, and δ_{HB} is the MET channel width. Model calculations show that the peak MET current is around 300 pA per nanometer of BM displacement at 4mm from the stapes. I_{OHC} is the current due to the piezo action of the basolateral membrane of the OHCs, given by

$$I_{OHC} = -\sum_{j=1}^{3} \epsilon_3 \dot{u}^{comp}_{OHC,j}, \tag{B.13}$$

where $u^{comp}_{OHC,j}$ is the total inward compression of the j^{th} OHC, ϵ_3 is the piezoelectric constant and Z_m is the basolateral impedence. The force transduced by the j^{th} OHC

is given by

$$F_{OHC,j} = K_{OHC} u^{comp}_{OHC,j} + \epsilon_3 \Big(\phi_{OHC} - \phi_{ST} \Big), \tag{B.14}$$

where K_{OHC} is the OHC axial stiffness.

The finite element dynamic stiffness matrix can be written as [114]

$$\begin{bmatrix} K_f & Q_{fs} & 0 \\ Q_{sf} & K_s & Q_{se} \\ 0 & Q_{es} & K_e \end{bmatrix} \begin{pmatrix} \mathbf{p} \\ \mathbf{u} \\ \boldsymbol{\phi} \end{pmatrix} = \begin{pmatrix} \mathbf{f_p} \\ \mathbf{f_u} \\ \mathbf{f_e} \end{pmatrix}, \tag{B.15}$$

where $[\mathbf{p}]$ is the vector containing all the pressure nodes of the fluid, $[\mathbf{u}]$ is a vector containing the structural nodes and $[\boldsymbol{\phi}]$ is a vector containing all the electrical nodes. K_f, K_s, and K_e are the dynamic stiffness of the fluid, structural and electrical domains, respectively. Q_{fs} and Q_{sf} are the coupling matrices for the fluid-structure interactions, and Q_{se} and Q_{es} are the coupling matrices for the electrical-structure interactions. The $\mathbf{f_p}$, $\mathbf{f_s}$, and $\mathbf{f_e}$ represent the forcing due to the natural boundary conditions on the fluid, structural, and electrical nodes, respectively. The finite element formalism was developed and solved using custom code written in Matlab and C++. The entire geometry was meshed using linear (bi-linear) shape functions for first (second) order PDEs (see [114]), and Hermite shape functions for the BM plate equations (see [87]). Mesh convergence studies were performed and 1000 nodes in the x direction and 42 nodes in the z direction were found to be optimal. A complete set of parameters is given in Tables B.1 through B.3. The model geometry of the organ of Corti at the base and apex is shown in Fig. B.4.

Table B.1: Dimensions used in the model (SI units)

(see schematic in Fig. B.1B)

Property	Description	Value	Source
L	Length of cochlea	18.5×10^{-3}m	[33]
L_h	Length of helicotrema	0.5×10^{-3}m	[33]
b	BM width	$(80 + 100x/L) \times 10^{-6}$m	[33]
L_{TM}	TM length	$(-460000x^2 + 11000x + 82) \times 10^{-6}$ m	[149]
L_{pc}		$0.32b$	[149]
L_0		$0.5b$	[149]
L_{ohc}	OHC length	$(15 + 2000x) \times 10^{-6}$ m	[65]
θ_{php}	PhP tilt angle with BM	60^o	based on [160]
θ_1	IPC-BM angle	$66°$	[149]
θ_2	IPC-OPC angle	$(490x + 60)°$	[149]
ϕ_{DC}		$(5 + 29.9x/L)°$	
L_{st}	Stereocilia length	$(1 + 5x/L) \times 10^{-6}$	[77]
α	RL tilt angle	$(5.3 + 29.6x/L)°$	[149], [65]
β	HB angle	$\alpha + (9^{x/L} - 1)°$	
H_{SV}	Height of SV duct	$(-724.70x^3 + 30.17x^2 - 0.4249x + .002268)$m , $x <$ 14mm from stapes	
		244×10^{-6}m , 14mm$< x <$ 18.5mm	
		$244 \times 10^{-6} \sqrt{1 - \left(\frac{x-L}{0.0276L}\right)^2}$m, $x >$ 18.5mm	Fit from [33]
H_{ST}	Height of ST duct	$0.5H_{SV}$	Fit from [33]

B.2 Predicting ANF FTC from mechanical tuning

Detailed models of the fluid structure interaction in the sub-tectorial space has shown that the radial motion of the TM with respect to the RL ($u_{TMS/RL}$) drives the deflection of the IHC HB by coupling the viscous fluid between the lower surface of the TM with the IHC HB [38, 111, 129]. The transfer function between the TM radial displacement and the IHC HB tip displacement IHC HB is a high pass filter

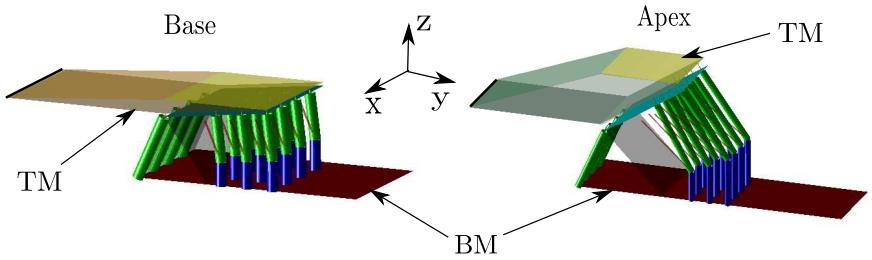

Figure B.4: The geometry of the organ of Corti at basal (1 mm from stapes) and apical (18 mm from stapes) locations generated from the parameters listed in Tab. B.1. Notice that the angle between the RL and the BM (α in Fig. B.1B) is larger at the apex than at the base. Further, the angle between the OHC and the DC axes (ϕ_{DC} in Fig. B.1B) increases from base to apex.

($F_1(f)$) of the form

$$F_1(f) = \frac{-i(f/f_{c1})}{1 - i(f/f_{c1})}, \tag{B.16}$$

where f is the frequency and f_{c1} is the corner frequency of the high pass filter. Here, we have assumed a $f_{c1} = 100$ Hz [131]. Further, adaptation in mammalian hair bundles leads to a high pass filtering of the MET current [121, 34, 105, 1] and consequently the ANF excitation spectrum. This is included with a second high pass filter $F_2(f)$ with corner frequency $f_{c2} = 600$ Hz (equivalently a time constant of 1.7 ms) consistent with measurements from experiments ([105]). The complete transfer function is given by

$$F(f) = F_1(f)F_2(f), \tag{B.17}$$

ans the ANF excitation (E) is given by

$$E(f) = F(f)u_{TMS/RL}(f). \tag{B.18}$$

Table B.2: Dynamical parameters used in the model (SI units)

Property	Value in SI	Source
K_{bm}	$2.16e^{-380x} \times 10^5$ Pa	[79]
K_{st}	$1.2e^{-380x} \times 10^4$ Pa	[145]
K_{tms}	$2.4e^{-380x} \times 10^4$ Pa	[122]
K_{tmb}	$1e^{-380x} \times 10^3$ Pa	Based on [164]
K_{rl}	$5.4e^{-380x} \times 10^3$ Pa	[22]
K_{ohc}	$2.7e^{-380x} \times 10^3$ Pa	[49]
K_{php}	$4.3e^{-380x} \times 10^3$ Pa	[160]
C_{bm}	0.05 Pa-s	Fit
C_{tms}	0.04 Pa-s	Assumed
C_{tmb}	0.04 Pa-s	Assumed
C_{php}	0.04 Pa-s	Assumed
D_{xx}	$1e^{-100x} \times 10^{-10}$ N-m	[79]
D_{xy}	$1e^{-100x} \times 10^{-10}$ N-m	[79]
D_s	$4.3e^{-100x} \times 10^{-11}$ N-m	[79]
G_{tm}	$1 \times 10^{-20x} \times 10^3$ Pa	[42]
η_{tm}	0.02×10^{-20x} Pa-s	Based on [45]
M_{bm}	$4.2e^{160x} \times 10^{-7}$ Pa-s^2	Fit
M_{tms}	$7e^{160x} \times 10^{-7}$ Pa-s^2	Fit
M_{tmb}	$4e^{160x} \times 10^{-7}$ Pa-s^2	Fit

The normalized threshold ($T(f)$) at the location is given by

$$T(f) = 20 \log_{10} \left| \frac{E_{CF}}{E(f)} \right|, \tag{B.19}$$

where E_{CF} is the ANF excitation at CF. It should be noted that there are additional filters in the IHC as well as nonlinear processes inside the IHC and at the synapse that have been shown to modulate neural tuning [4] influencing factors such as phase locking, but these mechanisms have not been included in our estimate of the input to the auditory nerve. The purpose of this model is to evaluate the first order effects of mechanical tuning on the neural tuning, and in a way, model the electro-mechanical stimulus to the IHC that would serve as the input to the more elaborate IHC and synaptic model presented in [4].

Table B.3: Electrical parameters used in the model (SI units)

Property	Value in SI	Source
R_{tl}	4 Ω-m	Based on [144]
R_{vm}	25 Ω-m	Based on [144]
R_{vl}	10 Ω-m	Based on [144]
$1/R_{a0}$	$1.7e^{-300x} \times 10^{-2}$ $(\Omega\text{-m})^{-1}$	Calculated from [23]
R_{sv}	3×10^6 Ω-m	[144]
R_{sm}	5×10^6 Ω-m	Based on [144]
R_{st}	150×10^6 Ω-m	Based on [144]
$1/R_m$	$2.7e^{-300x} \times 10^{-2}$ $(\Omega\text{-m})^{-1}$	[56, 63]
C_a	50×10^{-9} F	Calculated from [23]
C_m	$300(9 + 12x/L) \times 10^{-9}$F	[56, 63]
ϵ_3	$-0.0104(1 + 10x)$ N(m-V)$^{-1}$	[61]

B.3 Cochlear tuning from base to apex

The CF map or the tonotopic map of the BM obtained from our model is shown in Fig. B.5 with blue symbols and the CF of the threshold ANF FTC is shown with black symbols. The Greenwood map of the CF of multiple locations from different experiments [47] is shown with the solid black line. The exponential place-frequency map fit to the experimental data at the base of the cochlea is shown with a straight dashed line (on the semi-log scale). It is worth noting that the fit from [47] is based on very few data points at the apex, especially within the last five millimeter of the cochlear spiral. The model recreates the breakdown of exponential scaling at the apex and closely follows the fit of the tonotopic map from [47]. The model predicts that the CF of the ANF could deviate from that of the BM because of the additional filters associated with the hair bundle transduction in the organ of Corti (see previous section). Moreover, the geometry of the helicotrema *in vivo* could influence the tuning in a significant way within the apical one millimeter of the cochlea and its effect is not captured by the simplistic geometry of the helicotrema assumed in this model.

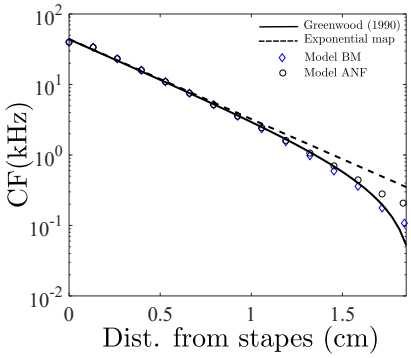

Figure B.5: The tonotopic map of the CF obtained from our model. The blue circles show the CF map of the BM from the model and the black circles show the CF map of the ANF from the model. The solid line shows the fit from [47] and the dashed line shows the exponential fit.

B.4 Effect of location and optical axis on the OoC response phase

The location and direction of the measurements made in experiments of [115] are different from that of the computational model. In this section, we analyze these differences and relate the two quantities for low frequency (below CF) excitation. Fig. B.6 shows a schematic of the organ of Corti vibration in the active (A) and the passive (B) cochlea. In the model, the RL motion is defined to be perpendicular to the original plane of the RL and the absolute motion of this point is identified by a blue arrow in Fig. B.6(A) and (B) and shown in Fig. 4.1 of Chapter IV. The virtual optical axis coincides with this direction as shown in Fig. S9 with blue dotted lines. In the active case (low SPL excitation), the OHC electromotile force acts on the BM and the RL in opposite directions, pulling the RL downward (toward the ST) and the BM upward (toward the SM/SV) under depolarization. At low levels, the RL motion is greater than the BM motion. Consequently, the net RL motion is out of phase with the BM as shown with the blue arrow in Fig.B.6(A), and quantified through model results in Fig. 4.2(D) and Fig 4.4(E–H) in the main text. Hence, the RL is in phase with the stapes (when the stapes moves inward toward the cochlear fluids, the

RL moves upwards) while the BM is out of phase with the stapes. In the absence of somatic motility in the passive model, the OHCs act as passive stiffness members, and the RL moves in phase with the BM.

Recio-Spinoso and Oghalai estimate the experimental measurement location in their preparation to be "near the reticular lamina at the lateral edge of the outer hair cell region or medial edge of the Hensen cells" ([115]). Considering this description and the lateral resolution of the imaging voxel (9.8μm), we assume that the measured signal partially includes contributions from the medial portion of the Hensen cells. Furthermore, the optical axis of the OCT system is not perpendicular to the RL. Rather, as reported in [115], the optical axis is either transverse to the BM or parallel to the central axis of cochlea; using this information, we estimate the axis to be within the two angles shown by the red dotted lines in Fig. B.6. Along this optical axis, the tissue would move outward (positively) upon compression of the OHC (shown with the red measurement point in Fig. B.6(A) and (B)) during upward BM motion. Such compression occurs in both the active (low SPL stimulation) and passive cases, putting the measured motion of this tissue out of phase with the stapes motion and in phase with the BM motion at low frequencies. We hypothesize that this as a mechanism to explain the discrepancy in the sub-CF phase of the active RL between the model results and experiments in Fig. 4.4(E–H) in Chapter IV. This is a testable hypothesis (by directly measuring the vectorial motion of the tissue) that is consistent with the measurements of Ciganović et al. (2018) [14] shown in Fig. SB.6(C). Other as yet unidentified mechanisms may also be responsible.

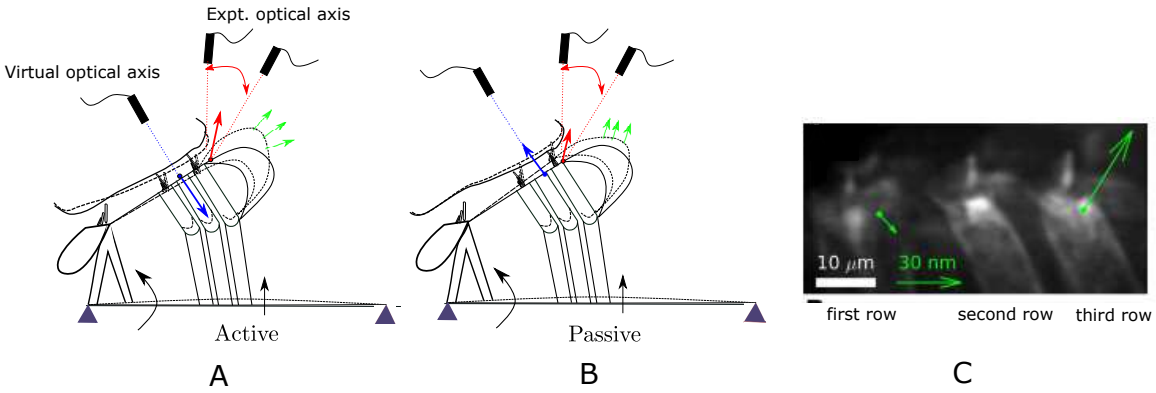

Figure B.6: The effect of different measurement locations and directions on the relative phase between the RL and the BM in the (A) active and the (B) passive cochlea for frequencies below CF. In our theoretical calculations, the displacement of the RL is measured at the second row of the OHCs (shown with the blue circle) perpendicular to the RL, as defined by u_{RL} in the model. (A) In the active model, the net RL motion is downward (as shown by the blue arrow) and out of phase with the BM (black arrow). However, the lateral edge of the third row OHCs and the medial edge of the Hensen cells (location shown with red circle) have been shown to vibrate differently than the RL at the second row of OHC (C) by Ciganović et al.[14]. In experiments, the motion of the second row of the OHC towards the ST (Fig. (C) shorter green arrow) led to the squeezing out of the third row of the OHC and the Hensen cells (Fig. (C) longer green arrow) towards the SV. In our active model (A), if the third row of OHCs and the Hensen cells are squeezed outward (as shown with green arrows in (A)) by the compression of the OHC, this motion, as measured along the experimental optical axis (dashed red lines) would be in phase with the BM and out of phase with the RL at the second OHC. In the passive model (B), the RL and BM move together, but the RL motion is less than the BM motion. Under this condition, the OoC is still squeezed and the Hensen cells move outward and upward as well as being in phase with the BM (as shown with the red circle), just as in the active case. The hair bundles of the second row of the OHCs have been omitted in the schematics in Fig. (A,B) for clarity. Fig. (C) is from Ciganović et al. [14] and was included here under the PLoS creative commons license.

APPENDIX C

C.1 NAM Using Electrodynamical Speakers

We used the Thiele Small parameters for the 1-1/4 inch CE30P-4 Dayton mini speakers to model the NAM system discussed in the main text. The parameters are tabulated in Tab. S1. The transfer function of the velocity of the speaker membrane (V_{sp}) due to voltage applied to the terminals (ϕ) is given by

$$\frac{V_{sp}}{\phi} = \frac{BL}{Z_e Z_m + BL^2}, \tag{C.1}$$

where $Z_e(s) = Ls + R$, $Z_m = ms + k/s + c$ and $s = -i\omega$.

The output of the microphone (of sensitivity $\Gamma = \frac{\phi}{p}$) was amplified through a gain g_d using an acoustic amplifier and supplied to the input terminals of the speaker. The complete transfer function between the velocity of the speaker V_{sp} and the pressure at its corresponding microphone (located at a distance d_{FF} upstream) is given by

$$V_{sp} = G_{sp} p(x - d_{FF}) = \Gamma g_d \frac{BL}{(Z_e Z_m + BL^2)} p(x - d_{FF}). \tag{C.2}$$

Using Eq. C.2, the acoustic source strength $S(x_j)$ can be written in terms of the pressure at the j$^{\text{th}}$ microphone P_p^j as

$$S(x_j) = -i\omega\rho V_{sp}\frac{S_{sp}}{S_{duct}} = G_{sp}P_p^j, \tag{C.3}$$

where $G_{sp} = \Gamma g_d \frac{-iS_{sp}}{S_{duct}} \frac{BL}{Z_e Z_m + BL^2}$, S_{duct} is the cross-sectional area of the duct, and S_{sp} is the area of the speaker diaphragm. Stability calculations (as discussed in Chapter VI) yield a stable discrete gain boundary of $g_d \in (-0.04, 0.088)$.

C.2 Full Wave (FW) Simulations

We performed 3D full wave simulations in Comsol Multiphysics v5.4 using the pressure acoustics module. The schematic of the modeled system is shown in Fig. C.1. We imposed radiation boundary conditions at either end (shaded green) to model the infinite waveguide. The sensors were positioned along the center of the duct, at a distance d_{FF} upstream from its actuator pair (blue circles). A representative sensor-actuator pair is shown in Fig. S3 where the pressure at the cross-section shaded red is fed forward a distance d_{FF} to its actuator (blue circle) through a gain G_{sp}. For the FW model of the system, the actuators are modeled as boundary velocity forcing to replicate the diaphragm of electrodynamical speakers operating in the piston-mode with an average velocity V_{sp} given by Eq. C.2 and the nominal values for microphone and electrodynamical speakers (Tab. C.1) were used calculate the acoustic response. For the ideal actuator assumption (source strength equal to the upstream pressure, $S(x_j) = g_d p_p^j$), the velocity of the j$^{\text{th}}$ actuator was set to be

$$V_{sp} = g_d \frac{S_{duct}}{-iS_{sp}} P_p^j, \tag{C.4}$$

where P_p^j is the pressure at the corresponding upstream probe.

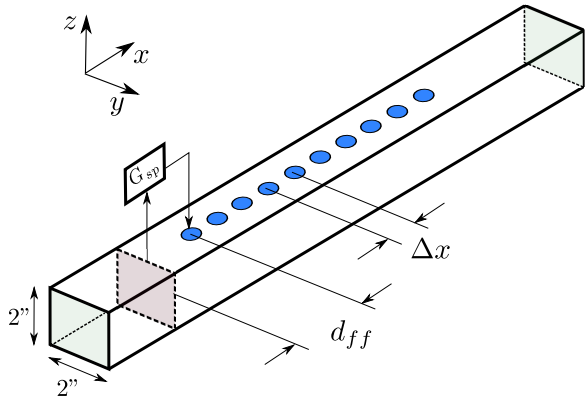

Figure C.1: The schematic of the 3D waveguide as modeled in finite element. The acoustic source strength of the actuator is controlled by the signal from a probe placed at a distance d_{FF} upstream modulated by the gain G_{sp}.

Table C.1: Speaker parameters

Property	Description	Value
BL	Magnetic coupling	1.906 Wb.m^{-1}
ρ	Density of air	1.2 kg.m^{-3}
R	Electrical resistance of speaker	3.508 Ω
L	Electrical inductance of speaker	1.64×10^{-4} H
m	Mass of speaker	6.08×10^{-4} kg
k	Stiffness of speaker	4651.2 N.m^{-1}
c	Damping of speaker	0.486 kg.m^{-1}
Γ	Sensitivity of microphone	0.5 V.Pa^{-1}
S_{duct}	Duct cross-section	26×10^{-4} m^2
$S_{speaker}$	Effective diaphragm cross-section	3.1416×10^{-4} m^2

BIBLIOGRAPHY

BIBLIOGRAPHY

[1] Stauffer. Eric A. and Holt Jeffrey H. Sensory transduction and adaptation in inner and outer hair cells of the mouse auditory system. *Journal of Neurophysiology*, 98:3360–3369, 2007.

[2] Luca Airoldi and Massimo Ruzzene. Design of tunable acoustic metamaterials through periodic arrays of resonant shunted piezos. *New Journal of Physics*, 2011.

[3] Jont B. Allen. Cochlear micromechanicsA physical model of transduction. *The Journal of the Acoustical Society of America*, 68(6):1660, 1980.

[4] Allesandro Altoè, Ville Pulkki, and Sarah Verhulst. The effects of the activation of the inner-hair-cell basolateral K^+ channels on auditory nerve responses. *Hearing Research*, 364:68–80, 2018.

[5] M. H. Ansari, M. A. Attarzadeh, M. Nouh, and M. Amin Karami. Application of magnetoelastic materials in spatiotemporally modulated phononic crystals for nonreciprocal wave propagation. *Smart Materials and Structures*, 2018.

[6] Bertram A. Auld. *Acoustic fields and waves in solids*. 1975.

[7] W. M. Beltman, P. J. M. Van Der Hoogt, R. M. E. J. Spiering, and Tijdeman. Implementation and experimental validation of a new viscothermal acoustic finite element for acousto-elastic problems. *Journal of Sound and Vibration*, 216(1):159–185, 1998.

[8] Andrea E. Bergamini, Manuel Zündel, Edgar A. Flores Parra, Tommaso Delpero, Massimo Ruzzene, and Paolo Ermanni. Hybrid dispersive media with controllable wave propagation: A new take on smart materials. *Journal of Applied Physics*, 118(15), 2015.

[9] Volker Bormuth, Jrmie Barral, Jean-Franois Joanny, Frank Jülicher, and Pascal Martin. Transduction channels' gating can control friction on vibrating hair-cell bundles in the ear. *Proceedings of the National Academy of Sciences of the United States of America*, 111(20):7185–90, 5 2014.

[10] Laurel H. Carney, Megean J. McDuffy, and Ilya Shekhter. Frequency glides in the impulse responses of auditory-nerve fibers. *The Journal of the the Acoustical Society of America*, 105:2384–2391, 1999.

[11] Fangyi Chen, Dingjun Zha, Anders Fridberger, Jiefu Zheng, Niloy Choudhury, Steven L Jacques, Ruikang K Wang, Xiaorui Shi, and Alfred L Nuttall. A differentially amplified motion in the ear for near-threshold sound detection. *Nature Neuroscience*, 14(6):770–4, 6 2011.

[12] Yangyang Chen, Xiaopeng Li, Hussein Nassar, Gengkai Hu, and Guoliang Huang. A programmable metasurface for real time control of broadband elastic rays. *Smart Materials and Structures*, 27(11), 2018.

[13] Lei Cheng, Yizeng Li, and Karl Grosh. Including fluid shear viscosity in a structural acoustic finite element model using a scalar fluid representation. *Journal of Computational Physics*, 247:248–261, 8 2013.

[14] Nikola Ciganović, Rebecca L. Warren, Batu Keceli, Anders Fridberger, and Tobias Reichenbach. Static length changes of cochlear outer hair cells can tune low-frequency hearing. *PLoS Computational Biology*, page 1005936, 2018.

[15] M Collet, M Ouisse, M Ichchou, and M Ruzzene. Semi-active optimization of 2D wave's dispersion into mechanical systems by the mean of periodically distributed shunted piezoelectric patches: a new class of adaptive metamaterials. *Behavior And Mechanics Of Multifunctional Materials And Composites 2011*, 2011.

[16] Nigel P. Cooper. Harmonic distortion on the basilar membrane in the basal turn of the guineapig cochlea. *The Journal of Physiology*, 509:277–288, 2004.

[17] Nigel P. Cooper and William S. Rhode. Nonlinear mechanics at the apex of the guinea-pig cochlea. *Hearing Research*, 82(2):225–243, 1995.

[18] Nigel P. Cooper and William S. Rhode. Mechanical responses to two-tone distortion products in the apical and basal turns of the mammalian cochlea. *Journal of Neurophysiology*, 78(1):261–270, 1997.

[19] Nigel P. Cooper, Anna Vavakou, and Marcel van der Heijden. Vibration hotspots reveal longitudinal funneling of sound-evoked motion in the mammalian cochlea. *Nature Communications*, 9, 2018.

[20] Steven A. Cummer, Johan Christensen, and Andrea Alù. Controlling sound with acoustic metamaterials, 2016.

[21] Peter Dallos. LowFrequency Auditory Characteristics: Species Dependence. *The Journal of the Acoustical Society of America*, 1970.

[22] Peter Dallos. Organ of Corti kinematics. *Journal of the Association for Research in Otolaryngology*, 4:416–421, 2003.

[23] Peter Dallos and B.N. Evans. High-frequency motility of outer hair cells and the cochlear amplifier. *Science*, 267:2006–9, 1995.

[24] Peter Dallos, Xudong Wu, Mary Ann Cheatham, Jiangang Gao, Jing Zheng, Charles T. Anderson, Shuping Jia, Xiang Wang, Wendy H.Y. Cheng, Soma Sengupta, David Z.Z. He, and Jian Zuo. Prestin-Based Outer Hair Cell Motility Is Necessary for Mammalian Cochlear Amplification. 2008.

[25] Egbert de Boer. The mechanical waveform of the basilar membrane. I. Frequency modulations (glides) in impulse responses and cross-correlation functions. *The Journal of the the Acoustical Society of America*, 101:3583–3592, 1997.

[26] Egbert de Boer and Alfred L. Nuttall. The mechanical waveform of the basilar membrane. III. Intensity effects. *The Journal of the Acoustical Society of America*, 107(3):1497–1507, 2000.

[27] W. Denk, W. W. Webb, and A James Hudspeth. Mechanical properties of sensory hair bundles are reflected in their Brownian motion measured with a laser differential interferometer. *Proceedings of the National Academy of Sciences of the United States of America*, 86(14):5371–5, 7 1989.

[28] Wei Dong and Nigel P. Cooper. An experimental study into the acoustomechanical effects of invading the cochlea. *Journal of the Royal Society Interface*, 6:561–571, 2006.

[29] Wei Dong and Elizabeth S. Olson. Supporting evidence for reverse cochlear traveling waves. *The Journal of the Acoustical Society of America*, 123(1):222–240, 1 2008.

[30] Wei Dong and Elizabeth S. Olson. Detection of cochlear amplification and its activation. *Biophysical Journal*, 2013.

[31] E. F. Evans. The frequency response and other properties of single fibres in the guineapig cochlear nerve. *The Journal of Physiology*, 1972.

[32] E. Fallah, C. Elliott Strimbu, and Elizabeth S. Olson. Nonlinearity and amplification in cochlear responses to single and multi-tone stimuli. *Hearing Research*, 277:271–281, 2019.

[33] César Fernández. Dimensions of the Cochlea (Guinea Pig). *The Journal of the Acoustical Society of America*, 24(5):519, 1952.

[34] Robert Fettiplace and Anthony J. Ricci. Adaptation in auditory hair cells. *Current Opinion in Neurobiology*, 13:446–51, 2003.

[35] Mario Fleischer, Rolf Schmidt, and Anthony W. Gummer. Compliance profiles derived from a three-dimensional finite-element model of the basilar membrane. *The Journal of the Acoustical Society of America*, 127(5):2973–2991, 2010.

[36] R Fleury, D Sounas, M R Haberman, and A Alu. Nonreciprocal Acoustics. *Acoustics Today*, 2015.

[37] Romain Fleury, Dimitrios L. Sounas, Caleb F. Sieck, Michael R. Haberman, and Andrea Alù. Sound isolation and giant linear nonreciprocity in a compact acoustic circulator. *Science*, 2014.

[38] Dennis M. Freeman and Thomas F. Weiss. Superposition of hydrodynamic forces on a hair bundle. *Hearing Research*, 48(1-2):1–15, 1990.

[39] Anders Fridberger, Igor Tomo, Mats Ulfendahl, and Jacques Boutet de Monvel. Imaging hair cell transduction at the speed of sound: Dynamic behavior of mammalian stereocilia. *Proceedings of the National Academy of Sciences*, 103(6):1918–1923, 2 2006.

[40] Y. C. Fung. *Foundation of Solid Mechanics And Variational methods*. 1965.

[41] Simon S. Gao, Rosalie Wang, Patrick D. Raphael, Yalda Moayedi, Andrew K. Groves, Jian Zuo, Brian E. Applegate, and John S. Oghalai. Vibration of the organ of Corti within the cochlear apex in mice. *Journal of Neurophysiology*, 2014.

[42] Nria Gavara and Richard S Chadwick. Noncontact microrheology at acoustic frequencies using frequency-modulated atomic force microscopy. *Nature Methods*, 7(8):650–654, 2010.

[43] C. Daniel Geisler. *From Sound to Synapse*. Oxford University Press, 1998.

[44] C. Daniel Geisler and Chunning Sang. A cochlear model using feed-forward outer-hair-cell forces, 1995.

[45] Roozbeh Ghaffari, Alexander J Aranyosi, and Dennis M Freeman. Longitudinally propagating traveling waves of the mammalian tectorial membrane. *Proceedings of the National Academy of Sciences of the United States of America*, 104(42):16510–5, 2007.

[46] Vikrant J. Gokhale and Mina Rais-Zadeh. Phonon-electron interactions in piezoelectric semiconductor bulk acoustic wave resonators. *Scientific Reports*, 4, 2014.

[47] Donald D. Greenwood. A cochlear frequencyposition function for several species29 years later. *The Journal of the Acoustical Society of America*, 1990.

[48] Karl Grosh, Jiefu Zheng, Yuan Zou, Egbert de Boer, and Alfred L Nuttall. High-frequency electromotile responses in the cochlea. *The Journal of the Acoustical Society of America*, 115(5):2178–2184, 2004.

[49] David Z.Z. He and Peter Dallos. Properties of voltage-dependent somatic stiffness of cochlear outer hair cells. *Journal of the Association for Research in Otolaryngology*, 1:64–81, 2000.

[50] Wenxuan He, Anders Fridberger, Edward Porsov, and Tianying Ren. Fast Reverse Propagation of Sound in the Living Cochlea. *Biophysical Journal*, 98(11):2497–2505, 6 2010.

[51] Wenxuan He, David Kemp, and Tianying Ren. Timing of the reticular lamina and basilar membrane vibration in living gerbil cochleae. *eLife*, 7, 9 2018.

[52] Wenxuan He and Tuanying Ren. Basilar membrane vibration is not involved in the reverse propagation of otoacoustic emissions. *Scientific Reports*, 3, 2013.

[53] Rickye Heffner, Henry Heffner, and Bruce Masterton. Behavioral Measurements of Absolute and Frequency-Difference Thresholds in Guinea Pig Behavioral Measurements of Absolute and Frequency- Difference Thresholds in Guinea Pig. *J. Acoust. Soc. Am.*, 49:1888–1895, 1971.

[54] Hermann L.F. Helmholtz. *Die Lehre von den Tonempfindungen als physiologische Grundlage fr die Theorie der Musik*. Longmans, Green, and Co., 1875.

[55] Fred S. Hickernell. The piezoelectric semiconductor and acoustoelectronic device development in the sixties, 2005.

[56] Gary D. Housley and Jonathan F. Ashmore. Ionic currents of outer hair cells isolated from the guinea-pig cochlea. *Journal of Physiology*, 448:73–98, 1992.

[57] J. Howard and A.J. J Hudspeth. Compliance of the hair bundle associated with gating of mechanoelectrical transduction channels in the bullfrog's saccular hair cell. *Neuron*, 1(3):189–199, 1988.

[58] Jonathon Howard. *Mechanics of Motor Proteins and the Cytoskeleton*, volume 7. 2001.

[59] Ronald R. Hoy and Daniel Robert. Tympanal hearing in insects. *Annual Review of Entomology*, 41:433–450, 1996.

[60] Thomas J.R. Hughes. *The Finite Element Method: Linear Static and Dynamic Finite Element Analysis*. Dover, 2000.

[61] K H Iwasa. Current noise spectrum and capacitance due to the membrane motor of the outer hair cell: theory. *Biophysical journal*, 73(6):2965–2971, 1997.

[62] Shuping Jia, Peter Dallos, and David Z Z He. Mechanoelectric transduction of adult inner hair cells. *The Journal of neuroscience : the official journal of the Society for Neuroscience*, 27(5):1006–1014, 1 2007.

[63] Stuart L. Johnson, Maryline Beurg, Walter Marcotti, and Robert Fettiplace. Prestin-Driven Cochlear Amplification Is Not Limited by the Outer Hair Cell Membrane Time Constant. *Neuron*, 70(6):1143–1154, 2011.

[64] G. P. Jones, V. A. Lukashkina, I. J. Russell, S. J. Elliott, and A. N. Lukashkin. Frequency-dependent properties of the tectorial membrane facilitate energy transmission and amplification in the cochlea. *Biophysical Journal*, 104(6):1357–1366, 3 2013.

[65] J P Kelly. Morphometry of the apical turn of the guinea pig's cochlea. *Acta Otolaryngol Suppl (Stockh)*, 467:113–122, 1989.

[66] D. T. Kemp. Stimulated acoustic emissions from within the human auditory system. *Journal of the Acoustical Society of America*, 64(5):1386–1391, 1978.

[67] Mead C. Killion and Peter Dallos. Impedance matching by the combined effects of the outer and middle ear. *The Journal of the Acoustical Society of America*, 41:433–450, 1979.

[68] G.S. Kino. *Acoustic Waves: Devices, Imaging, and Analog Signal Processing*. 1987.

[69] Erwin Kreyszig. *Advanced Engineering Mathematics*. Wiley, 1983.

[70] Richard Krimholtz. Equivalent Circuits for Transducers Having Arbitrary Asymmetrical Piezoelectric Excitation. *IEEE Transactions on Sonics and Ultrasonics*, 19(4):427–435, 1972.

[71] Pijush K. Kundu, Ira M. Cohen, and David R. Dowling. *Fluid Mechanics*. 2016.

[72] Hee Y. Lee, Patrick D. Raphael, Anping Xia, Jinkyung Kim, Nicolas Grillet, Brian E. Applegate, Audrey K.E. Bowden, and John S. Oghalai. Two-dimensional cochlear micromechanics measured *in vivo* demonstrate radial tuning within the mouse organ of Corti. *Journal of Neuroscience*, 36:8160–8173, 2016.

[73] Edwin R. Lewis, Eva Hecht-Poinar, Glennis R. Long, Richard F. Lyon, and Peter M. Narins, editors. *Diversity in Auditory Mechanics*. World Scientific, 1997.

[74] Yizeng Li. Micro and Macro Fluidic Effects in Cochlear. 2013.

[75] Yizeng Li and Karl Grosh. Direction of wave propagation in the cochlea for internally excited basilar membrane. *The Journal of the Acoustical Society of America*, 131(6):4710–4721, 6 2012.

[76] Yizeng Li and Karl Grosh. The Coda of the Transient Response in a Sensitive Cochlea: A Computational Modeling Study. *PLOS Computational Biology*, 12(7):e1005015, 7 2016.

[77] David J Lim. Cochlear anatomy related to cochlear micromechanics. A review. *The Journal of the Acoustical Society of America*, 67, 1980.

[78] Kian-Meng Lim and Charles R. Steele. A three-dimensional nonlinear active cochlear model analyzed by the WKB-numeric method. *Hearing Research*, 170(1-2):190–205, 8 2002.

[79] Shuangqin Liu and Robert D White. Orthotropic material properties of the gerbil basilar membrane. *The Journal of the Acoustical Society of America*, 2008.

[80] Yi-Wen Liu and Stephen T. Neely. Distortion product emissions from a cochlear model with nonlinear mechanoelectrical transduction in outer hair cells. *The Journal of the the Acoustical Society of America*, 127:2420–2432, 2010.

[81] Enrique A Lopez-Poveda and Almudena Eustaquio-Martín. A Biophysical Model of the Inner Hair Cell: The Contribution of Potassium Currents to Peripheral Auditory Compression. *JARO - Journal of the Association for Research in Otolaryngology*, 7:218–235, 2006.

[82] Andrei N Lukashkin and Ian J Russell. A second, low-frequency mode of vibration in the intact mammalian cochlea. *The Journal of the Acoustical Society of America*, 113(3):1544–1550, 2003.

[83] LM Lyamshev. A question in connection with the principle of reciprocity in acoustics. *Soviet Physics Doklady*, 4:406–409, 1959.

[84] Martin Maldovan. Sound and heat revolutions in phononics.

[85] F Mammano and R Nobili. Biophysics of the cochlea: Linear approximation. *J. Acoust. Soc. Am.*, 93(6):3320–3332, 6 1993.

[86] Daphne Manoussaki, Richard S Chadwick, Darlene R Ketten, Julie Arruda, Emilios K Dimitriadis, and Jen T O'Malley. The influence of cochlear shape on low-frequency hearing. *Proceedings of the National Academy of Sciences of the United States of America*, 105(16):6162–6, 4 2008.

[87] Julien Meaud and Karl Grosh. The effect of tectorial membrane and basilar membrane longitudinal coupling in cochlear mechanics. *The Journal of the Acoustical Society of America*, 127(3):1411–1421, 3 2010.

[88] Julien Meaud and Karl Grosh. Coupling active hair bundle mechanics, fast adaptation, and somatic motility in a cochlear model. *Biophysical Journal*, 100(11):2576–2585, 6 2011.

[89] Julien Meaud and Karl Grosh. Response to a Pure Tone in a Nonlinear Mechanical-Electrical-Acoustical Model of the Cochlea. *Biophysical Journal*, 102(6):1237–1246, 3 2012.

[90] Julien Meaud and Karl Grosh. Effect of the Attachment of the Tectorial Membrane on Cochlear Micromechanics and Two-Tone Suppression. *Biophysical Journal*, 106(6):1398–1405, 2014.

[91] Julien Meaud and Charlsie Lemons. Nonlinear response to a click in a time-domain model of the mammalian ear. *The Journal of the Acoustical Society of America*, 138(1):193–207, 7 2015.

[92] George A. Misrahy, Kenneth M. Hildreth, Edward W. Shinabarger, and William J. Gannon. Electrical properties of wall of endolymphatic space of the cochlea (Guinea Pig). *American Journal of Physiology*, 194:396–402, 1958.

[93] Hamid Motallebzadeh, Joris A.M. Soons, and Sunil Puria. Cochlear amplification and tuning depend on the cellular arrangement within the organ of Corti. *Proceedings of the National Academy of Sciences*, 115:5762–5767, 2018.

[94] David C. Mountain, Alan E. Hubbard, Darlene R. Ketten, and Jennifer T. O'Malley. The helicotrema: measurements and models. In Anthony W. Gummer, editor, *Biophysics of the cochlea: from molecules to models*, pages 393–399. World Scientific, 2003.

[95] Bjorn Nadrowski, Pascal Martin, Frank J\"{u}licher, and Frank Ju. Active hair-bundle motility harnesses noise to operate near an optimum of mechanosensitivity. *Proceedings of the National Academy of Sciences of the United States of America*, 101(33), 2004.

[96] Hui Nam and John J. Guinan. Non-tip auditory-nerve responses that are suppressed by low-frequency bias tones originate from reticular lamina motion. *Hearing Research*, 2018.

[97] Jong-Hoon Nam and Robert Fettiplace. Force Transmission in the Organ of Corti Micromachine. *Biophysj*, 98:2813–2821, 2010.

[98] S S. Narayan, Andrei N. Temchin, Alberto Recio, Mario A. Ruggero, and Spoendlin. Frequency tuning of basilar membrane and auditory nerve fibers in the same cochleae. *Science*, 282:1882–4, 1998.

[99] Stephen T Neely. A model of cochlear mechanics with outer hair cell motility. *J Acoust Soc Am*, 1993.

[100] Stephen T. Neely. A model of cochlear mechanics with outer hair cell motility On liquid-film thickness measurements with the atomic-force microscope A model of cochlear mechanics with outer hair cell motility. *The Journal of the Acoustical Society of America*, 94(68):186–1201, 1993.

[101] Andrew N Norris and Douglas A Rebinsky. Acoustic reciprocity for fluid-structure problems. Technical report.

[102] Manuela Nowotny and Anthony W. Gummer. Nanomechanics of the subtectorial space caused by electromechanics of cochlear outer hair cells. *Proceedings of the National Academy of Sciences of the United States of America*, 103(7):2120–2125, 2006.

[103] Alfred L. Nuttall and David F. Dolan. Two-tone suppression of inner hair cell and basilar membrane responses in the guinea pig. *The Journal of the Acoustical Society of America*, 93(1):390–400, 1993.

[104] Alfred L. Nuttall, Jiefu Zheng, Tianying Ren, and Egbert De Boer. Electrically evoked otoacoustic emissions from apical and basal perilymphatic electrode positions in the guinea pig cochlea. *Hearing Research*, 2001.

[105] Anthony W Peng, Thomas Effertz, and Anthony J Ricci. Adaptation of mammalian auditory hair cell mechanotransduction is independent of calcium entry. *Neuron*, 80(4):960–72, 11 2013.

[106] Gianluca Piazza, Valeriy Felmetsger, Paul Muralt, Roy H. Olsson, and Richard Ruby. Piezoelectric aluminum nitride thin fi lms for microelectromechanical systems, 2012.

[107] Bogdan-Ioan Popa and Steven A. Cummer. Non-reciprocal and highly nonlinear active acoustic metamaterials. *Nature communications*, 2014.

[108] David J. Powell, Gordon Hayward, and Robert Y. Ting. Unidimensional modeling of multi-layered piezoelectric transducer structures. *IEEE Transactions on Ultrasonics, Ferroelectrics, and Frequency Control*, 45(3):667–677, 1998.

[109] Richard J. Powers, Sue Kulason, Erdinc Atilgan, William E. Brownell, Sean X. Sun, Peter G. Barr-Gillespie, and Alexander A. Spector. The local forces acting on the mechanotransduction channel in hair cell stereocilia. *Biophysical Journal*, 106(11), 2014.

[110] Richard J. Powers, Sitikantha Roy, Erdinc Atilgan, William E. Brownell, Sean X. Sun, Peter G. Gillespie, and Alexander a. Spector. Stereocilia membrane deformation: Implications for the gating spring and mechanotransduction channel. *Biophysical Journal*, 102(2):201–210, 1 2012.

[111] Srdjan Prodanovic, Sheryl Gracewski, and Jong-Hoon Hoon Nam. Power Dissipation in the Subtectorial Space of the Mammalian Cochlea Is Modulated by Inner Hair Cell Stereocilia. *Biophysical Journal*, 108(3):479–488, 2015.

[112] S Puria and J B Allen. A parametric study of cochlear input impedance. *The Journal of the Acoustical Society of America*, 1991.

[113] Martin N. Raftenberg. Flow of endolymph in the inner spiral sulcus and the subtectorial space. *The Journal of the Acoustical Society of America*, 87(6):2606, 1990.

[114] Sripriya Ramamoorthy, Niranjan V Deo, and Karl Grosh. A mechano-electro-acoustical model for the cochlea: response to acoustic stimuli. *The Journal of the Acoustical Society of America*, 121(5 Pt1):2758–2773, 2007.

[115] Alberto Recio-Spinoso and John S. Oghalai. Mechanical tuning and amplification within the apex of the guinea pig cochlea. *The Journal of Physiology*, 00(650):1–13, 4 2017.

[116] Tobias Reichenbach and A J Hudspeth. A ratchet mechanism for amplification in low-frequency mammalian hearing. *Proceedings of the National Academy of Sciences*, 107, 2010.

[117] Tianying Ren. Longitudinal pattern of basilar membrane vibration in the sensitive cochlea. *Proceedings of the National Academy of Sciences*, 99, 2002.

[118] Tianying Ren, Wenxuan He, and David Kemp. Reticular lamina and basilar membrane vibrations in living mouse cochleae. *Proceedings of the National Academy of Sciences of the United States of America*, 113(35):9910–5, 8 2016.

[119] William S. Rhode. Observations of the Vibration of the Basilar Membrane in Squirrel Monkeys using the Mssbauer Technique. *The Journal of the Acoustical Society of America*, 49:1218–1231, 1971.

[120] A. J. Ricci, A. C. Crawford, and R. Fettiplace. Active Hair Bundle Motion Linked to Fast Transducer Adaptation in Auditory Hair Cells. *J. Neurosci.*, 20(19):7131–7142, 10 2000.

[121] Anthony J Ricci, Helen J Kennedy, Andrew C Crawford, and Robert Fettiplace. The transduction channel filter in auditory hair cells. *The Journal of neuroscience : the official journal of the Society for Neuroscience*, 25(34):7831–9, 2005.

[122] Claus-Peter Richter, Gulam Emadi, Geoffrey Getnick, Alicia Quesnel, and Peter Dallos. Tectorial Membrane Stiffness Gradients. *Biophysical Journal*, 93(6):2265–2276, 2007.

[123] L Robles and M a Ruggero. Mechanics of the mammalian cochlea. *Physiological reviews*, 81(3):1305–1352, 2001.

[124] M a Ruggero, S S Narayan, a N Temchin, and a Recio. Mechanical bases of frequency tuning and neural excitation at the base of the cochlea: comparison of basilar-membrane vibrations and auditory-nerve-fiber responses in chinchilla. *Proceedings of the National Academy of Sciences*, 97(22):11744–11750, 2000.

[125] Mario A. Ruggero, Nola C. Rich, and Richard L. Freyman. Spontaneous and impulsively evoked otoacoustic emission: indicators of cochlear pathology? *Hearing Research*, 10:283–300, 1983.

[126] Mario A Ruggero and Andrei N Temchin. The roles of the external, middle, and inner ears in determining the bandwidth of hearing. *Proceedings of the National Academy of Sciences of the United States of America*, 99(20):13206–10, 10 2002.

[127] Ian J Russell, P Kevin Legan, Victoria A Lukashkina, Andrei N Lukashkin, Richard J Goodyear, and Guy P Richardson. Sharpened cochlear tuning in a mouse with a genetically modified tectorial membrane. *Nature neuroscience*, 2007.

[128] Aritra Sasmal, Nathan Geib, and Karl Grosh. Broadband nonreciprocal linear acoustics through nonlocal active media. *arXiv preprint*, 2019.

[129] Aritra Sasmal and Karl Grosh. The competition between the noise and shear motion sensitivity of cochlear inner hair cell stereocilia. *Biphysical Journal*, 114:474–483, 2018.

[130] Aritra Sasmal and Karl Grosh. Unified cochlear model for low- and high-frequency mammalian hearing. *Proceedings of the National Academy of Sciences*, 116:13983–88, 2019.

[131] Peter M. Sellick and Ian J. Russell. The responses of inner hair cells to basilar membrane velocity during low frequency auditory stimulation in the guinea pig cochlea. *Hearing Research*, 2:439–445, 1980.

[132] Lei Shao and Kevin P. Pipe. Amplification and directional emission of surface acoustic waves by a two-dimensional electron gas. *Applied Physics Letters*, 2015.

[133] Christopher A. Shera. Frequency glides in click responses of the basilar membrane and auditory nerve: Their scaling behavior and origin in traveling-wave dispersion. *The Journal of the Acoustical Society of America*, 2001.

[134] Christopher A. Shera. Laser amplification with a twist: Traveling-wave propagation and gain functions from throughout the cochlea. *The Journal of the Acoustical Society of America*, 122(5):2738, 2007.

[135] Christopher A. Shera and John J. Guinan. Evoked otoacoustic emissions arise by two fundamentally different mechanisms: A taxonomy for mammalian OAEs. *The Journal of the Acoustical Society of America*, 105(2):782–798, 1999.

[136] Christopher A. Shera, John J. Guinan, and Andrew J. Oxenham. Otoacoustic estimation of cochlear tuning: Validation in the chinchilla. *JARO - Journal of the Association for Research in Otolaryngology*, 11(3):343–365, 2010.

[137] W. Richard Smith, Henry M. Gerard, Thomas M. Reeder, Herbert J. Shaw, and Jeffrey H. Collins. Analysis of Interdigital Surface Wave Transducers by use of an Equivalent Circuit Model. *IEEE Transactions on Microwave Theory and Techniques*, 1969.

[138] Joris A. M. Soons, Anthony J. Ricci, Charles R. Steele, and Sunil Puria. Cytoarchitecture of the Mouse Organ of Corti from Base to Apex, Determined Using In Situ Two-Photon Imaging. *Journal of the Association for Research in Otolaryngology*, 16(1):47–66.

[139] Dimitrios L. Sounas and Andrea Alù. Non-reciprocal photonics based on time modulation, 2017.

[140] Bethanie J.H. Stadler and Tetsuya Mizumoto. Integrated magneto-optical materials and isolators: A review, 2014.

[141] Eric A. Stauffer and Jeffrey R. Holt. Sensory transduction and adaptation in inner and outer hair cells of the mouse auditory system. *Journal of Neurophysiology*, 98:3360–3369, 2009.

[142] Charles R. Steele and Sunil Puria. Force on inner hair cell cilia. *International Journal of Solids and Structures*, 42(21-22):5887–5904, 10 2005.

[143] Charles R. Steele and Larry A. Taber. Comparison of WKB calculations and experimental results for three-dimensional cochlear models. *The Journal of the Acoustical Society of America*, 65(4):1007, 1979.

[144] David Strelioff. A computer simulation of the generation and distribution of cochlear potentials. *Journal of the Acoustical Society of America*, 1973.

[145] David Strelioff and ke Flock. Stiffness of sensory-cell hair bundles in the isolated guinea pig cochlea. *Hearing Research*, 15(1):19–28, 1984.

[146] John W. Strutt. On the Constant of Magnetic Rotation of Light in Bisulphide of Carbon. *The Royal Society Philosophical Transactions*, 176:360–384, 1 1885.

[147] Bora Sul and Kuni H. Iwasa. Effectiveness of hair bundle motility as the cochlear amplifier. *Biophysical Journal*, 97(10):2653–2663, 11 2009.

[148] Andrei N. Temchin, Nola C. Rich, and Mario A. Ruggero. Threshold tuning curves of chinchilla auditory-nerve fibers. I. Dependence on characteristic frequency and relation to the magnitudes of cochlear vibrations. *Journal of neurophysiology*, 100(5):2889–98, 11 2008.

[149] Ingo Ulrik Teudt and Claus Peter Richter. The hemicochlea preparation of the guinea pig and other mammalian cochleae. *Journal of Neuroscience Methods*, 162(1-2):187–197, 2007.

[150] Jean-Yves Tinevez, Frank Jülicher, Pascal Martin, Jean-Yves Tinevez, and Frank Ju. Unifying the various incarnations of active hair-bundle motility by the vertebrate hair cell. *Biophysical journal*, 93(11):4053–67, 12 2007.

[151] T. Valis, A. H. von Flotow, and N. W. Hagood. An Acoustic-electromagnetic Piezoelectric Waveguide Coupler. *Journal of Sound and Vibration*, 178(5):669–680, 1994.

[152] Sietse M van Netten, Theo Dinklo, Walter Marcotti, and Corne J Kros. Channel gating forces govern accuracy of mechano-electrical transduction in hair cells. *Proceedings of the National Academy of Sciences of the United States of America*, 100(26):15510–15515, 2003.

[153] Todd W. Vanderah and Douglas J. Gould. *Nolte's Human Brain*. Elsevier, 7 edition, 2015.

[154] Georg von Békésy. *Experiments in Hearing*. McGraw-Hill, 1960.

[155] Yanli Wang, Charles R. Steele, and Sunil Puria. Cochlear Outer-Hair Cell Power Generation and Viscous Fluid Loss. *Nature Scientific Reports*, 6:19475, 2016.

[156] Yifan Wang, Behrooz Yousefzadeh, Hui Chen, Hussein Nassar, Guoliang Huang, and Chiara Daraio. Observation of Nonreciprocal Wave Propagation in a Dynamic Phononic Lattice. *Physical Review Letters*, 121(19), 2018.

[157] Rebecca L Warren, Sripriya Ramamoorthy, Nikola Ciganović, Yuan Zhang, Teresa M Wilson, Tracy Petrie, Ruikang K Wang, Steven L Jacques, Tobias Reichenbach, Alfred L Nuttall, and Anders Fridberger. Minimal basilar membrane motion in low-frequency hearing. *Proceedings of the National Academy of Sciences of the United States of America*, 113(30):4304–10, 7 2016.

[158] Yong Jin Yoon, Charles R. Steele, and Sunil Puria. Feed-forward and feedbackward amplification model from cochlear cytoarchitecture: An interspecies comparison. *Biophysical Journal*, 100(1):1–10, 1 2011.

[159] Valeria Zampini, Lukas Rüttiger, Stuart L. Johnson, Christoph Franz, David N. Furness, Jrg Waldhaus, Hao Xiong, Carole M. Hackney, Matthew C. Holley, Nina Offenhauser, Pier Paolo Di Fiore, Marlies Knipper, Sergio Masetto, and Walter Marcotti. Eps8 Regulates Hair Bundle Length and Functional Maturation of Mammalian Auditory Hair Cells. *PLoS Biology*, 9(4):e1001048, 4 2011.

[160] Deborah E Zetes, Jason A Tolomeo, and Matthew C Holley. Structure and Mechanics of Supporting Cells in the Guinea Pig Organ of Corti. *PLoS ONE*, 7(11), 2012.

[161] Yuxin Zhai, Hyung Suk Kwon, and Bogdan-Ioan Popa. Active Willis metamaterials for ultracompact nonreciprocal linear acoustic devices. *Physical Review B*, 99(22), 2019.

[162] Jing Zheng, Weixing Shen, David Z.Z. He, Kevin B. Long, Laird D. Madison, and Peter Dallos. Prestin is the motor protein of cochlear outer hair cells. *Nature*, 405:149–155, 2000.

[163] Xuefeng Zhu, Hamidreza Ramezani, Chengzhi Shi, Jie Zhu, and Xiang Zhang. PT -symmetric acoustics. *Physical Review X*, 4(3), 2014.

[164] Jozef J. Zwislocki and Lisa K. Cefaratti. Tectorial membrane II: Stiffness measurements in vivo. *Hearing Research*, 42:211–227, 1989.